Investigation of temporal variability in Black hole and Neutron star binary systems across different timescales

M.Sc. Thesis

Vijay Choudhary

Department of Astronomy, Astrophysics and Space Engineering
INDIAN INSTITUTE OF TECHNOLOGY INDORE
May 20, 2025

Investigation of temporal variability in Black hole and Neutron star binary systems across different timescales

M.Sc.Thesis

Submitted in partial fulfillment of the requirements for the awards of the degree
of
Master of Science

by

Vijay Choudhary

Department of Astronomy, Astrophysics and Space Engineering

INDIAN INSTITUTE OF TECHNOLOGY INDORE

May 20, 2025

INDIAN INSTITUTE OF TECHNOLOGY INDORE

CANDIDATE'S DECLARATION

I hereby certify that the work which is being presented in the thesis entitled **Investigation of temporal variability in Black hole and Neutron star binary systems across different timescales** in the partial fulfillment of the requirements for the award of the degree of **MASTER OF SCIENCE** and submitted in the **DEPARTMENT OF ASTRONOMY, ASTROPHYSICS AND SPACE ENGINEERING, Indian Institute of Technology Indore**, is an authentic record of my own work carried out during the time period from June, 2024 to May, 2025 under the supervision of Dr. Manoneeta Chakraborty, Associate Professor, Department of Astronomy, Astrophysics and Space Engineering.

The matter presented in this thesis has not been submitted by me for the award of any other degree of this or any other institute.

12/05/2025

Signature of the student with date

Vijay Choudhary

This is to certify that the above statement made by the candidate is correct to the best of my/our knowledge.

Manoneeta Chakraborty

12/5/2025

Signature of the Supervisor of
M.Sc. thesis (with date)

Dr. Manoneeta Chakraborty

Vijay Choudhary has successfully given his M.Sc. Oral Examination held on **06/05/2025**.

Manoneeta Chakraborty

Signature(s) of Supervisor(s) of MSc thesis
Date: 13/05/2025

Manoneeta Chakraborty

Programme Coordinator, M.Sc.
Date: 19/05/2025

Manoneeta Chakraborty

Convenor, DPGC
Date: 19/05/2025

HoD, DAASE
Date:

Acknowledgments

I would like to express my sincere gratitude to my supervisor, Dr. Manoneeta Chakraborty, for her continuous support, guidance, and encouragement throughout this project. Her insights and feedback have been invaluable in shaping this work.

I would like to express my sincere thanks to Dr. M. C. Ramadevi for kindly providing us with the SSM/Astrosat data, which was crucial for studying the pulsation behavior in our work. Her support and collaboration greatly enriched the quality of this research, and I truly appreciate the time and effort she dedicated to helping us.

I would like to thank Aromal P for providing data for eclipse studies. I also extend my heartfelt thanks to my friends and labmates for their constant support, stimulating discussions, and for making the lab environment enjoyable.

I'm really thankful to everyone who supported me and made this journey easier and more enjoyable.

Abstract

X-ray binary (XRB) systems, comprising a stellar remnant (neutron star or black hole) and a companion star, are key objects for studying accretion physics and the extreme conditions, such as intense gravity and magnetic fields, around compact objects. These X-ray binary systems sometimes show high periodic variabilities on the scales ranging from a few seconds to some days. The periodicity at the scales of milliseconds to seconds can be the pulsation of the neutron star, at the scales of a few hours or days can be the orbital period, and the scales longer than the orbital period are super-orbital periodicities, which arise due to different mechanisms going on there in the accretion disk. This project deals with the analysis of XRBs, focusing on detecting periodicities and understanding the physical processes giving rise to them. Using techniques such as the Lomb-Scargle periodogram for unevenly sampled data, rescaling of the power spectrum to get the noise continuum to remove the red noise component present in the power spectrum, and false alarm probability (FAP) calculations are used to get the significant periodicities in these systems. The science cases of pulsations and super-orbital periods explored to probe neutron star spin and the accretion disk behavior, respectively. This project focuses on the importance of noise reduction techniques in extracting meaningful periodic signals and further enhancing our understanding of compact objects and accretion disk behavior in XRBs. In addition, it focuses on the study of long-term evolution of detected periodicities to get the ideas about the evolving mechanisms producing them and the energy dependence of the superorbital periodicities to get an idea about the emitting region from the system. Other than superorbital periods, we also conducted an analysis to investigate the temporal evolution of pulsation in selected XRBs. Also, an effort is made to model eclipses in these systems which can give a deeper insights of XRBs.

Contents

List of Figures

List of Tables

Chapter 1

Introduction

Neutron stars and black holes are some of the most strange, weirdest, but most interesting objects in the universe. These are the remnants that result from the explosion of massive stars. When massive stars die, they collapse under their own gravity, triggering a powerful explosion called a supernova. The death of a star or a supernova produces an immense amount of energy that sometimes can outshine an entire galaxy. During the explosion, the core of the star is compressed into a very compact and dense object. Depending upon the mass of the progenitor star, the remnant can either be a neutron star - an object so dense that a spoon of its material weigh approx a trillion of kilograms, or a black hole - an object so gravitationally strong that even the fastest of all the entities, the light, cannot escape once comes to its vicinity.

The study of these compact objects offers valuable insights into stellar evolution, extreme rotational dynamics, intense magnetic fields, and the effects of strong gravity on spacetime geometry. Tracing their transformation from normal stars to compact remnants enhances our understanding of the various evolutionary stages and the physical conditions that govern them. The remarkable and often unexpected behavior of these objects continues to challenge and captivate the scientific community. These show humans the limit of their bright, beautiful, and intelligent minds.

The sections below give a brief introduction to these objects separately, followed by the instruments used, analysis and results, discussion and the future aspects of the project.

1.1 Neutron stars

Neutron stars are formed when a progenitor star with a mass between $8 - 20M_{\odot}$ ($M_{\odot}$ = solar mass) goes through a supernova explosion. The remnant core, compressed into an extremely dense object (about 10-15 km in diameter), becomes a neutron star. The core's density is so high that neutrons are formed by the merging of protons and electrons. These stars are highly compact, such that their density reaches $10^{17}\ kg/m^3$. These objects have very strong magnetic fields (of the order of 10^{8-15} Gauss) (Reisenegger 2001) and rotation periods of a few milliseconds to seconds. These properties are crucial for understanding the underlying physics of neutron stars. Figure 1.1 shows a picture of a neutron star in which the blue object represents the neutron star and the curved lines connecting the poles represent the magnetic field lines.

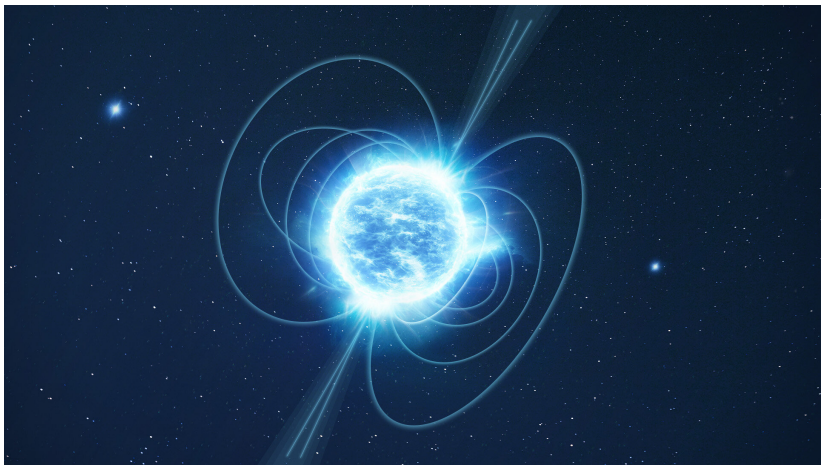

Figure 1.1: Artistic impression of Neutron Star. Credit: ESA.

1.2 Black holes

Black holes are the result of the supernova explosion of a star whose mass is greater than $20M_{\odot}$. If the mass of the core remnant exceeds more than 2-3 $M_{\odot}$ (the Tolman–Oppenheimer–Volkoff limit), the outward pressure, neutron degeneracy pressure, can no longer support it. The core collapses entirely, forming a black hole where gravity is so powerful that nothing, even light, cannot escape through it. The compactness creates an intense

gravitational field, warping spacetime so severely that it leads to phenomena like time dilation and frame-dragging (especially in rotating black holes). This warping has an extreme effect on the path of matter around it, the orbit of the nearby stars, and even on the path of light. Figure 1.2 shows a simple representation of a black hole. The black circle in the center and the orange colour around the center represent the black hole and matter around it, respectively.

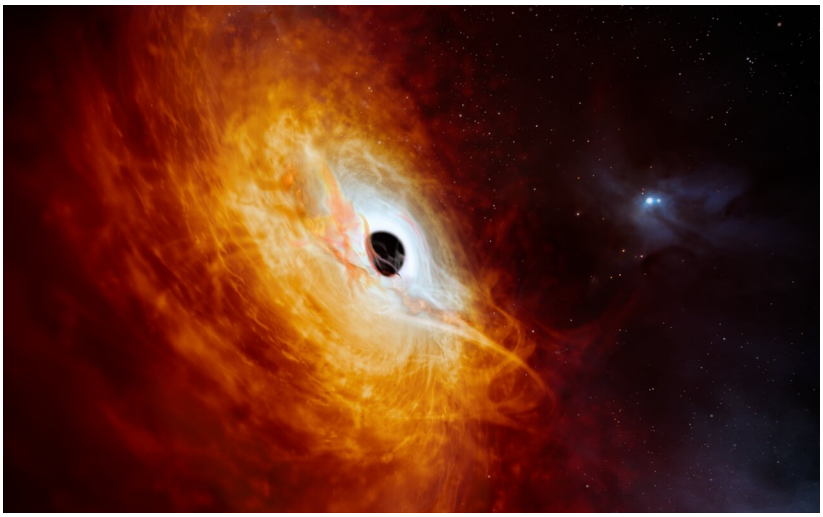

Figure 1.2: Artistic impression of Black Hole. Credit: ESO/M. Kornmesse.

1.3 X-ray Binaries (XRBs)

When these compact objects are in orbit with any other star, most of the time a main sequence star, they form a binary star system. As the companion revolves around the compact object, its matter or the photospheric gas starts to accrete around the compact object forming a disk-like structure, called the accretion disk. The matter, accreting or in-falling, has some gravitational potential energy associated with it, which gets converted into kinetic energy and eventually into heat, due to which the temperature of the disk reaches some millions of kelvin (10^7 K), emitting radiation in X-rays. Hence, these objects are called **X-ray binaries (XRBs)**. Figure 1.3 shows the schematic diagram of such an XRB. The different components of these systems are labeled in the diagram.

The XRBs can be mainly classified into two categories depending upon

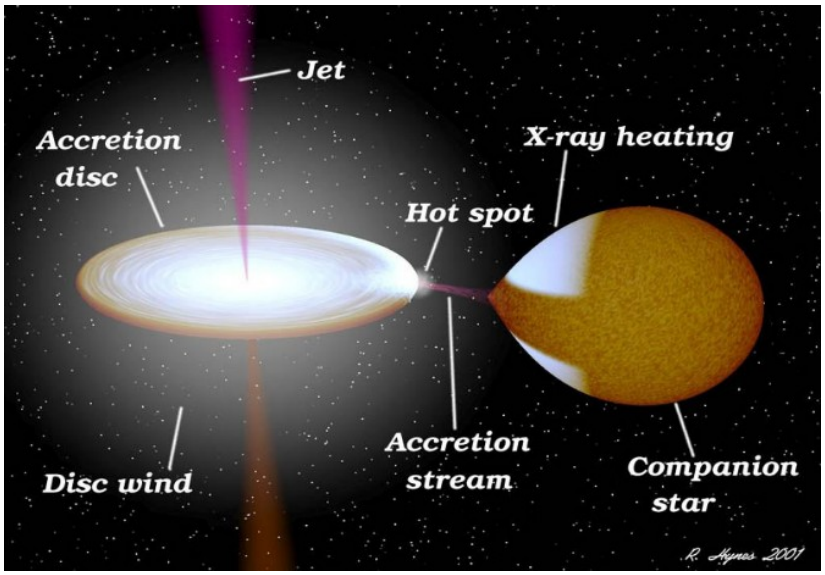

Figure 1.3: Representation of an X-ray binary. (Credit: NASA/R. Hynes.)

the nature of the companion star the systems have: **Low Mass X-ray Binaries (LMXBs)** and **High Mass X-ray Binaries (HMXBs)**.

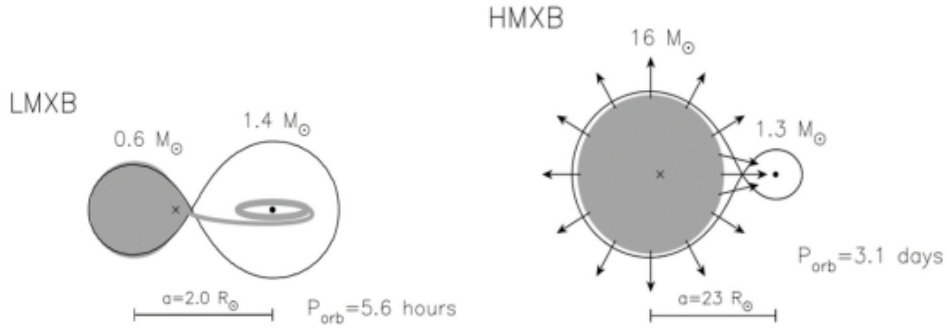

(a) LMXB (b) HMXB

Figure 1.4: The figure shows an LMXB (a) and HMXB (b) with a neutron star as the compact object. Roche lobe overflow in LMXB and stellar wind accretion in HMXB are also shown. (From: Tauris and E. v. d. Heuvel 2003).

1.3.1 Low Mass X-ray Binaries

These are the X-ray binary systems in which the companion star has a mass around $1M_{\odot}$, and the accretion is dominated by Roche lobe overflow. The Roche lobes are the region for stars in a binary system, which are formed due to equipotential surfaces (formed due to the potential energies

of both the component stars, the remnant and the companion), and the matter of the individual star is gravitationally bound to itself in this region. Figure 1.5 depicts the equipotential surfaces and the Roche lobes in a binary star system. The curves around the stars are the equipotential surfaces and the equipotential surface with '∞-like' structure forms the Roche lobes of the two stars. The point joining the two Roche lobes is called Lagrangian point 1 (L1). If the matter crosses this point from the companion, it will no longer be bound to the star and start accreting around the compact object, forming the accretion disk. The companion star in this case is a low-mass star with a longer lifespan, which allows Low-Mass X-ray Binary (LMXB) systems to persist for a long duration-typically between $10^7 - 10^9$ yrs (Tauris and E. v. d. Heuvel 2003). An example of LMXB is shown in Figure 1.4a.

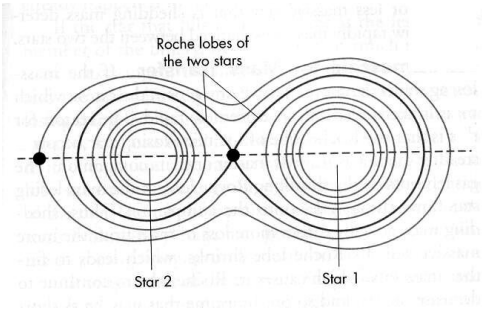

Figure 1.5: Equipotential surfaces and Roche lobe.

1.3.2 High Mass X-ray Binaries

These are the systems with a companion which has a mass greater than $10M_{\odot}$ (an O, B type of star) and the accretion is dominated by stellar winds. These types of companion stars have high temperatures, which results in the burning of the star's nuclear fuel rapidly, and hence, the star has a shorter life compared to low-mass stars. Therefore, these systems last for a shorter period ($10^5 yrs$) (Tauris and E. v. d. Heuvel 2003) relative to LMXBs. A typical diagram of HMXB is shown in Figure 1.4b.

1.3.3 Accreting X-ray Pulsars

An important subclass of XRBs is **Accreting X-ray Pulsars (AXPs)**, where a very fast rotating neutron star is the accreting object. Pulsars are neutron stars that produce pulses. In these systems, the matter is channeled

to the magnetic poles by the magnetic field of the pulsar, which results in the creation of hotspots. When the rotational and magnetic axes are not aligned, the moving in and out of these hotspots with respect to the line of sight of an observer shows pulsation. As time passes, these neutron stars start rotating faster and faster due to the transfer of angular momentum from the accretion disk to the neutron star, and the process is called **recycling scenario**. This results in a change of pulsation period to milliseconds. Figure 1.6 shows a schematic diagram of an AXP.

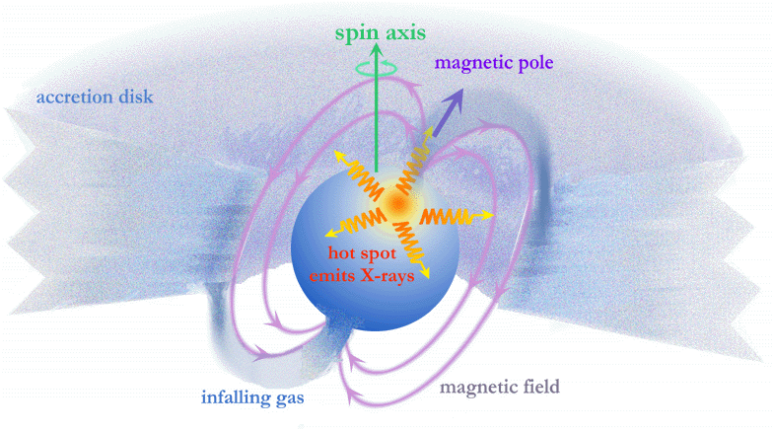

Figure 1.6: Diagram showing matter falling from the accretion disk onto the neutron star. (Illustration: CXC/S. Lee).

1.4 Motivation

XRB emission typically is highly variable, and these sources show variabilities across time scales ranging from seconds to days. Apart from the millisecond to second scale variabilities shown by XRBs, which are often related to instabilities/fluctuations in the disk or the corona, various long-term periodicity and timing behaviors are observed, which can shed light on the complementary physical processes in these systems. Changes in these periodicities will indicate shifts in the system and the underlying physical processes responsible for these changes.

The sections below discuss the different aspects of the variabilities across different timescales considered for this study in detail.

1.4.1 Superorbital periods

The periodic variability in X-ray emission on time scales larger than the orbital period (P_{orb}) falls in the category of superorbital periods (P_{sup}). Such superorbital periodicities typically range from a few days to hundreds of days. The study of superorbital periods gives us a deep understanding of the accretion processes and large-scale instabilities in the accretion disk. The cause of superorbital periods can be attributed to the precession of the accretion disk, radiation-induced wrapping, X-ray state change, magnetic wrapping, wind-driven tilting, processing relativistic jets, or a third body in the system, as discussed by Kotze and P. A. Charles 2011 (hereafter KC11). Knowing the superorbital period can help in the prediction of these physical scenarios. Also, the change in superorbital periods with time shows the modulation in the physical process giving rise to them, for e.g., a slowly evolving warp in the disk.

Earlier, many studies have been made to find the periodicities in different X-ray binary systems. Some of these studies focus on individual sources, whereas some focus on a group of sources. Priedhorsky and Terrell 1983 studied sources, GX 301-2, 4U 1145-619 and GX 304-1, and found periods of 41.5, 187 and 132.5 days, respectively. Another study made by them in 1984 revealed a period of 199 days in X1916-053, 41.6 days in X1907+09 and a period of 122-125 days in Aql X-1 (Priedhorsky and Terrell 1984).

Both studies were done using Vela 5B. Investigations made by Smale and Lochner 1992 confirmed the 175 days period reported by Priedhorsky and Terrell (1983a) in X1820-303 but not the 199 day period in X1916-053. They reported period of ~77 days in Cyg X-2 and ~333 days in Cyg X-3. Priedhorsky et al. (1995) made a search for period in 8 XRBs detected by WATCH Eureca, but did not find any new period. Studies made by Wen et al. 2006 examined the long-term light curve of a sample of sources and found orbital periods and superorbital periodicities in different X-ray sources utilizing 8.5 years of Rossi X-Ray Timing Explorer All-Sky Monitor (RXTE ASM) data. Their study demonstrates that the orbital modulation is more readily detected in HMXBs than in LMXBs. They studied the complete light curves to find the periodicities (not the periodicity modulation).

Other studies are done to find periods in single sources. The study conducted by Jun-yi et al. 2017 focused on the X-ray source SS433 and found period of ~6.29, 6.54, 13.08, 81.50 and 162.30 days in different energy bands using Swift/Burst Alert Telescope (Swift/BAT) and Rossi X-ray Timing Explorer/All Sky Monitor (RXTE/ASM). Ackermann et al. 2015 found multi-wavelength and γ-ray quasi-periodicity in gamma-ray blazar PG 1553+113 and reported a very long period of about 2 years. Corbet et al. 2024 confirmed the previously detected period of ~244 days reported by RXTE Proportional Counter Array (PCA) monitoring observations for XTE 1829-098.

A comprehensive work has been conducted by Kotze and P. A. Charles 2011 to look for the varying periodicities of XRB sources and their causes. They aimed to characterize these periodicities in a completely systematic way. They found some sources that were stable throughout their observations (like LMC X-4 and Her X-1) and some that showed chaotic behavior (like Sco X-1 and LMC X-2). Also, they claimed that some of the superorbital periodicities that were detected could be a result of modulation in mass accretion rate ($\dot{M}$) rather than warped or precessing accretion disks. However, often, the cause of these periodicities and the exact triggering mechanism behind their physical origin remain ambiguous. Furthermore, governing factors resulting in some periodicities being stable and the other evolving chaotically, need to be unveiled. Certain scenarios invoked to ex-

plain these superorbital periodicities can also have a crucial role to play in the outburst behavior of the XRBs. Additionally, the evolution of the detected superorbital periodicities over the years will reveal the transient nature of these XRB systems.

Following the work by Kotze and P. A. Charles 2011, in this study, we will examine the intervals that have not been previously analyzed (may have some days of overlapping between the intervals), which will help us understand the detailed evolution of these systems. We will investigate the reasons behind the emerging periodicities and their evolution. We will also try to look for changes in periodicities due to modulation in $\dot{M}$.

In addition, our research will also explore the energy dependencies associated with these periodicities, which may enhance our understanding of the X-ray-emitting region. Since there may be differences in the modulation of a particular periodicity in different energy bands, it gives more insight into the emitting region that produces the periodicity.

1.4.2 Pulsation

Pulsation is produced when the magnetic field channels the matter to the magnetic poles from the accretion disk in a neutron star binary system, which creates hotspots. When these hotspots move in and out of the line of sight of an observer, they produce pulses, similar to that is observed at a lighthouse. Pulsation helps in probing the spin or the rotation of the pulsar, the strength, geometry and behavior of the magnetic field, and the accretion processes. It reveals information about the accretion rate, as the change in pulsation characteristics follows the change in the rate of accretion. On a global scale, the spinning-up and spinning-down of the neutron star is a result of mass and angular momentum transfer from the accretion disk (Salvo and nana 2020; Walter and Ferrigno 2017).

Earlier studies showed that some sources like XTE J1751-305, XTE J1807-294, IGR J17511-3057 and IGR J00291+5934 spin-up during outbursts, whereas some sources like IGR J17591-2342, XTE J0929-314, IGR J17498-2921 and XTE J1814-338 show spin-down during the accretion phase (Salvo and nana 2020). The spin frequencies evolve very slowly. Frequency derivative ($\dot{\nu}$) of $\sim 5 - 8 \times 10^{-13}$ Hz/sec has been observed in

IGR J00291+5934 by Falanga, M. et al. 2005. A $\sim 9 \times 10^{-12}$ Hz/sec of frequency spin-up rate was detected by A. Sanna et al. 2017 for source GRO J1744-28 with frequency 2.14 Hz. The spin-down rate was observed in IGR J17591-2342 with -7×10^{-14} Hz/sec by Sanna et al. 2020 and they constrained the magnetic field to be $\sim 2.8 \times 10^{8}$ gauss. Similarly, the spinning down rate of -6.3×10^{-14} Hz/sec in IGR J17498-2921 (Papitto, Bozzo, et al. 2011) and -6.7×10^{-14} Hz/s in XTE J1814-338 (Papitto, Di Salvo, et al. 2007) has been seen. Sometimes, rather than the exact value of spin derivatives, a range of values has been observed, like in source IGR J17379-3737, $-0.5 \times 10^{-14} < \dot{\nu} < 0.9 \times 10^{-14}$ Hz/sec (Sanna, A. et al. 2018). Determining the frequency derivative is essential for calculating the magnetic field (B) of a neutron star, as it is directly related to the spin derivative or, equivalently, the period derivative as $B \propto (P\dot{P})^{1/2}$ (Salvo and nana 2020).

For the above discussed features, we will search for long-term changes in the pulsation period and strength that may help us understand the change in accretion rates. We will examine the monotonicity of the period change, i.e., whether the period is only spin-up or down, or if there is any torque reversal, and try to find their cause. Hence, pulsation is a powerful property that can be used to study the evolution of the neutron star and the binary system, especially with respect to its magnetic field and rotational properties. We can also try to find some correlation between the superorbital and pulsation period and their variation.

1.4.3 Eclipse modeling

In X-ray binary systems, an eclipse occurs when the companion star obscures the X-ray source, leading to a reduction in the observed X-ray flux. Modeling eclipse helps in understanding some of the crucial parameters of the system, like mass ratio, binary separation, binary inclination, and orbital period, as discussed by Buisson et al. 2021. Variations and jitters in the eclipse occurrence times also shed light on the changes (possible shrinking) in the binary orbit over extended timescales. The eclipse characteristics, profiles, and radiative behavior can also shed light on the stellar atmosphere and associated intricacies (stellar prominences, etc.).

By modeling the eclipse, we will try to find the above-mentioned param-

eters and also check for the orbital period change from the long observations. We will look for the trend in the ingress and egress time with different orbits, which will show the changing behavior of the companion.

The above-discussed properties give us a much deeper and better understanding of the physical processes and evolution of these X-ray binary systems. Hence, this study focuses on these phenomena using long-term high-sensitivity data of XRBs to obtain a clearer understanding of the physical processes affecting these systems, especially with regard to accretion properties and binary geometry. We aim to investigate these long-term variabilities in X-ray Binaries (XRBs) across time scales ranging from seconds to days.

The instruments considered for this purpose are discussed in the following section, and the results obtained are presented in the Analysis and Results section.

Chapter 2

Instrument

The choice of instrument is made based on the requirements and motivation of the scientific objectives. For this project, the instrument should be operational in energy bands corresponding to X-rays (i.e. in keV). As we are looking for long-term periodicity and changes in the XRB systems, the instrument should have regular, long observations of the astronomical sources in the study. For this requirement, the best option is to use scanning monitors (which scan a large patch of sky regularly) instead of focusing monitors (which only focus on a particular source for short durations). Hence, such scanning monitors give us regular, continuous, long-term observations of sources relative to the focusing monitors. Other than regular and continuous observations, the time resolution of the instrument should be such that small periodicities can also be detected. For example, suppose we want to detect pulsation of, let us say, 401 Hz (for the X-ray source SAX J1808.4-3658) or the spin period 0.002494 seconds (1/401 sec). In this case, the instrument should at least have a resolution of milliseconds, otherwise, the spin period will not be detected. Also, different instruments covering different energy bands in X-rays can be used to study the energy dependence of the detected periodicities in binary systems.

Keeping in mind the above requirements, we decided to use the data from the following instruments/satellites:

2.1 Scanning Sky Monitor (SSM) onboard AstroSat

To find the periodicities in these systems, we initially aimed to use the Scanning Sky Monitor (SSM) onboard the AstroSat mission. AstroSat contains three SSM detectors, namely SSM1, SSM2 and SSM3, all of which are one-dimensional position-sensitive gas-filled proportional counters with coded masks. Figure 2.1 presents a detailed picture of SSM. The coded masks are used to detect the position of the source in the sky (Figure 2.2). The field of view of the central SSM is 22.1° × 100° and 26.8° × 100° for the other two. With their separate electronics, the detectors are mounted on a rotating platform. Its time resolution is 1 ms and operational in 2-10 keV energy band. The gas used in these detectors is 25% Xe + 75% P-10 (P-10 is 90% Argon + 10% Methane) (Seetha et al. 2006; *AstroSat, INDIA'S FIRST MULTIWAVELENGTH ASTRONOMY SATELLITE.* 2014).

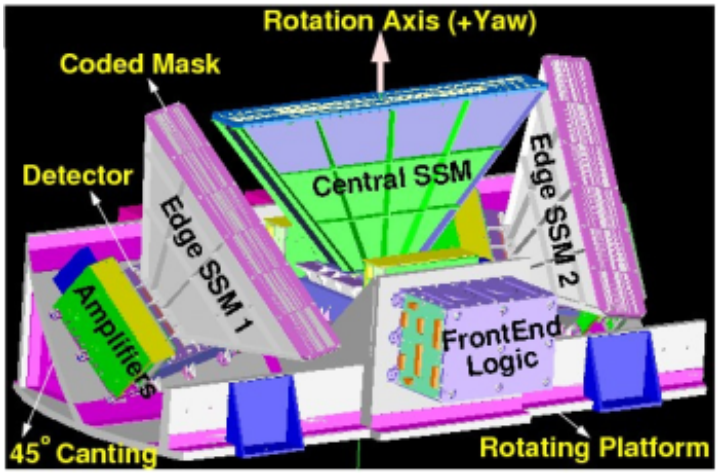

Figure 2.1: Image of Scanning Sky Monitor. From: *AstroSat, INDIA'S FIRST MULTIWAVELENGTH ASTRONOMY SATELLITE.* 2014.

2.2 Monitor of All-sky X-ray Image

Another instrument that we are using is the Monitor of All-Sky X-ray Image (MAXI) onboard the International Space Station (ISS) (Figure 2.3), which has been used to search for long-term periodicities. The instrument has two detectors:

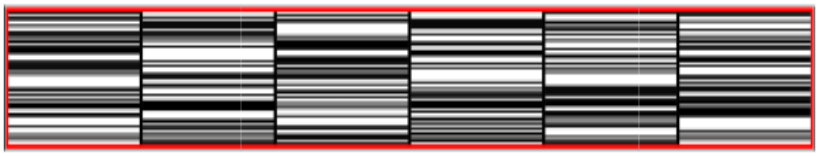

Figure 2.2: The coded mask plate with six different mask patterns for each SSM cameras. From: *AstroSat, INDIA'S FIRST MULTIWAVELENGTH ASTRONOMY SATELLITE.* 2014.

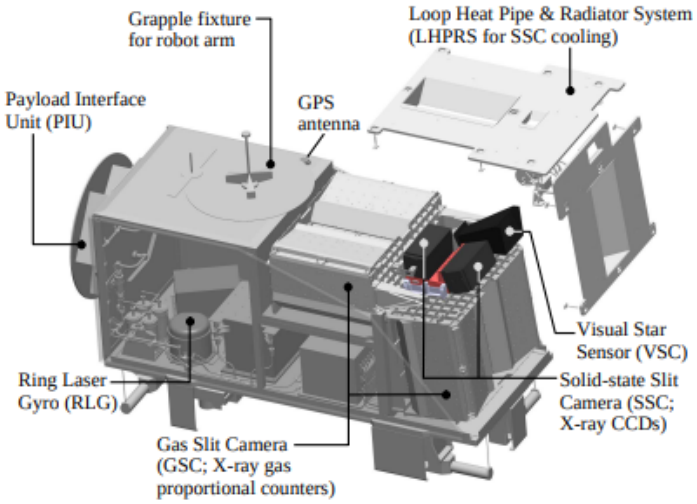

Figure 2.3: Overview of MAXI. From: Matsuoka et al. 2009.

Gas Slit Camera (GSC), which is a one-dimensional position-sensitive gas proportional counter operational in energy band 2-30 keV. It provides a field of view of $160^o \times 1.5^o$, and scans 90 to 98 % of all-sky every 96 min (one orbit/rotation period of the ISS), and has an absolute time resolution of 0.1 ms (n.d.; Matsuoka et al. 2009).

Solid-state Slit Camera (SSC), which is a charged-coupled device (CCD) and operational in energy band 0.5-12 keV. It provides the field of view of $90^o \times 1.5^o$ and scans 70 % of all-sky every 96 min (one orbit/rotation period of the ISS) and has an absolute time resolution of 5.8 s (n.d.; Matsuoka et al. 2009). The 1-day averaged data from GSC in band 2-20 keV is used for the study.

2.3 Large Area X-ray Proportional Counter (LAXPC) on-board AstroSat

LAXPC is one of the major components of AstroSat. The satellite has 3 identical LAXPC instrument with X-ray detection volume of $100cm \times 36cm \times 15cm$. Each unit has a field of view of $1^o \times 1^o$. The proportional counter is filled with a mixture of xenon (90%) and methane (10%), and is operational in a wide energy band of 3-80 keV (Yadav et al. 2016). Figure 2.4 shows the image of the three units of LAXPC. We have used the data from the LAXPC

Figure 2.4: The three units of LAXPC. Image credit: TIFR.

to study the eclipse behavior of source EXO 0748-676. This source is used because SSM data is low quality with large gaps, and MAXI's 1-day bins are too coarse to detect short eclipses lasting minutes to hours.

Chapter 3

Analysis and Results

3.1 Analysis

In this study, we considered all the sources mentioned in the paper M. M. Kotze and P. A. Charles, 2011 (hereafter KC11) for examining their long-term variability, as these sources exhibit reported superorbital periodicities, making them promising candidates for this study. The ASM 1-d average data sets used in the referred paper span from 1996 February 20 to 2011 February 12. Here, we have considered MAXI/GSC light curve data with 1-day binning spanning more than 15 years, i.e., from MJD 55050 to MJD 60580 from (http://maxi.riken.jp/top/slist.html). The light curves are provided in four different energy bands, i.e., 2-4 keV, 4-10 keV, 10-20 keV and 2-20 keV. The intensities are given in the units of photon/s/cm^2 and time in MJD. Fig. 3.1 and Fig. 3.2 show the examples of light curves obtained from the MAXI observations. Apart from the long-term light curves, the occurrences of various types of outbursts can be observed from Fig. 3.1 for GX 339-4, which is a frequently outbursting transient XRB. Fig. 3.2 shows a less variable long-term behavior in the light curve. Since the binning of the light curve is 1-day, we will not be able to find the periodicities smaller than 2 days because of the Nyquist limit. The Nyquist theorem states that the maximum frequency that can be detected is half of the sampling rate or the minimum period that can be detected is twice the sampling time (or binning). To find the periodicities of seconds and hours, the binning of the light curves should be smaller than the desired periodicity of seconds

or hours, respectively. Though the paper KC11 mentioned 25 sources, but MAXI data was not available for three sources among them, namely, IGR J17098–3628, MS 1603.6+2600 and X1820–303. Therefore, we conducted our long-term periodicity search analysis using MAXI data for the other 22 sources.

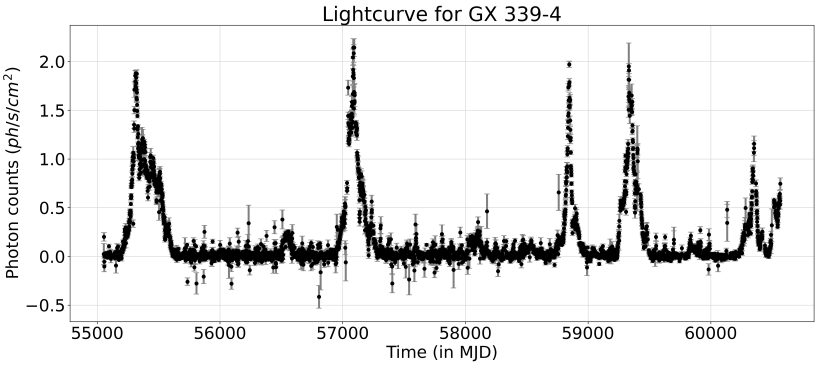

Figure 3.1: Lightcurve of GX 339-4 with 1-day binning. The source shows strong variability. The black points are the measured count rates and small gray lines with the data points are the uncertainties in the photon count rate.

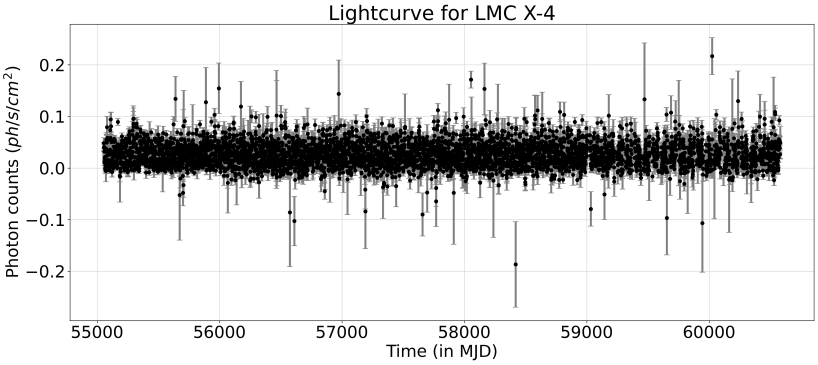

Figure 3.2: Lightcurve of LMC X-4 with 1-day binning. The source does not show high variabilities as GX 339-4. The black points are the measured count rates and small gray lines with the data points are the uncertainties in the photon count rate.

After obtaining the long-term light curves, we proceeded to search for long-term periodicities in the light curves for each source. The 15-year-long light curves produced are occasionally not evenly sampled. To find periodicities in such cases of unevenly spaced data, the traditional Fourier

transform cannot be used, as it works for evenly sampled data points. To deal with this problem, we have used the Lomb-Scargle method to produce the periodograms, which is discussed as follows:

3.1.1 Lomb-Scargle Periodogram

The method used to make the periodogram from the light curve is Lomb-Scargle (Lomb 1976; Scargle 1982). It is preferred over the traditional Fourier transformation because it can be used for unevenly distributed data points in the light curve, whereas, in the traditional Fourier method, the data points in the light curve should be evenly sampled. The Lomb-Scargle method essentially fits a sinusoidal model to the data at various trial frequencies and evaluates the goodness-of-fit using a least-squares approach. In other words, the method scans a range of trial frequencies, up to the Nyquist frequency, and then at each frequency, the power is computed based on how well the sinusoidal model matches the data.

In the Lomb-Scargle periodogram, the power at any frequency range is given by Eq. 3.1 (VanderPlas 2018):

$$P_{LS}(f) = \frac{1}{2}\left[\frac{\left(\sum_{n=1}^{N} x_n \cos(2\pi f[t_n - \tau]\right)^2}{\sum_{n=1}^{N} \cos^2(2\pi f[t_n - \tau])} + \frac{\left(\sum_{n=1}^{N} x_n \sin(2\pi f[t_n - \tau]\right)^2}{\sum_{n=1}^{N} \sin^2(2\pi f[t_n - \tau])}\right] \tag{3.1}$$

where, t_n is the time at n = 1, 2, 3....., N (N = data points in the lightcurve), which are not necessarily evenly sampled, f is the frequency at which power is being calculated and τ is specified for each f to ensure time-shift invariance and is defined as:

$$\tau = \frac{1}{4\pi f} \tan^{-1}\left(\frac{\sum_{n=1}^{N} \sin(4\pi f t_n)}{\sum_{n=1}^{N} \cos(4\pi f t_n)}\right) \tag{3.2}$$

Eq. 3.1 reduces to the classical Fourier form in the case of even sampling and is time shift-invariant and proven better than standard Fourier expressions in the cases of non-uniformly distributed data sets. The Lomb-Scargle periodogram constructed from MAXI light curve data with 1-day sampling for the XRB source X1636-536 is shown in Fig. 3.3. One can note the

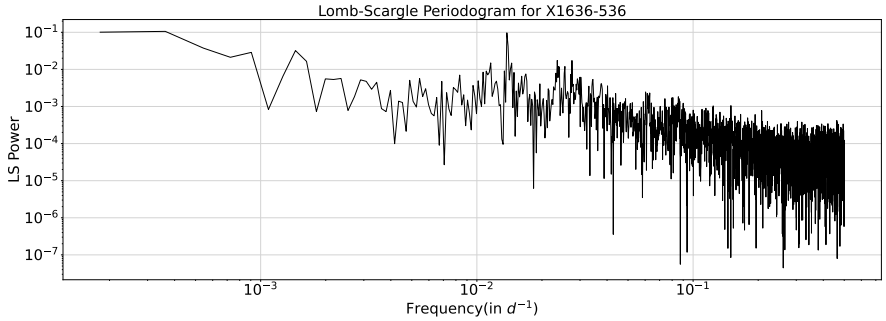

Figure 3.3: Lomb-Scargle periodogram for X1636-536.

presence of red noise (high power at lower frequencies) in the periodogram. The red noise leads to the detection of false periods, suppressing the real periods present in the source. Hence, before proceeding, the noise has to be removed.

However, plotting the periodogram with any of the methods does not resolve the problem of noise in the periodogram. To detect the significant periodicities, noise reduction is one of the major jobs. To do this, we used two methods, light curve chunking and rescaling of the periodogram, which are discussed below.

3.1.2 Light curve chunking

The signal-to-noise ratio in the periodograms can be increased by dividing the light curves into small chunks and then averaging over the periodograms from each of the chunks. Chunking enhances signal detection by leveraging the incoherent addition of stochastic noise and the coherent summation of periodic signals across segmented lightcurve periodograms, thereby reducing noise power in the averaged spectrum. The greater the number of chunks, N, the larger will be the signal-to-noise ratio. But N should be chosen wisely because, as the number of chunks increases, the length of the chunk decreases which results in a decrease in the frequency resolution, Δf, of the power spectrum since $\Delta f \propto 1/T$, where T is the total time of the chunk. As the length of the chunk changes, the lowest frequency that can be sampled will be changed, thereby making the periodogram insensitive to very low frequencies or long-term periodicities, and we may lose the superorbital period information. Hence, this method is not well suited for noise reduction in such cases. Also, the averaged periodogram may have a

higher signal-to-noise ratio, but the information of the source variability will be smeared, which is not desirable. The other problem with this method is the presence of colored noise (here, in our case, the red noise) that should be removed before analysis. This can be done with the help of local averaging and rescaling of the periodogram.

3.1.3 Rescaling of the periodogram

Rescaling is one of the most important techniques for suppressing the colored noise component present in the periodogram. For lower frequencies, the power is generally high in the case of colored noise, which has to be removed to detect significant peaks. If it is not removed, then the noise powers corresponding to the lower frequencies will be detected as the significant frequencies. To implement this, the method of local averaging over the log scale is used, as discussed by Israel and Stella 1996 and Wen et al. 2006. The local average gives the underlying noise power, which is used to get the rescaled periodogram. For this, the local average at j^{th} frequency bin is calculated in such a way that the frequency bandwidth to the right and the left of the j^{th} frequency is approximately equal in log scale, i.e.,

$$log(\nu_j) - log(\nu_j - \Delta\nu_{left}) = log(\nu_j + \Delta\nu_{right}) - log(\nu_j) \tag{3.3}$$

$$\Delta\nu_{total} = \Delta\nu_{right} + \Delta\nu_{left} \tag{3.4}$$

where ν_j is the frequency at the j^{th} frequency bin, $\Delta\nu_{left}$ and $\Delta\nu_{right}$ are the frequency bands left and right to ν_j, respectively, and $\Delta\nu_{total}$ is the total bandwidth for calculating the local average.

Fixing $\Delta\nu_{total}$, from Eq. 3.3 and 3.4 $\Delta\nu_{right}$ and $\Delta\nu_{left}$ can be written as

$$\Delta\nu_{right} = \frac{(4\nu_j^2 + \Delta\nu_{total}^2)^{1/2} - (2\nu_j - \Delta\nu_{total})}{2} \tag{3.5}$$

$$\Delta\nu_{left} = \Delta\nu_{total} - \Delta\nu_{right} \tag{3.6}$$

The average of the powers is calculated in both bands, excluding the power from frequency bins $j-2$ to $j+2$. These bins are excluded so that the power does not get rescaled by itself and the nearby powers. Then, the average of both bins is calculated as the local average (P_{la_j}) of the expected continuum power at ν_j.

The original power (P_j) at the frequency v_j is then divided by the local average power to get the periodogram with reduced colored noise. To avoid dividing itself, the powers from $j-2\ to\ j+2$ are excluded, as mentioned above. If we had included the power P_j in the local average, we might have also lost the significant high power peaks. Hence, the rescaled power (P_{re}) is given by:

$$P_{re_j} = P_j / P_{la_j}$$

The interval size, I, which corresponds to the bandwidth Δv_{total} (= $I * frequency\ resolution$) for local averaging, is fixed for every P_j. The choice of I is made on the basis of the fact that the distribution of the rescaled powers follows an exponential distribution, as for the case of white noise as discussed by Israel and Stella 1996. We applied the Kolmogorov-Smirnov test for the distributions of rescaled powers for different values I. This test compares the empirical distribution function of a sample to a known, continuous reference distribution (here, exponential distribution). It tests whether the sample comes from that reference distribution or not. For this, our null hypothesis is that the sample comes from the reference distribution. Higher probability values imply a resemblance between the two distributions. Hence, we searched for the value of I for which the probability is highest for the values in the range of $I = 2$ to $1/10$ th of the total number of independent frequencies.

An example of colored noise reduction for the source X1636-536 is given in Fig. 3.4. The top panel shows the original periodogram, the middle panel shows the local average computed using the aforementioned method, and the bottom panel shows the rescaled periodogram. It is clear from the figure that the powers at lower frequencies are dominant over the powers at higher frequencies in the original periodogram, which are suppressed in the rescaled periodogram.

After the reduction of the colored noise, the significant peaks in the periodogram are searched. This search is done by calculating of false alarm level for the given powers in the periodogram.

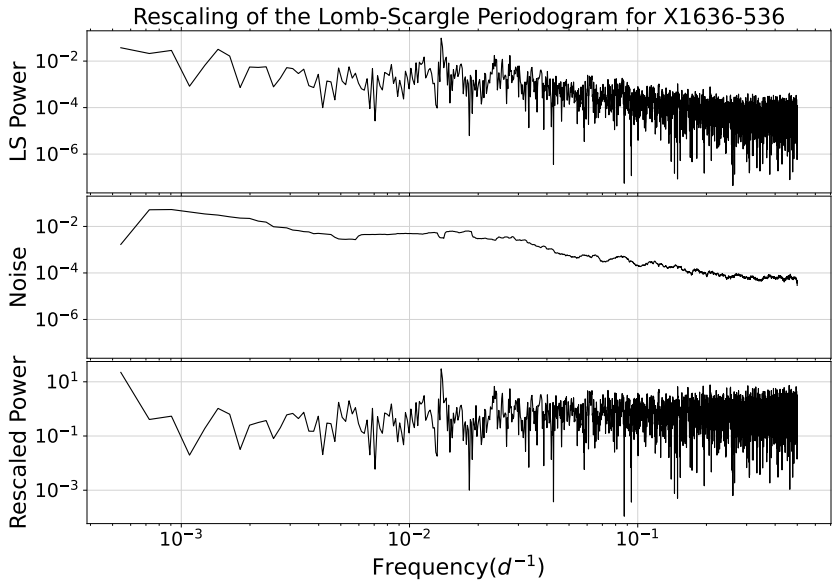

Figure 3.4: Plot showing comparison between the original (top panel) and the rescaled periodogram (bottom panel) for X1636-536. The middle panel shows the underlying noise.

3.1.4 False alarm probability (FAP)

After plotting the rescaled periodogram, the significance of the detected peaks was assessed by calculating their False Alarm Probability (FAP). The probability of finding the value P_0 or more among N independent measurements is known as FAP and is given by Eq. 3.7 for an exponential distribution of powers (Wen et al. 2006). The null hypothesis in this context assumes that the observed peaks in the periodogram arise from noise (only Poissonian or white noise) rather than a true periodic signal. The lower value of FAP signifies the significant detection of periodicity, and higher values signify the noise.

$$FAP = 1 - (1 - e^{-P_0})^N \tag{3.7}$$

To find a significant period, we set the significant threshold power level for FAP as 10^{-5} and compute the periods corresponding to the powers above this level for new detections and FAP as 10^{-3} for previously known periods.

3.1.5 Dynamic Power Spectrum (DPS)

A Dynamic power spectrum, as the name suggests, is a plot that shows the power spectrum at varying times. Or in other words, the DPS is a plot showing the variations in the period over the entire span of the observations (15 years). The intensity of the color in the DPS shows the strength of the powers based on the color bar. In the DPS, we plot the time on the x-axis, periods on the y-axis and the power on the z-axis. The power axis is perpendicular to the plane of the paper. The left panel with the DPS, shown in Fig. 3.6, shows the Lomb-Scargle periodogram of the complete light curve and the green line shows the threshold power level corresponding to FAP = 10^{-5}, and the top panel shows the lightcurve for the source over the 15 year of span. The variations in these DPS show the variations in mechanisms triggering the periodicities.

For plotting the DPS, we used a window of 600 days and a sliding window of 5 days to observe a continuous variation in the source for the same, 1-day averaged data from MAXI. The rescaled periodogram is calculated for all the lightcurves of 600 days. Large window size is not used as a larger window will average out the small signals and the variations in the periodicities will not be visible. The minimum period that can be detected is 2 days and the maximum 600 days. But since the edge effects may results in false detection, periods higher than 200 days in DPS are not shown. One of the disadvantages of this small window is the reduction of the frequency resolution.

3.2 Results from MAXI/ISS

Using the above methodology, we have plotted the rescaled periodogram for the 22 sources with the frequency resolution of $1/T$, where T is the total observation time for each source. The frequencies are plotted on the x-axis, and powers are on the y-axis in arbitrary units. The horizontal green line is the significant power level with FAP as 10^{-5}. Periodic signals with power values exceeding this level are considered statistically significant detections. The detected periods are mentioned in the plots, and the previously known periodicities are discussed in the particular section of the source.

3.2.1 Cen X-3

This is an HMXB with an orbital period of 2.09 days. Superorbital periodicity of ~140 days around MJD 51500 was found by KC11, which could be a part of the evolving period of ~200 days around MJD 51000 reported by them. We have detected the periods of ~2.03, 2.09 and 2.15 days as shown in Fig. 3.5. Among these periodicities, 2.09 days corresponds to the orbital period, and the reason for the other two has to be found. We did not find any of the previously known superorbital periodicities in our study.

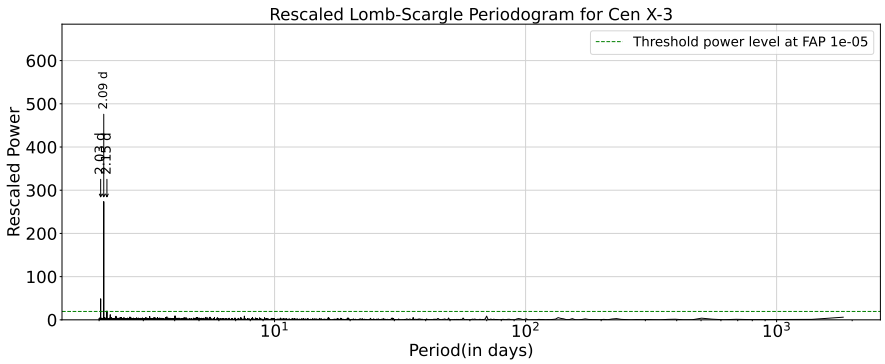

Figure 3.5: Cen X-3: Lomb-Scargle periodogram.

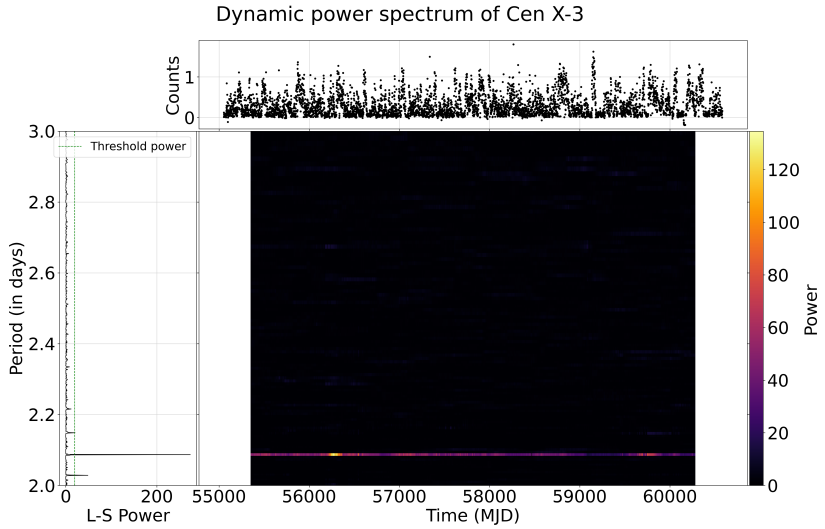

Figure 3.6: Cen X-3: Dynamic power spectrum.

Fig. 3.6 shows no emerging periodicities over time, indicating the source's stability. The 2.09-day orbital period also remains unchanged.

3.2.2 Cyg X-1

The source is an HMXB. The previously detected superorbital periodicities were ~142 days (Ogilvie and Dubus 2001), ~150 days and ~290 days (Lachowicz et al. 2006), and ~326 days (Rico 2008). The periodicities of 150 days and 326 days were also found by KC11. We only detected the orbital period of ~5.6 days (Liu, Paradijs, and E. P. J. v. d. Heuvel 2007) as shown in Fig. 3.7 with FAP of 3.94×10^{-4}. Other periodicities are not found. The DPS in the Fig. 3.8 shows a new period of ~200 days at MJD 57000 and the orbital period is not detected may be due to its weak signal strength.

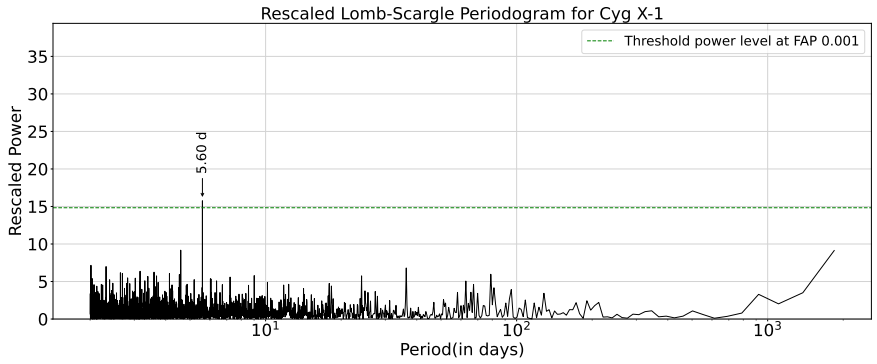

Figure 3.7: Cyg X-1: Lomb-Scargle periodogram.

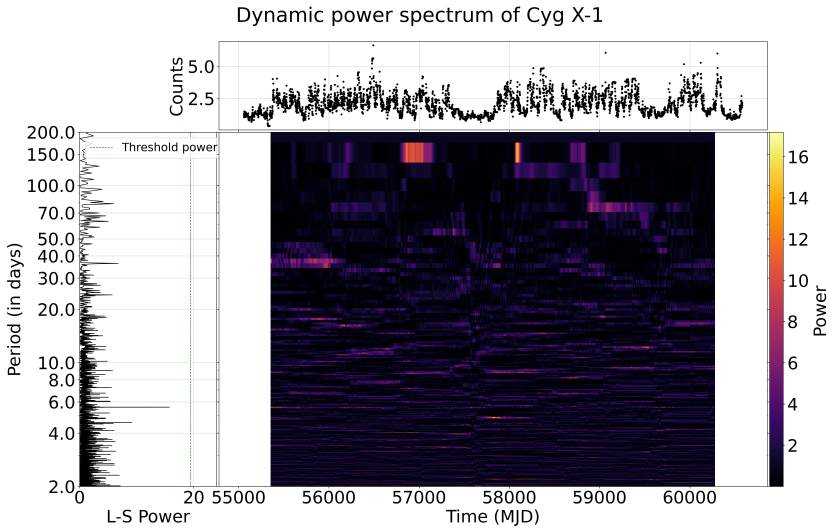

Figure 3.8: Cyg X-1: Dynamic power spectrum.

3.2.3 Cyg X-2

Cyg X-2 is an LMXB system. A range of varying periodicities was previously detected, like ~60–90 days (Wen et al. 2006) and ~40-90 days (KC11). The source has an orbital period of 9.88 days (Liu, Paradijs, and E. P. J. v. d. Heuvel 2007). Smale and Lochner 1992 detected a period of ~77 days, whereas Paul, Kitamoto, and Makino 2000 concluded the absence of any long-term periodicity from RXTE/ASM data. We did not find any of the periodicities as can be seen through Fig. 3.9. Variations in the periods can be seen in the Fig. 3.10, but no strong conclusion can be made about any of the periods.

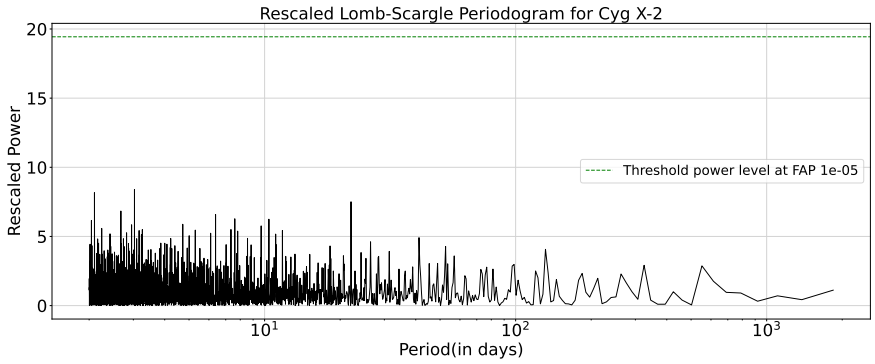

Figure 3.9: Cyg X-2: Lomb-Scargle periodogram.

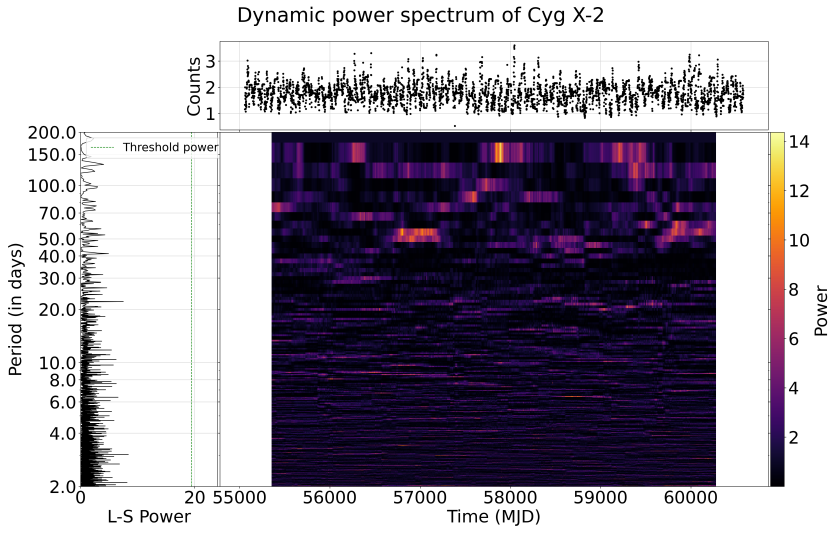

Figure 3.10: Cyg X-2: Dynamic power spectrum.

3.2.4 EXO 0748-676

This is an LMXB source with an orbital period of 3.8 hrs (Liu, Paradijs, and E. P. J. v. d. Heuvel 2007). An unstable superorbital periodicity of ~181 days was detected by KC11 in the high state. The periodicity of 181 days is not detected and the orbital period cannot be detected due to the constraints applied by the sampling interval of the light curve as shown in Fig. 3.11. The DPS (Fig. 3.12) also does not show any significant period as it does not have high power to call a period significant detection.

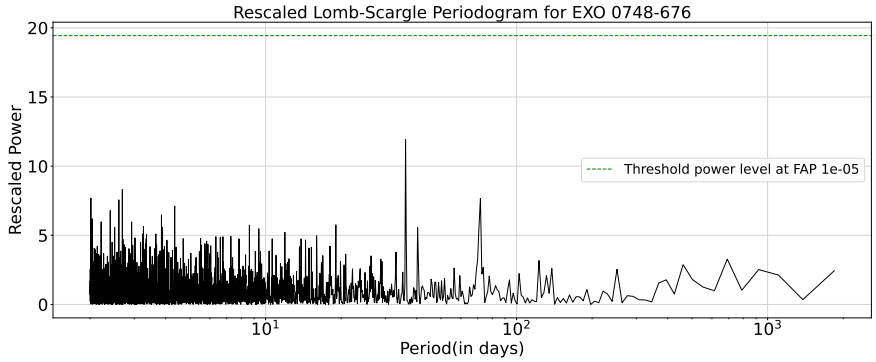

Figure 3.11: EXO 0748-676: Lomb Scargle periodogram

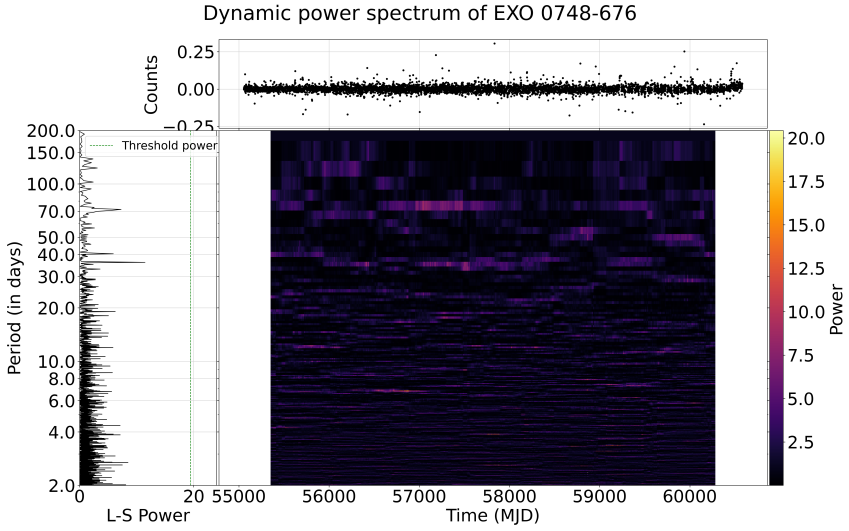

Figure 3.12: EXO 0748-676: Dynamic power spectrum.

3.2.5 GRS 1747-312

This LMXB has an orbital periodicity of 12.36 hr (Liu, Paradijs, and E. P. J. v. d. Heuvel 2007). The superorbital periodicity of ~147 days was found in the initial stages (MJD 50500 and 52000) of the KC11 study, which fades with time. The same period was also detected by Wen et al. 2006. KC11 also detected an evolving periodicity of ~70 days. We did not find any of the periodicities in the Lomb Scargle periodogram (Fig. 3.13), instead, there is a detection of ~24 days of period in the DPS (Fig. 3.14), which is stable throughout the observation. The reason for the periodicity has not been figured out yet.

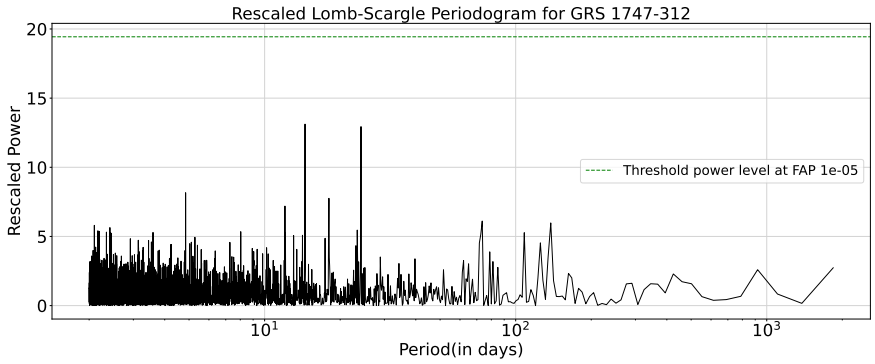

Figure 3.13: GRS 1747-312: Lomb-Scargle periodogram.

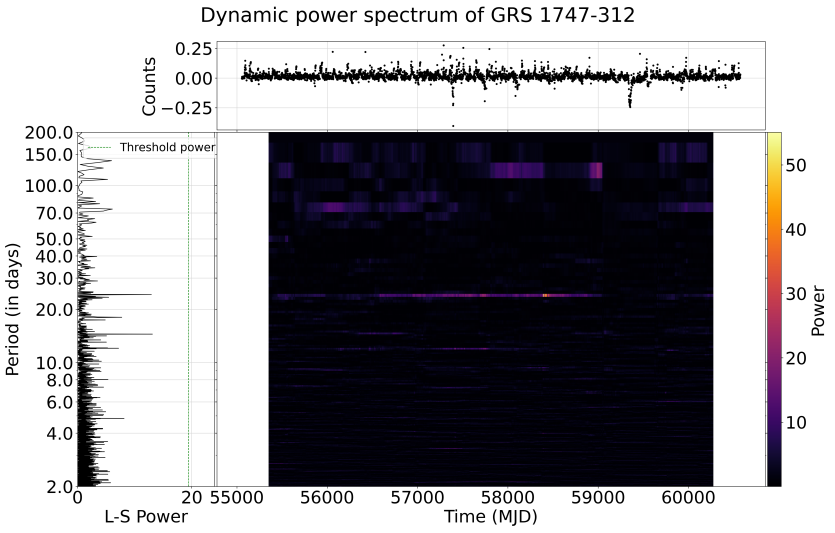

Figure 3.14: GRS 1747-312: Dynamic power spectrum.

3.2.6 GX 339-4

The superorbital period of ~190-250 days was detected by KC11 and by P. Charles et al. 2008 in this LMXB. It has an orbital period of 1.755 days (Liu, Paradijs, and E. P. J. v. d. Heuvel 2007). We did not get any of the detections in our study. It may be due to the presence of high noise in the periodogram even after applying the whitening technique, as can be seen in Fig. 3.15. A period ~70-75 days emerges in Fig. 3.16 , which may an artifact due to the precession of ISS.

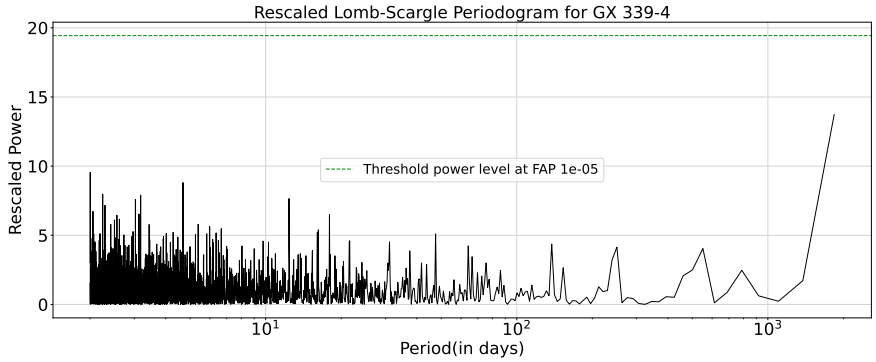

Figure 3.15: GX 339-4: Lomb-Scargle periodogram.

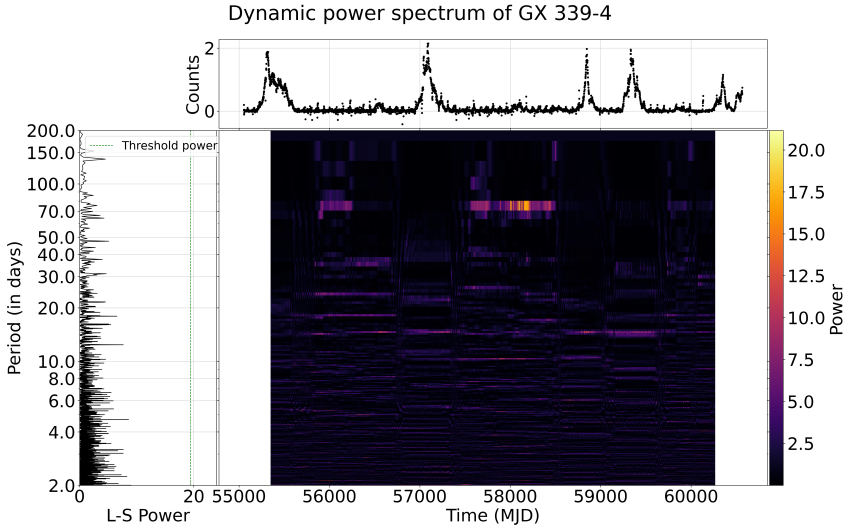

Figure 3.16: GX 339-4: Dynamic power spectrum.

3.2.7 GX 354-0

For this LMXB, periodicities of ~63 and ~70 days were initially detected by KC11 and an evolution from ~50 to ~70 days was there in the later stages of their study. None of the power crosses the significance power level in our study as seen in Fig. 3.17. Fig. 3.18 also does not show any strong period or variation in it.

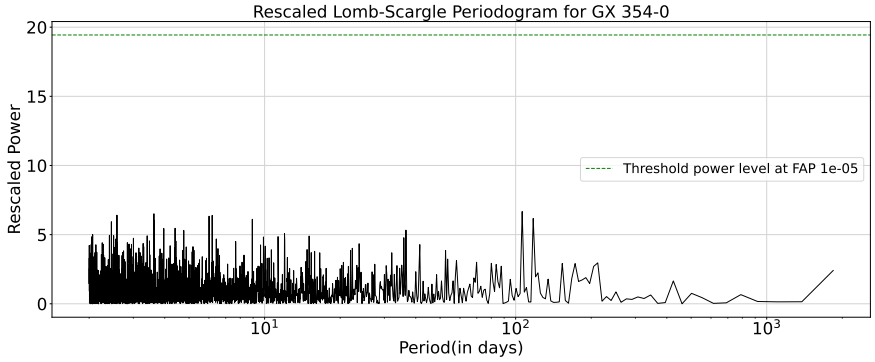

Figure 3.17: GX 354-0: Lomb-Scargle periodogram.

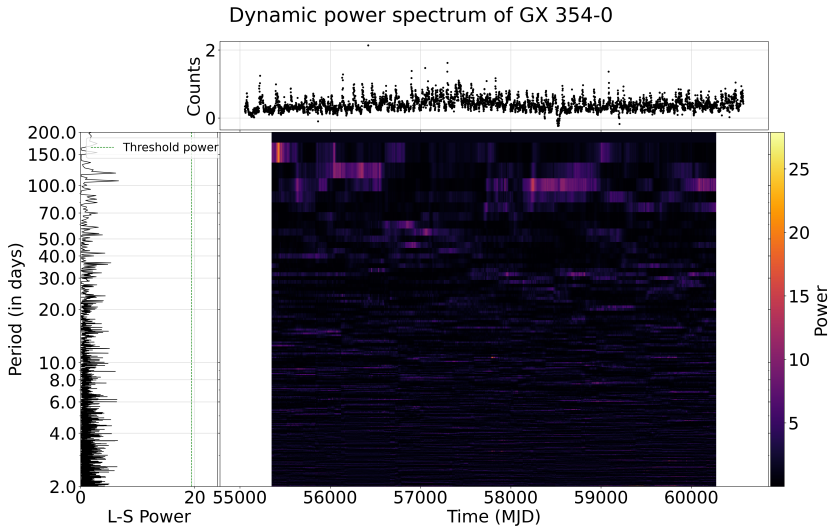

Figure 3.18: GX 354-0: Dynamic power spectrum.

3.2.8 Her X-1

In our study, this LMXB shows some significant peaks at higher frequencies close to each other. We detected the periodicities of ~66.54, 4.74, 17.37, 14.02, 2.51, 2.43, 2.35 and 2.07 days as can be seen in Fig. 3.19. The superorbital period of 34.74 days was previously detected in many studies (not with the exact value of 35 days). The period of 17.37 days is the harmonic of 37.74 days of period. The reasons for the other periodicities are unknown. The orbital period of 1.7 days (Liu, Paradijs, and E. P. J. v. d. Heuvel 2007) is again not detected due to binning constraints. Some of the detected periods can be artifacts like 2.07 days, as the period in this range is found in many other sources as well. Table 3.1 summarizes the list of different candidate artifact periods. The source shows a steady nature in the DPS as well. The period of 66.54 days is not strong enough in Fig. 3.20 to get detected in the 600-day-long long lightcurve.

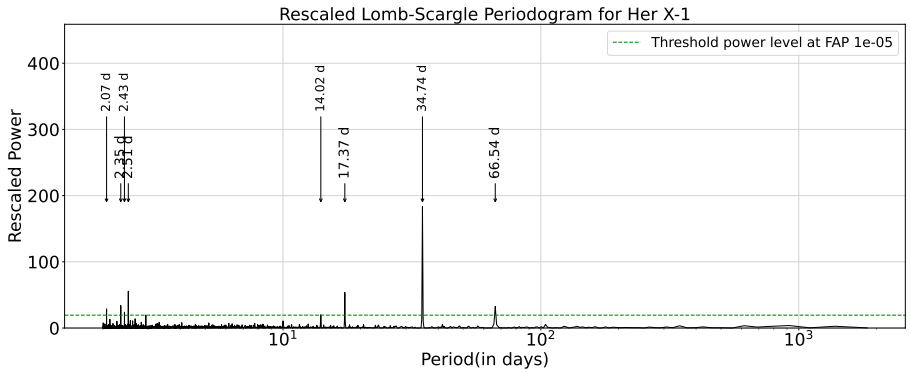

Figure 3.19: Her X-1: Lomb-Scargle periodogram.

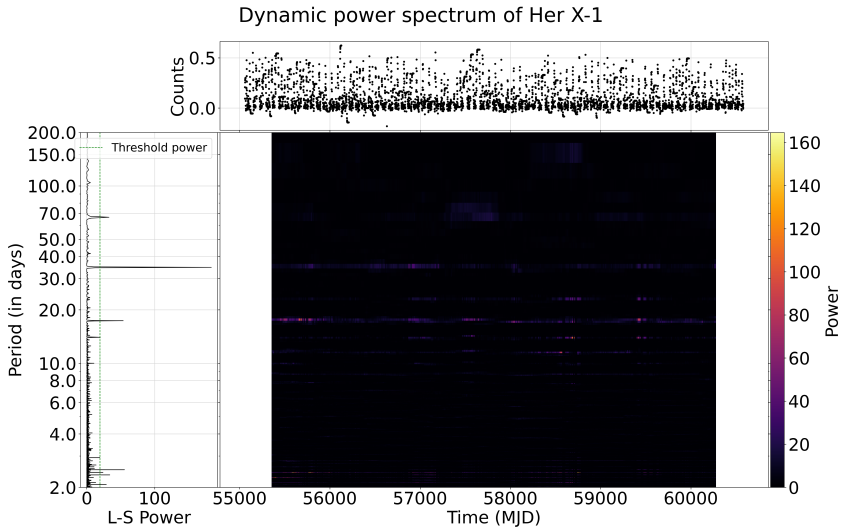

Figure 3.20: Her X-1: Dynamic power spectrum.

3.2.9 KS 1731-260

In this LMXB, the superorbital periodicity of ~38 days was detected around MJD 51000 and an evolving periodicity from ~75-40 days was strongly detected between MJD 51000-52000 by KC11. No periodicity was detected in the later stages of their study (after 52000). We also did not find any periodicity (Fig. 3.21). The DPS also shows nothing as periods as seen in Fig. 3.22. The higher power values lie at the higher periods, where the edge effect from the rescaling periodogram produces discrepancies, and hence are not shown in the plot.

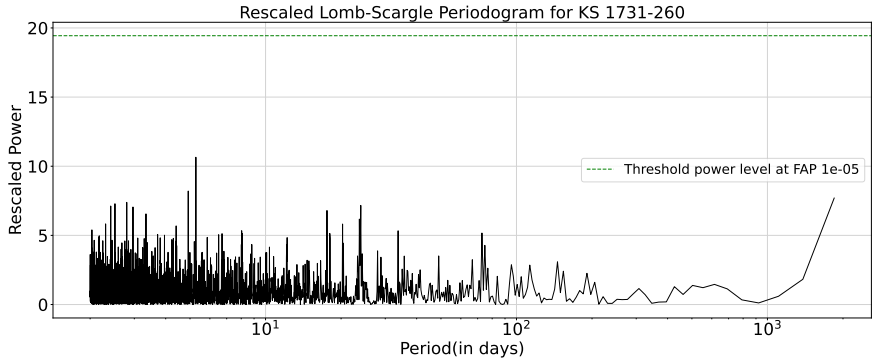

Figure 3.21: KS 1731-260: Lomb-Scargle periodogram.

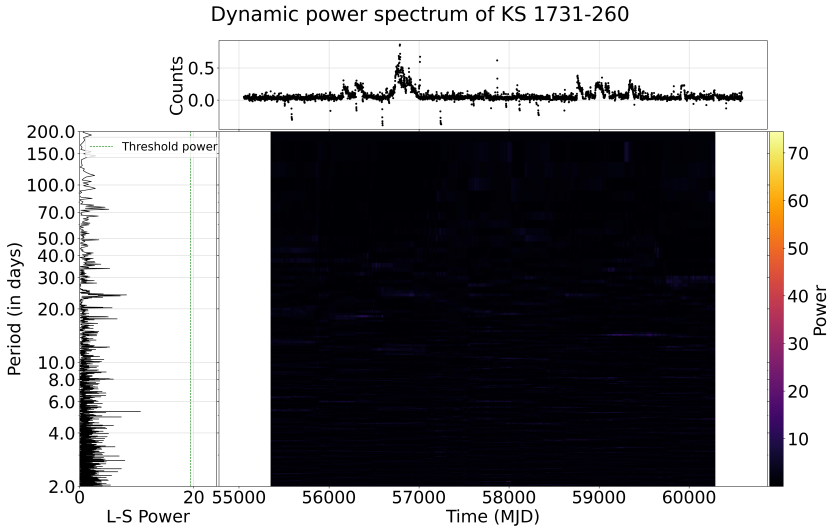

Figure 3.22: KS 1731-260: Dynamic power spectrum.

3.2.10 LMC X-2

The LMXB showed a superorbital periodicity of ~8 days (P. Charles et al. 2008), which is neither detected by KC11 nor by us. We have detected two periodicities of ~72 and ~36 days (Fig. 3.23). The reason for 72 day periodicity might be the precession period of ISS, and 36 days might be its harmonic. The given reason is supported by the detection of these two periodicities in other sources as well, as the same periods in many sources are rare. In Fig. 3.24, 72 days of period is visible throughout the observation. The source shows an unstable behavior as small periods vary over time.

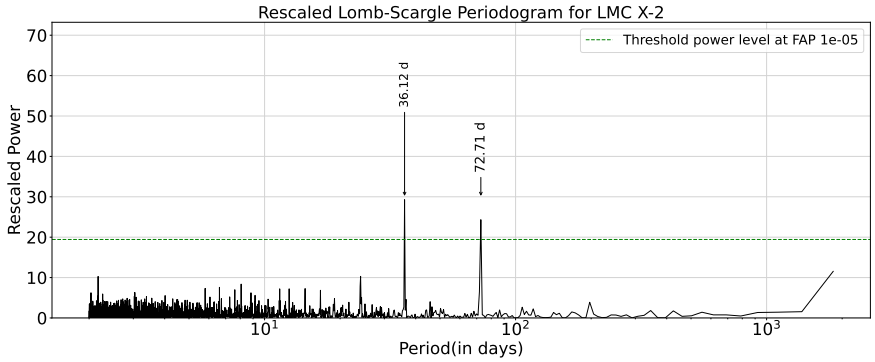

Figure 3.23: LMC X-2: Lomb-Scargle periodogram.

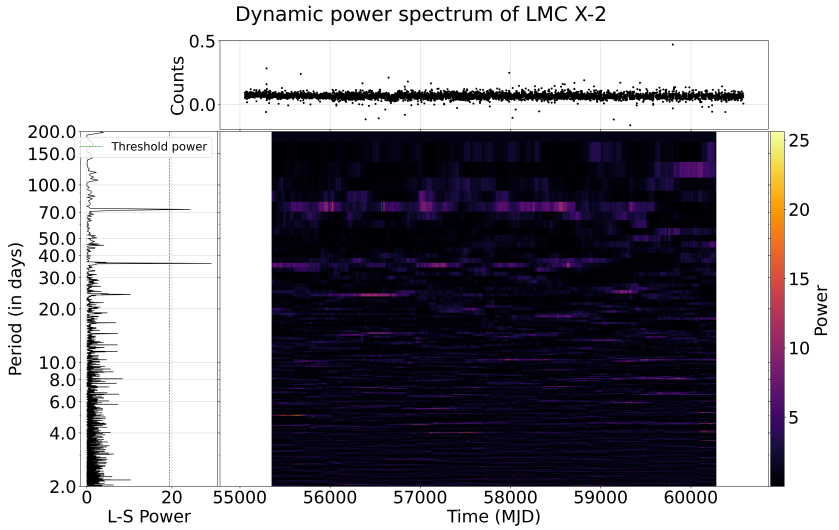

Figure 3.24: LMC X-2: Dynamic power spectrum.

3.2.11 LMC X-3

For this HMXB source, superorbital periodicity of ~99 days was detected by Cowley et al. 1991 and KC11 detected the evolving superorbital periodicities in the range of ~100-500 days (also Wen et al. 2006). None of the peaks in our periodogram crosses the significant level (Fig. 3.25). A periodicity of ~150 days arises around MJD 57000 and then fades in Fig. 3.26.

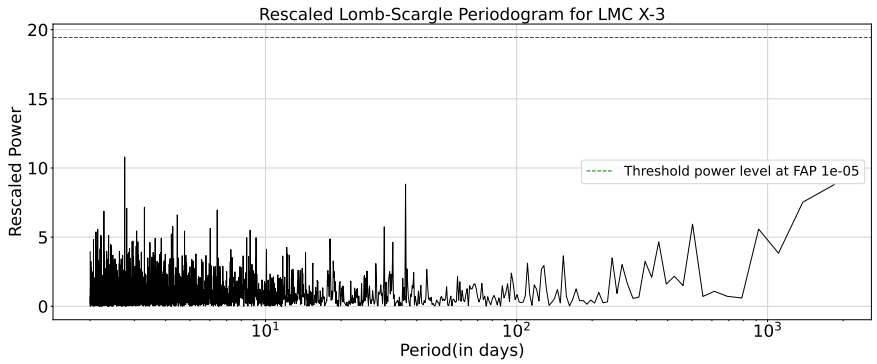

Figure 3.25: LMC X-3: Lomb-Scargle periodogram.

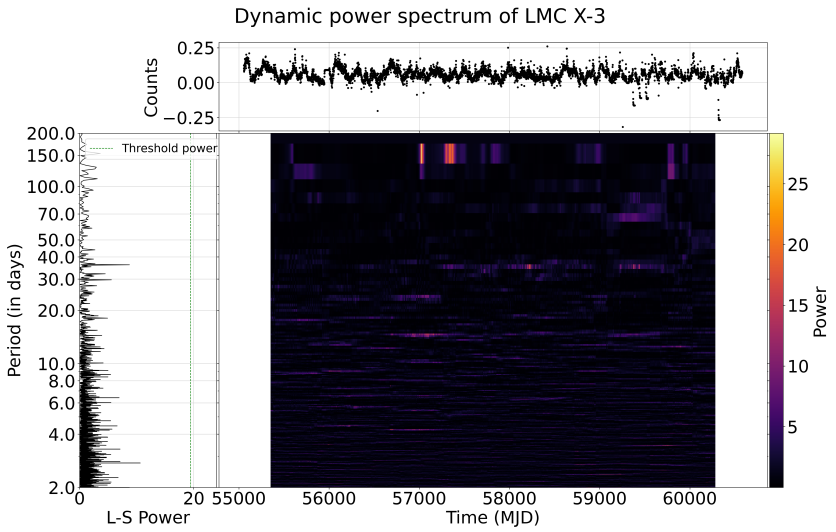

Figure 3.26: LMC X-3: Dynamic power spectrum.

3.2.12 LMC X-4

The HMXB has an orbital period of 1.41 days (Wen et al. 2006), the detection of which in our study is constrained by the binning of the light curve. The superorbital periodicity of ∼30 days was detected by Wen et al. (2006) and KC11. We also detected this periodicity at 30.36 days and its harmonic at 15.18 days. Other than this, we detected significant signals at the periods of ∼52, 51 and 21 days, which can be seen in Fig. 3.27. These were not detected in either of the above-cited papers. The reasons for these periods have not yet been found. Fig. 3.28 shows a stable period of 30 days. Periods that are not detected in the DPS may simply lack sufficient strength.

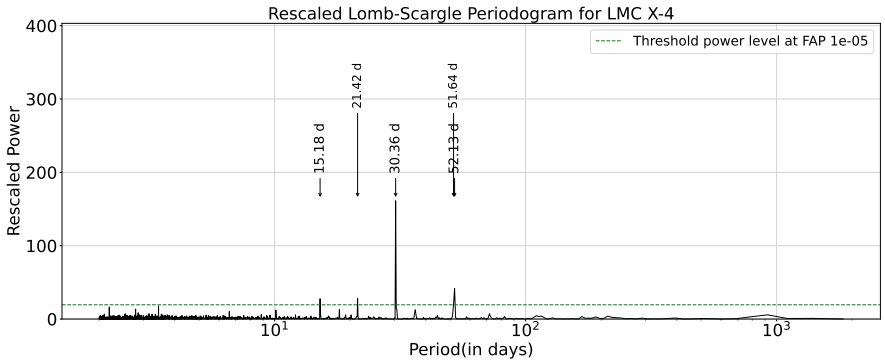

Figure 3.27: LMC X-4: Lomb-Scargle periodogram.

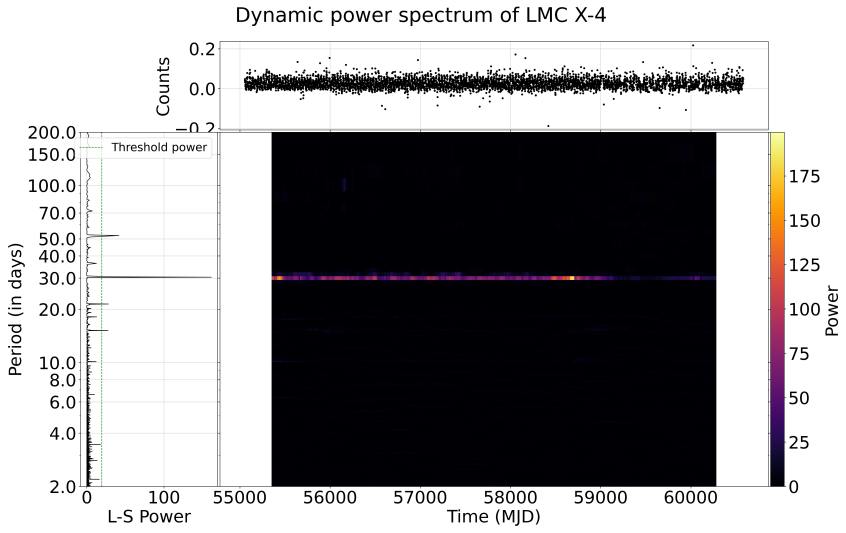

Figure 3.28: LMC X-4: Dynamic power spectrum.

3.2.13 Sco X-1

The previously detected periodicity of 2.6 days (Kudryavtsev et al. 1989) is neither detected by KC11 nor by us for this LMXB. KC11 strongly detected the periodicity of ~200 days. This is also not detected in our study. We detected a periodicity of ~72 days with $FAP < 10^{-3}$(Fig. 3.29), which can be again due to the precession of ISS as discussed for LMC X-2. Further justification is needed for this period. Fig. 3.30 also shows the variation in the same period after MJD 580000.

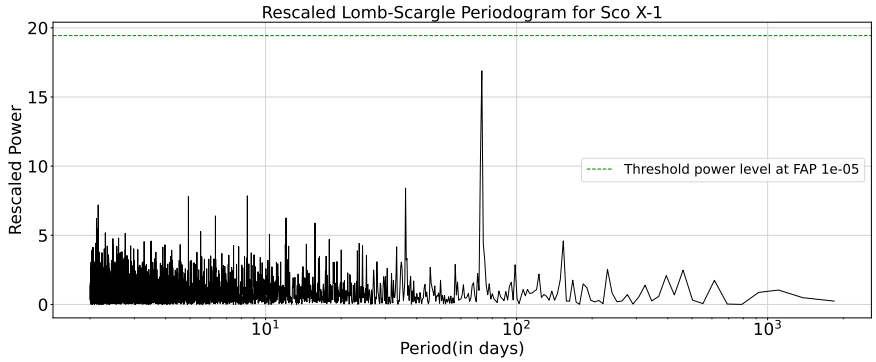

Figure 3.29: Sco X-1: Lomb-Scargle periodogram.

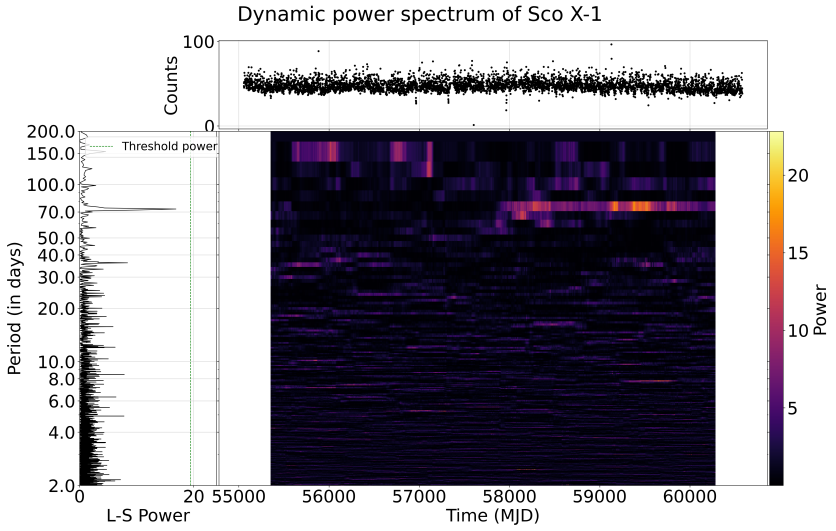

Figure 3.30: Sco X-1: Dynamic power spectrum.

3.2.14 SMC X-1

For this HMXB source, periodicities in the range of ~50-70 days were found by Wen et al. 2006, and KC11 strongly detected the presence of evolving periodicities in the range of ~42-70 days. A quasi-periodicity of ~60 days was suggested by Gruber and Rothschild 1984 and was confirmed by Wojdowski et al. 1998 and Clarkson et al. 2003. Wen et al. reported a quasi-periodicity around ~56 days. We detected the periodicities of ~4.19, 3.89 and 2.06 days in Fig. 3.31, among which 3.89 days is the orbital period (Schreier et al. 1972). The other periodicities were not detected previously. There is a detection of a superorbital period of ~65 days in the Fig. 3.32 with varying power over time.

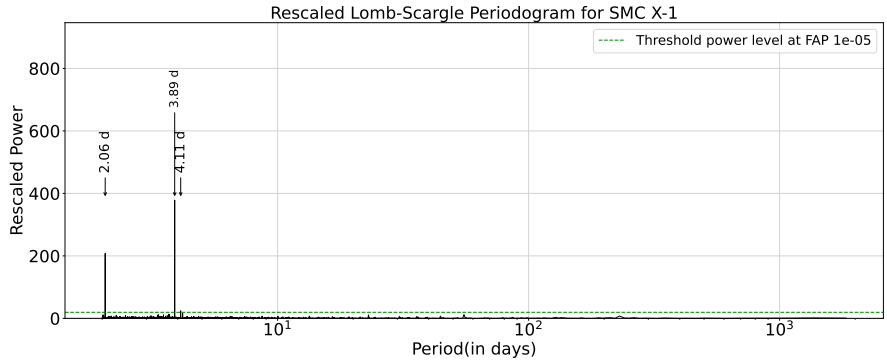

Figure 3.31: SMC X-1: Lomb-Scargle periodogram.

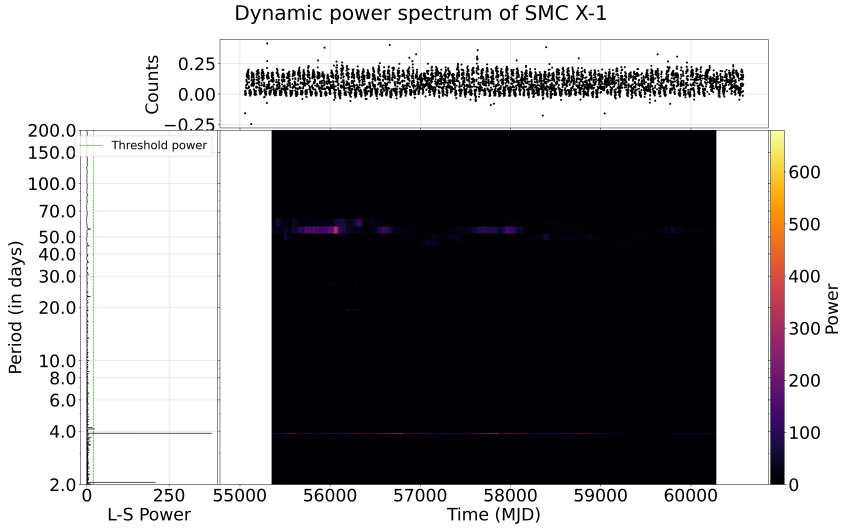

Figure 3.32: SMC X-1: Dynamic power spectrum.

3.2.15 SS433

The superorbital periodicity of ~162 days was strongly detected by Wen et al. 2006 and KC11, which is the relativistic jet precession period (Margon 1984). The HMXB source has an orbital period of 13.1 days (Crampton, Cowley, and Hutchings 1980). KC11 reported a strong period of ~400 days when the period of 162 days is weakly detected, suggesting some correlation between the two periods. The period of 162 days in detected with the $FAP < 10^{-5}$, whereas the orbital period and its harmonic is detected with $FAP < 10^{-3}$ as can be seen from Fig. 3.33. The source shows high variability at different periods other than the superorbital period of ~ 162 days in Fig. 3.34.

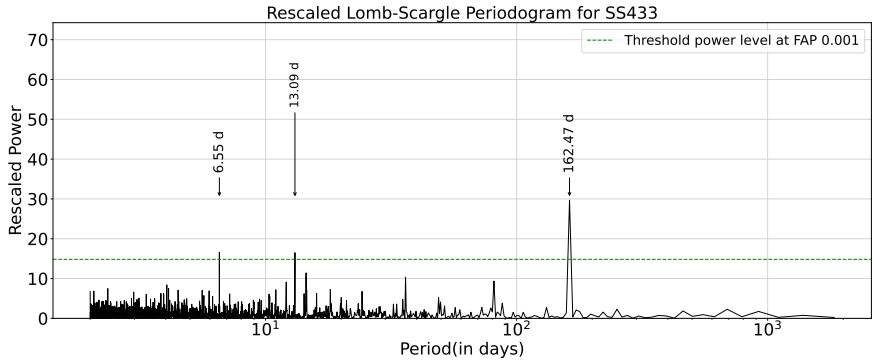

Figure 3.33: SS433: Lomb-Scargle periodogram.

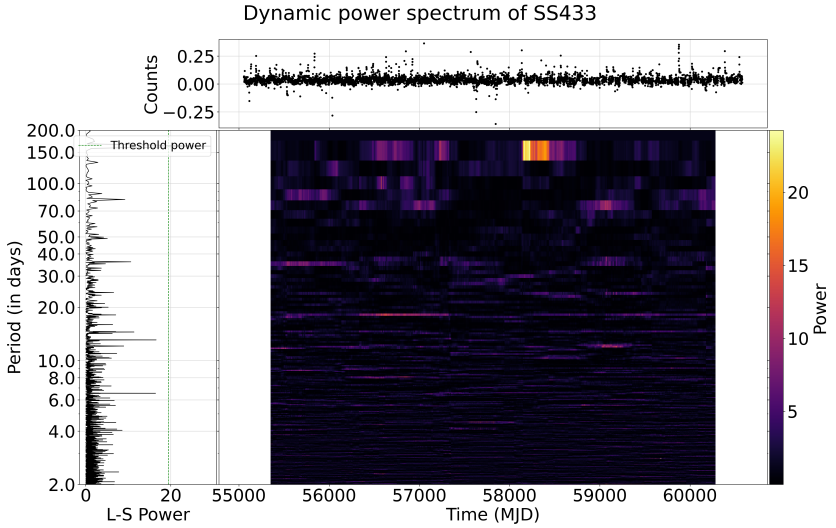

Figure 3.34: SS433: Dynamic power spectrum.

3.2.16 X0114+650

We have detected only the orbital period of 11.6 days (Wen et al. 2006) for this HMXB. There was a strong detection of ~30.8 days superorbital period by Wen et al. 2006 and an alternate weak and strong detection by KC11. This period is detected with the $FAP < 10^{-3}$ (Fig. 3.35). Other than this, period of ~36 days, which is thought to be an artifact, is also detected with the same FAP. Fig. 3.36 shows the dominant period of ~72 days (the candidate artifact) and a continuous and stable orbital period with low power till MJD 58000.

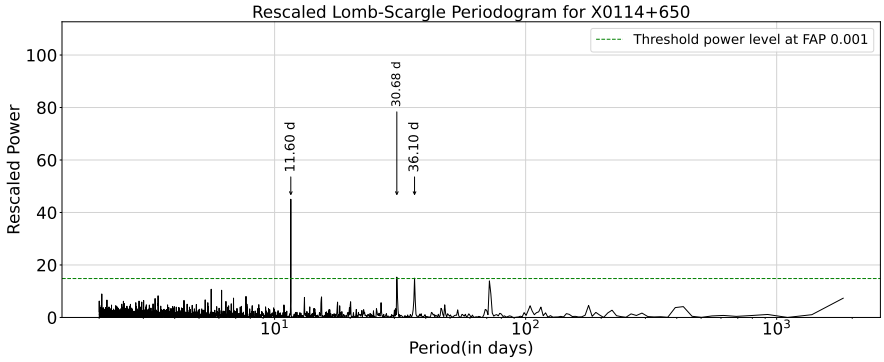

Figure 3.35: X0114+650: Lomb-Scargle periodogram.

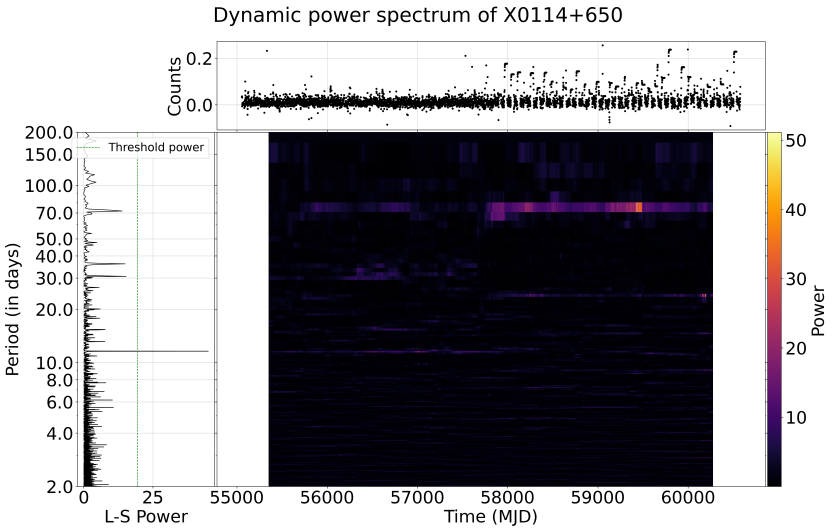

Figure 3.36: X0114+650: Dynamic power spectrum.

3.2.17 X1636-536

The superorbital periodicity of ~46 days for this LMXB was detected by P. Charles et al. 2008 and also by KC11 in the time range MJD 53000–54000. Fig. 3.37 shows a significant period at ~72 days, which is the artifact as discussed above and a superorbital period of ~1840 days, which might be the noise raised due to edge effects in the rescaling of the Lomb-Scargle period. Robust evidences are required to confirm that this period is an intrinsic characteristic of the XRB.Fig. 3.38 shows the variations in the artifact and the evolution of 1840 days of period cannot be detected due to the window size constraints.

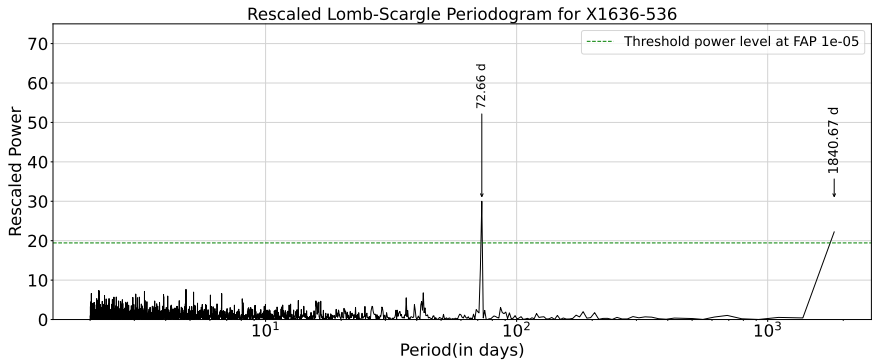

Figure 3.37: X1636-536: Lomb-Scargle periodogram.

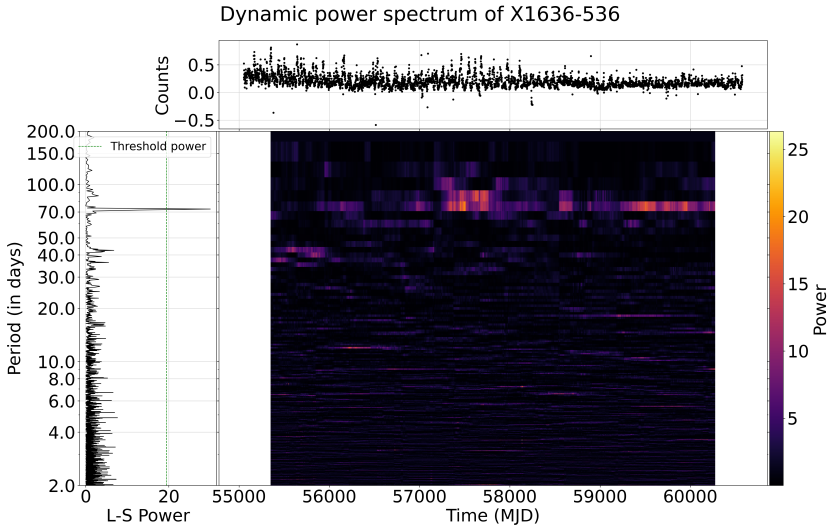

Figure 3.38: X1636-536: Dynamic power spectrum.

3.2.18 X1730-333

This is an LMXB in which a superorbital periodicity of ~217 days was detected by Wen et al. 2006 (and references therein) and in the early stages of the KC11 study. A period of ~100 days was also strongly detected by KC11. There is no significant period detected in the complete lightcurve (Fig. 3.39), but in Fig. 3.40 a period around 100 days is detected in-between MJD 58000 to 59000. This can be due to the same reason as the previous one. This assertion lacks robustness, as KC11 observed that the period evolves. The only supporting argument is the possibility that the underlying mechanism has re-initiated.

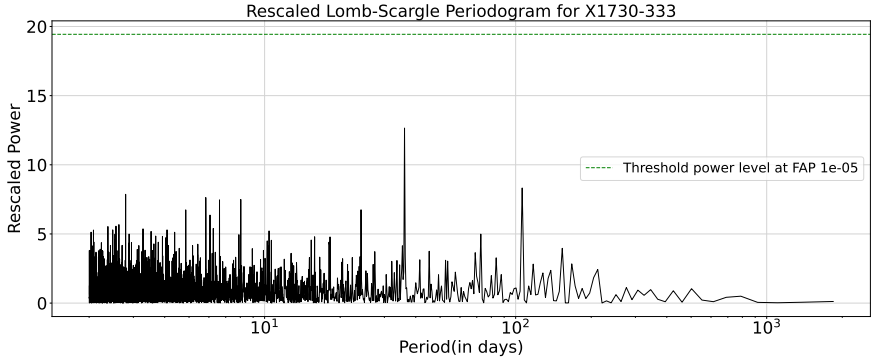

Figure 3.39: X1730-333: Lomb-Scargle periodogram.

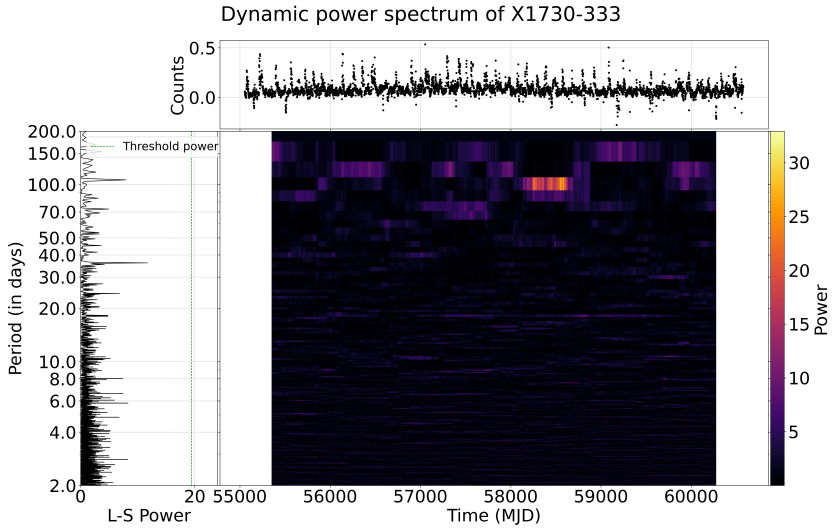

Figure 3.40: X1730-333: Dynamic power spectrum.

3.2.19 X1907+097

In this HMXB, there was a superorbital periodicity of ~42 days (Priedhorsky and Terrell 1984). This is not detected in our study. We have detected the periodicities of ~72.70, 36.11, 8.37 and 4.19 days as seen in Fig. 3.41. Among these periods, 8.37 days is the orbital period (Liu, Paradijs, and E. P. J. v. d. Heuvel 2007) and 4.19 days can be the harmonic of it. Periodicity of 72.70 and 36.11 days can be the above-discussed artifacts. Fig. 3.42 shows a period of ~24 days, which is detected in the Lomb-Scargle periodogram of the entire lightcurve with $FAP < 10^{-3}$. Also the periodicity fades away after MJD 58000.

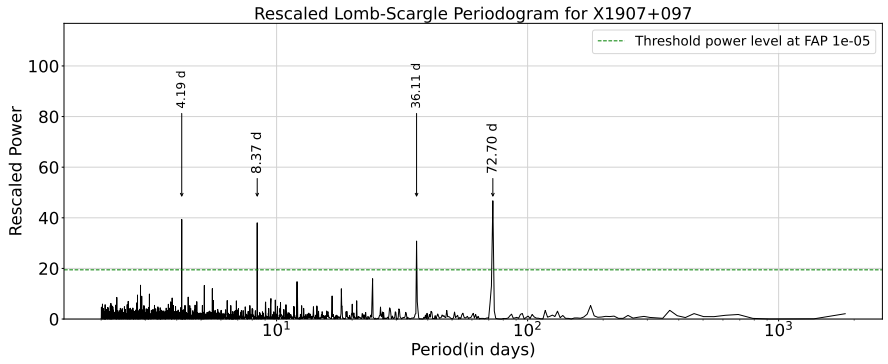

Figure 3.41: X1907+097: Lomb-Scargle periodogram.

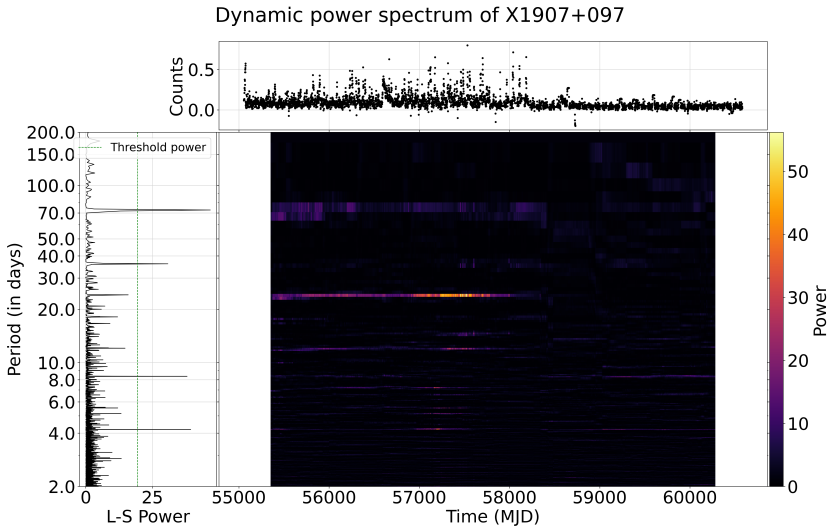

Figure 3.42: X1907+097: Dynamic power spectrum.

3.2.20 X1916-053

The LMXB source had a periodicity of ~5 days (P. Charles et al. 2008) and ~199 days (Priedhorsky and Terrell 1984). KC11 also detected the 199 day period but only in the initial stages of their study and no evidence of 5 day period was found by them. In our study, no power crosses the threshold power level. A period of ~70 days and ~36 days again seen in the DPS shown in Fig. 3.44. In addition to these, a period of around ~19 days is also detected with varying power. The DPS shows high power of different periods around MJD 58000 to 58500, and then again around MJD ~59100-60000, implying high variation in the source in this particular interval of time. The simultaneous appearance and disappearance of these periods suggest a possible underlying correlation between them.

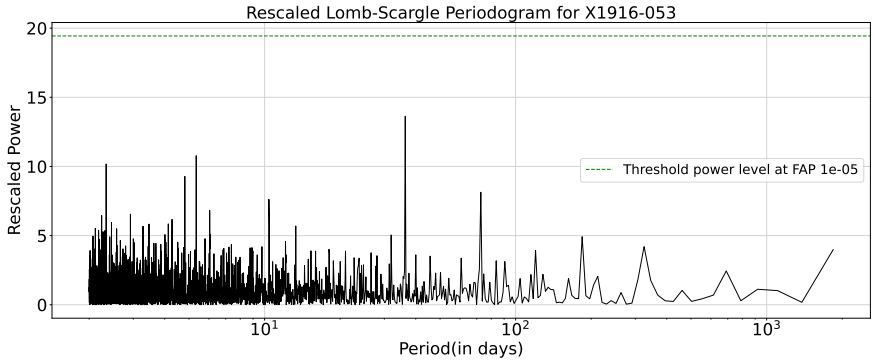

Figure 3.43: X1916-053: Lomb-Scargle periodogram.

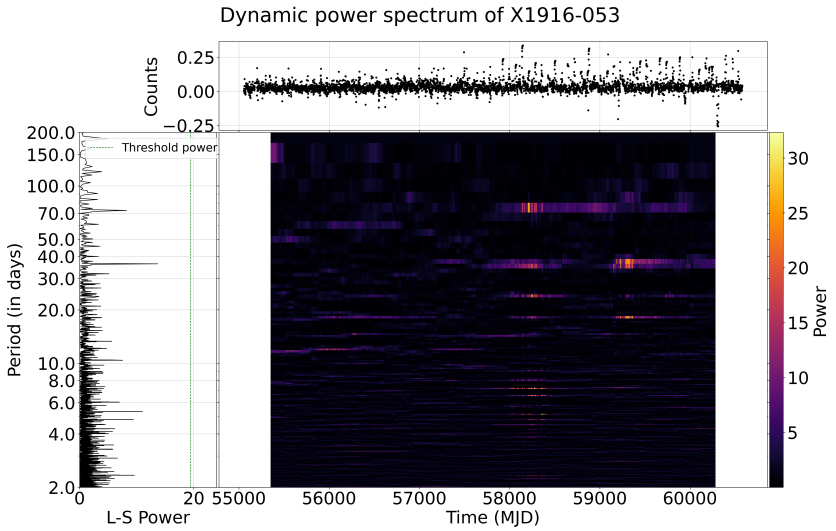

Figure 3.44: X1916-053: Dynamic power spectrum.

3.2.21 X1957+115

The superorbital periodicity of ~117 days was found by P. Charles et al. 2008 in this LMXB. Also, this periodicity was only detected initially by KC11. We did not detect any periodicity for the source as shown in Fig. 3.45. The DPS, Fig. 3.46 shows high variabilities in the periods in wide ranges of days. This variation can be mainly due to noise, as no power is highly dominating.

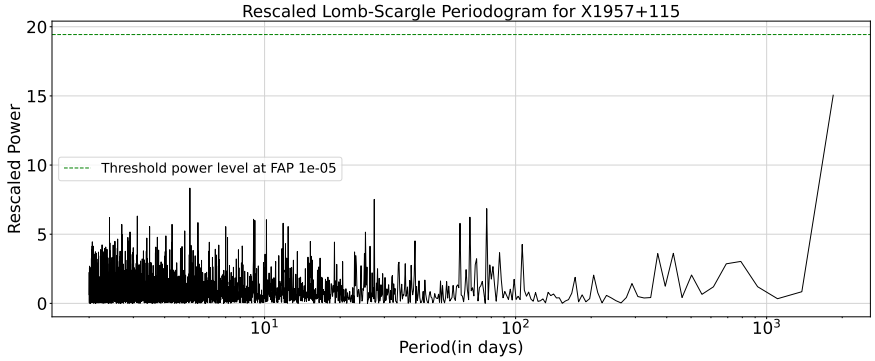

Figure 3.45: X1957+115: Lomb-Scargle periodogram.

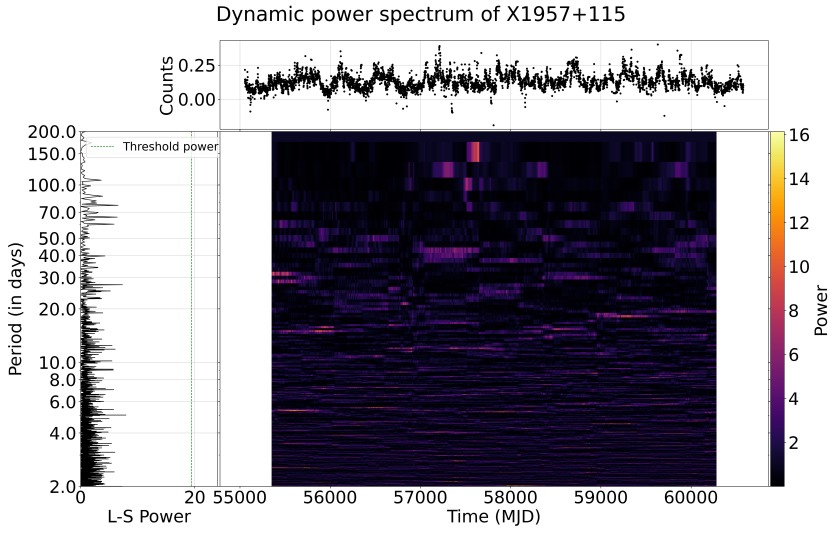

Figure 3.46: X1957+115: Dynamic power spectrum.

3.2.22 XTE J1716-389

The HMXB source had a superorbital periodicity of ~99 days (Wen et al. 2006). KC11 detected this periodicity initially, but it went weaker with time. The source does not show any stable period, neither in Lomb-Scargle periodogram (Fig. 3.47) nor in DPS (Fig. 3.48).

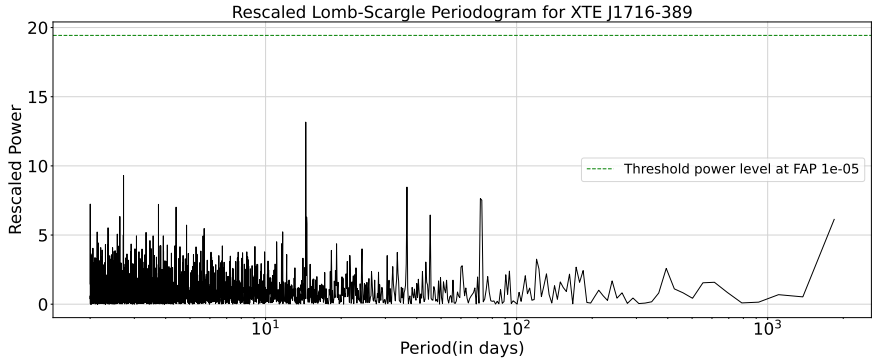

Figure 3.47: XTE J1716-389: Lomb-Scargle periodogram.

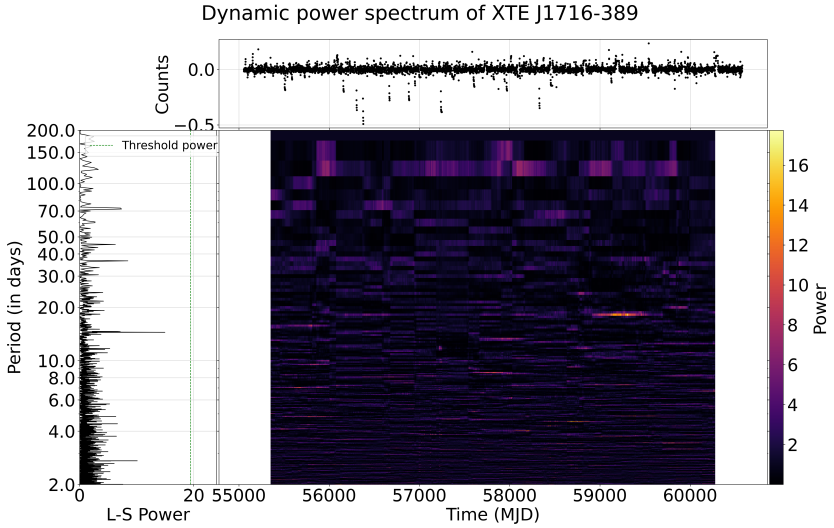

Figure 3.48: XTE J1716-389: Dynamic power spectrum.

The following table summarizes the detected periodicities in our study with their corresponding FAP. **Black represents new detected periodicities, blue represents previously known periodicities we also detected with FAP < 10^{-5}, green represents previously known periodicities we also**

detected with FAP < 10^{-3}, red represents the periodicities that can be artifacts.

Source	**Detected periods (in days)**	**FAP**
Cen X-3	2.15	3.16e-06
	2.09	3.71e-116
	2.03	1.91e-18
Cyg X-1	5.60	3.94e-04
Her X-1	66.54	1.6e-11
	34.74	5.4e-77
	17.37	1.25e-20
	14.02	5.59e-06
	2.51	1.90e-21
	2.43	1.07e-07
	2.35	4.75e-12
	2.07	7.75e-10
LMC X-2	72.71	7.48e-08
	36.12	5.30e-10
LMC X-4	52.13	1.93e-15
	51.64	4.74e-06
	30.36	2.52e-67
	21.42	1.41e-09
	15.18	2.56e-09
SMC X-1	4.11	7.20e-08
	3.89	1.06e-161
	2.06	1.06e-87
SS433	162.47	3.46e-10
	13.09	1.88e-04
	6.55	1.68e-04
X0114+650	30.68	5.78e-04
	11.60	7.38e-17
X1636-536	1840.67	6.12e-07
	72.66	2.57e-10
X1907+097	72.70	1.40e-17
	36.11	1.14e-10
	8.371	8.49e-14
	4.19	2.18e-14

Table 3.1: Detected periodicities with their corresponding FAP.

The above analysis demonstrates that both the periodogram and the Dynamic Power Spectrum (DPS) reveal repeating patterns in the source flux and their evolution over the course of the observation. However, these techniques do not provide insights into the origin or mechanism of the emission. To gain information about the emitting region within the system, it is essential to study the energy dependence of these periodicities, as discussed in the following section.

3.3 Energy dependence of the periodicities

The energy dependence of periodicities provides crucial insights into the origin of the emission at specific frequencies. To investigate this, we computed the fractional amplitude of the detected periodicities across different energy bands (2-4, 4-10, and 10-20 keV). This was achieved by phase-folding the lightcurves at the detected periods and fitting them with single or multiple sinusoidal components, optimizing for a reduced chi-square value close to 1 in each energy band. The fractional amplitude was then obtained by dividing the fitted optimized amplitude by the offset of the sinusoid.

A higher fractional amplitude indicates greater variability in a particular energy band. An increasing trend with energy suggests that the periodic modulation originates from hard X-ray photons, likely emitted from the hotter and inner regions of the accretion disk or potentially from the corona. Given that superorbital periodicities are generally disk-driven, the disk remains the more probable source. Conversely, a decreasing fractional amplitude with energy points to soft X-ray emission, typically arising from the cooler and outer regions of the accretion disk.

Fig. 3.49 shows phase phase-folded lightcurve in four different energy bands for source Cen X-3 at period 2.09 day. The top panel, for each energy band, shows black curve as the sum of all the photons in a particular phase bin and the red curve shows the fitted model, a sinusoid, with single or multiple sine functions. The number of sinusoids used to fit the phase-folded light curve is based on the value of reduced chi-square.

Reduced chi-square is a statistical test used to check the goodness-of-fit depending on the number of unknown parameters in the model. Reduced chi-square is calculated in the following steps:
Weighted residual, χ, is calculated, which is a measure of the difference between observed data and a model prediction, adjusted by the uncertainty (or weight) of each data point.

$$\chi = \frac{O_i - E_i}{\sigma_i} \tag{3.8}$$

where O_i is the observed value, E_i is the expected value and σ_i is the error in the observed value for the ith data point. The smaller the value of χ, the

more the data point lies toward the fitted model. Then, for the complete data set with N number of data points, chi-square value is calculated as:

$$\chi^2 = \sum_{i=1}^{N} \left(\frac{O_i - E_i}{\sigma_i} \right)^2 . \tag{3.9}$$

If p is the number of parameters in the model, the degree of freedom (dof) is calculated as

$$dof = N - p \tag{3.10}$$

and the reduced chi-square, χ^2_{red}, is then given by

$$\chi^2_{red} = \chi^2 / dof . \tag{3.11}$$

χ^2_{red} values $<< 1,\ \approx 1\ and\ \ >> 1$ show over-fitting, good-fitting and under-fitting of the model, respectively.

To achieve a good fit, we attempted to bring the reduced chi-square (χ^2_{red}) value closer to 1. However, in some cases where the photon counts are high with low errors, or fluctuations in the baseline (e. g., fluctuations at the top and bottom of sinusoid nature in Fig. 3.49), the χ^2_{red} value remains above 2 or goes higher, even after trying better models. The same can be seen from the phase folded lightcurves of all the sources, where the χ^2_{red} (given in the caption) is the highest in the 2-20 keV band, as this band has the highest count among all the energy bands. For high values of $\chi^2_{red} > 2$, a minimum of values is considered for the study.

The fractional amplitude has been analyzed only for the periods, which shows a good periodic nature in phase-folded lightcurves in the energy band 2-20 keV. Cyg X-2 shows no variations periodic nature in the phase-folded light curves for the detected 5.6 day period, LMC X-2 has two candidate artifact periods, ~36 and 72 days, and the very long-term period of ~1840 days in X1636-536 also does not show any periodic behavior. Hence, energy dependence analysis is not made for these sources.

The following subsections show the fractional amplitude of different sources in different energy bands.

3.3.1 Cen X-3

The period which shows a well periodic nature in the phase folded lightcurve is only 2.09 days. Fig. 3.49 shows the folded lightcurve of Cen X-3 at a period of 2.09 days. From the figure, it can be seen that the count rate is high compared to the error. This creates a bias in calculating the χ^2_{red} as discussed above. The χ^2_{red} values are given in the caption of the figures.

For the same period, Fig. 3.50 shows the fractional amplitude for the combination of four different sinusoids (one with fundamental frequency and three with harmonics) used to fit the phase-folded light curve. $a1$ is the fundamental amplitude, $a2$, $a3$ and $a4$ are the harmonics amplitudes, and $a0$ is the offset of the fitted model. Among all the amplitudes, only $a1$, the fundamental amplitude, shows some significant change in fractional amplitude. The other amplitudes have significant errors, showing no change in the fractional amplitude.

The decreasing order of fractional amplitude with energy for the fundamental amplitude shows that the mechanism producing the period is dominated in softer X-rays.

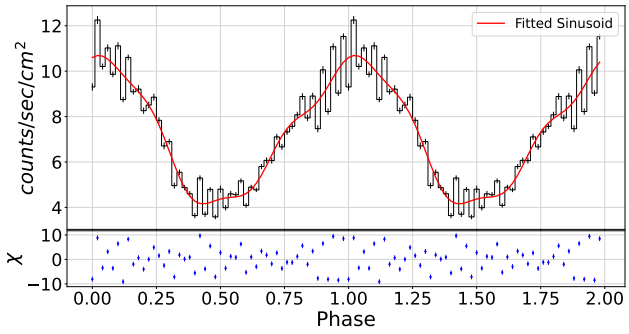

(a) Energy: 2-4 keV; χ^2_{red} = 31.62.

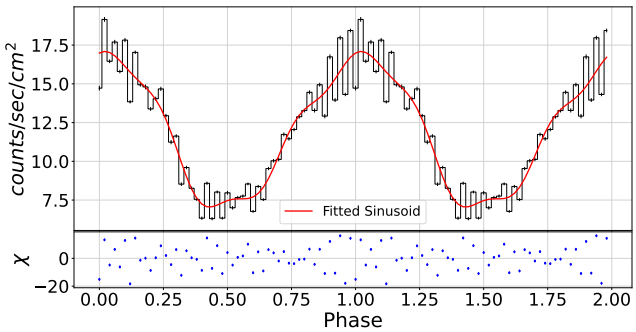

(b) Energy: 4-10 keV; χ^2_{red} = 95.47.

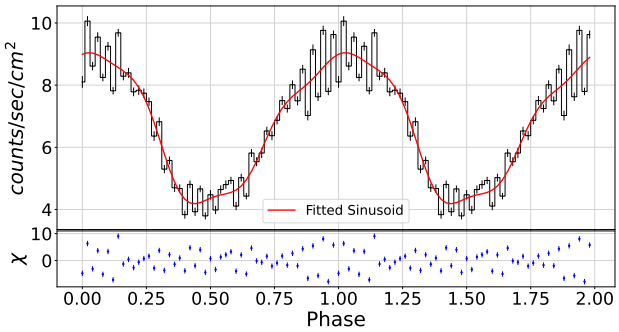

(c) Energy: 10-20 keV; χ^2_{red} = 19.22.

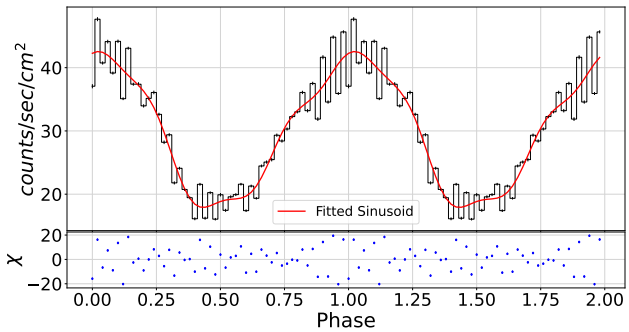

(d) Energy: 2-20 keV; χ^2_{red} = 125.97.

Figure 3.49: Phase folded lightcurve for Cen X-3 at period ~2.09 days.

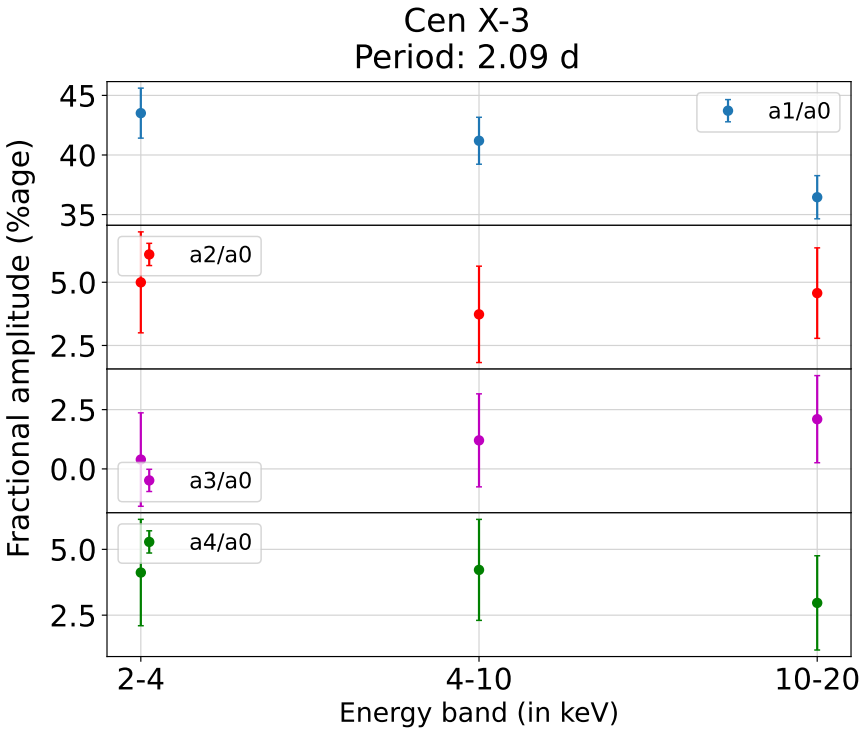

Figure 3.50: Fractional amplitude for period 2.09 days.

3.3.2 Her X-1

The source shows many different periodicities, among which, periods ~2.34, 2.42, 2.51, 14.01, 34.75 and 66.54 days showed periodic patterns. From Fig. 3.51 to 3.56 show the folded lightcurves at different periods in different energy bands. All energy bands exhibit similar behavior across the periods, except for the 34.74-day period, which shows a distinct peak and hump. The errors in band 2-20 keV for the period 2.43, 2.51, 14.02 and 66.54 days show relatively higher errors than other bands, showing a large deviation of the observed values from the model in this band.

Fig 3.57 and 3.58 show the fractional amplitude for these periods. For period 2.35 and 2.43 days, fractional amplitude is higher in the energy band 2-4 keV, but does not show any significant change from 4-10 to 10-20 keV energy band. Hence, showing that the periods are arising due to softer X-rays and produced equally in the other two energy bands. Whereas, periods 2.51 and 14.02 days have large error bars, having the same value within the limits of uncertainty, hence the mechanisms producing these periods are equally radiating in the three bands.

Fig. 3.58a The figure displays four distinct fractional amplitudes corresponding to four different sine components. It is evident that the variations in $a1$ and $a2$ exhibit a similar pattern, suggesting a possible correlation between them. Likewise, $a3$ and $a4$ also follow a comparable trend, indicating a potential correlation within that pair as well. Also, the decrease of the fractional amplitude suggests the signals are dominantly produced by the softer X-rays or the thermal component.

From Fig. 3.58b, it can be seen that the fractional amplitude does not show any significant change from 4-10 to 10-20 keV for $a1$, whereas $a2$ and $a3$, both have similar values of fractional amplitude in 2-4 and 4-10 keV and decrease in the band 10-20 keV.

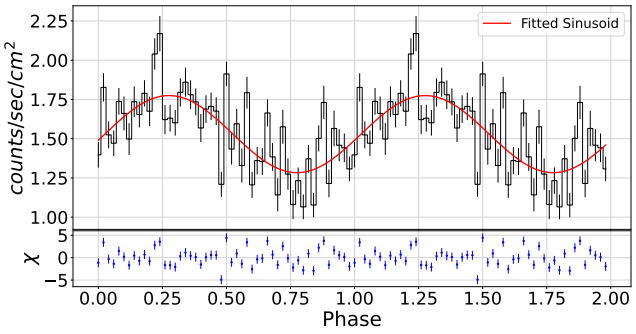

(a) Energy: 2-4 keV; χ^2_{red} = 4.18.

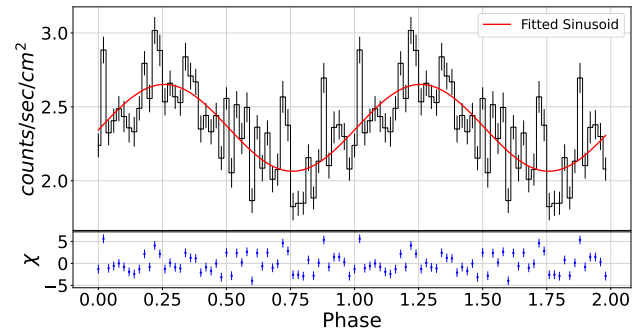

(b) Energy: 4-10 keV; χ^2_{red} = 5.53.

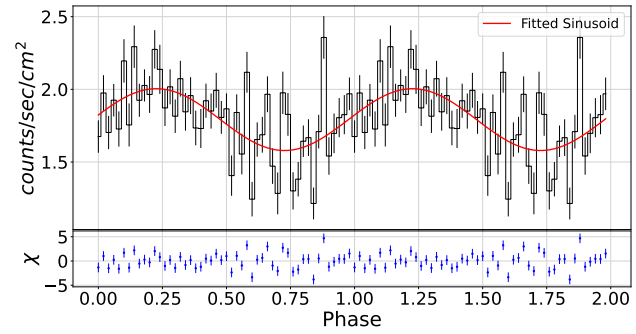

(c) Energy: 10-20 keV; χ^2_{red} = 2.92.

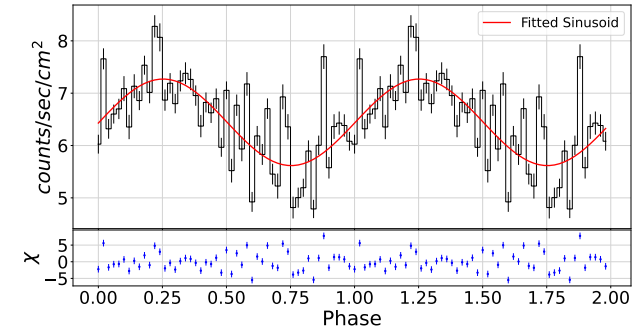

(d) Energy: 2-20 keV; χ^2_{red} = 8.73.

Figure 3.51: Phase folded lightcurve for Her X-1 at period ~2.35 days.

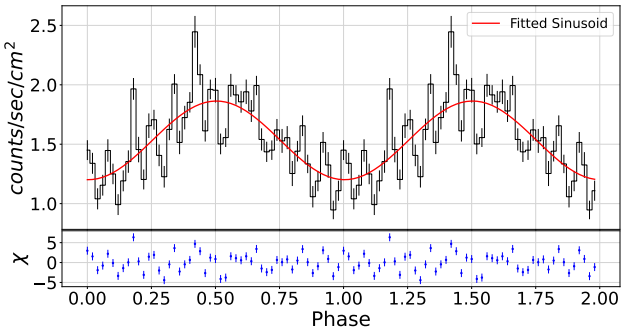

(a) Energy: 2-4 keV; χ^2_{red} = 5.94.

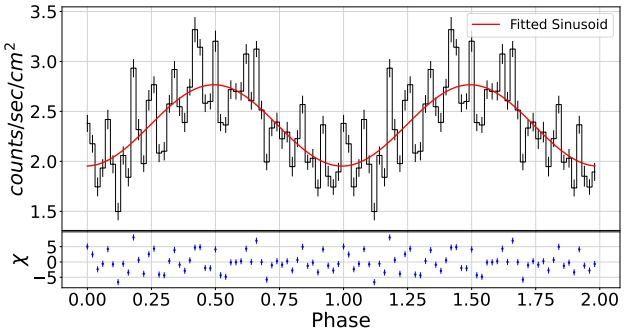

(b) Energy: 4-10 keV; χ^2_{red} = 12.01.

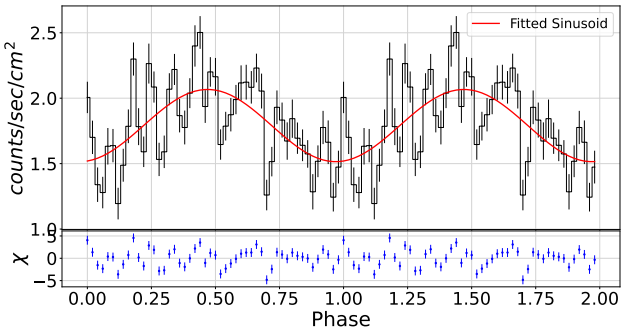

(c) Energy: 10-20 keV; χ^2_{red} = 4.38.

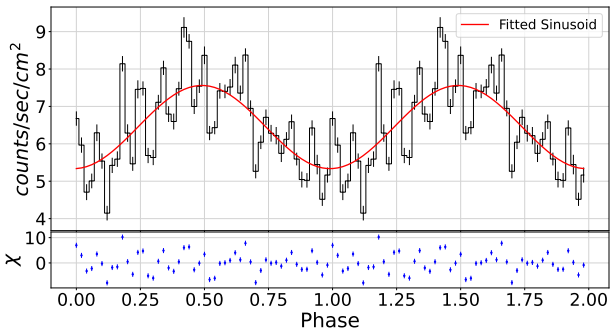

(d) Energy: 2-20 keV; χ^2_{red} = 17.56.

Figure 3.52: Phase folded lightcurve for Her X-1 at period ~2.43 days.

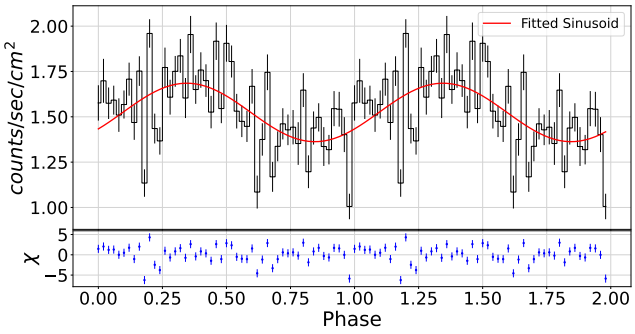

(a) Energy: 2-4 keV; χ^2_{red} = 5.04.

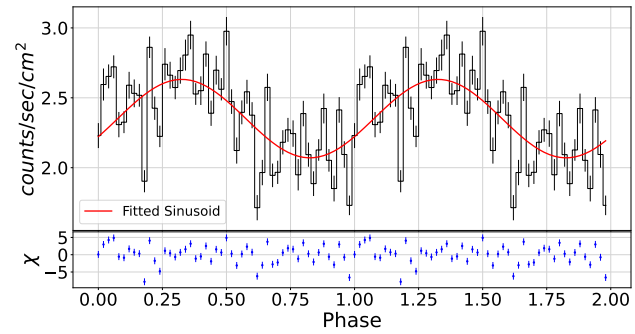

(b) Energy: 4-10 keV; χ^2_{red} = 8.48.

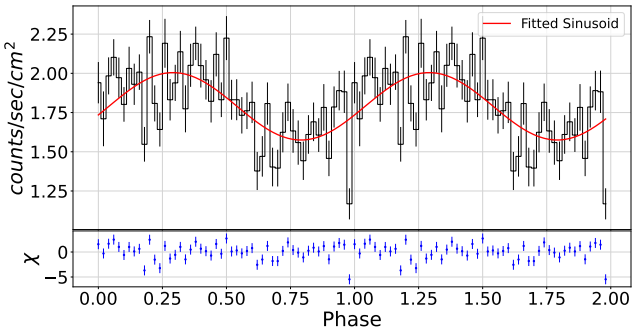

(c) Energy: 10-20 keV; χ^2_{red} = 2.81.

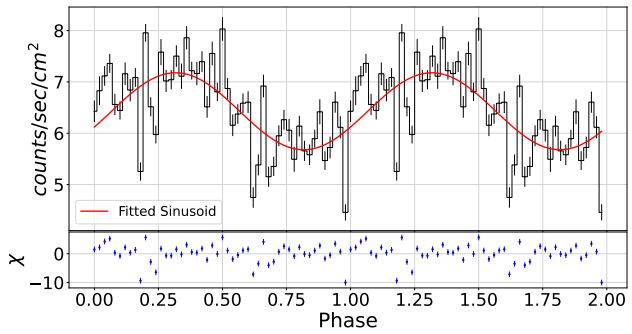

(d) Energy: 2-20 keV; χ^2_{red} = 11.64.

Figure 3.53: Phase folded lightcurve for Her X-1 at period ~2.51 days.

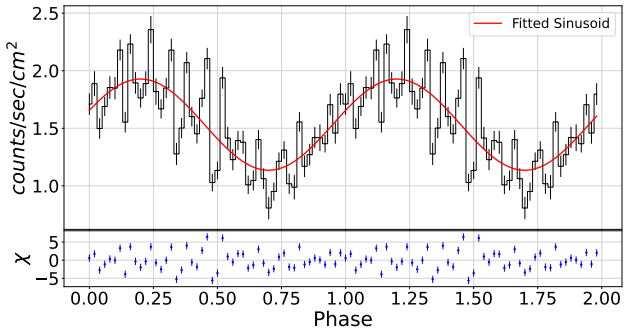

(a) Energy: 2-4 keV; χ^2_{red} = 7.55

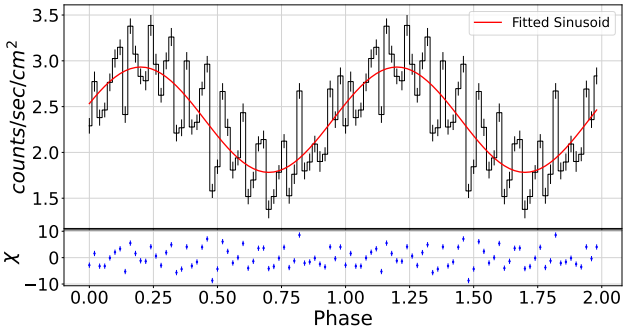

(b) Energy: 4-10 keV; χ^2_{red} = 15.22

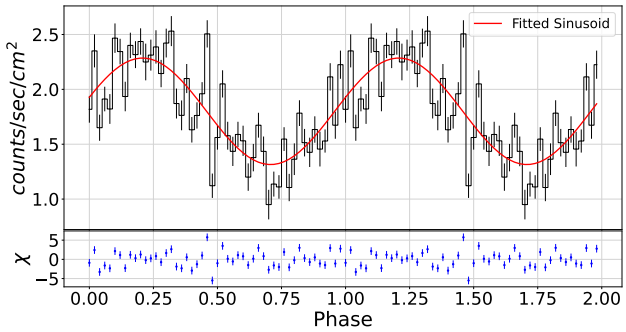

(c) Energy: 10-20 keV; χ^2_{red} = 4.55

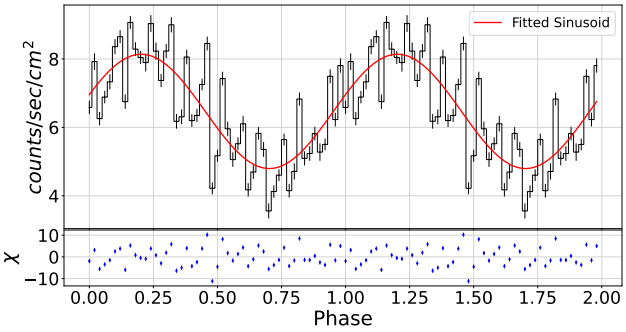

(d) Energy: 2-20 keV; χ^2_{red} = 20.56

Figure 3.54: Phase folded lightcurve for Her X-1 at period ~14.02 days.

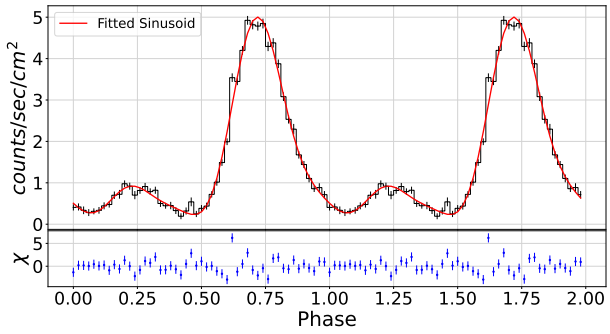

(a) Energy: 2-4 keV; χ^2_{red} = 2.88.

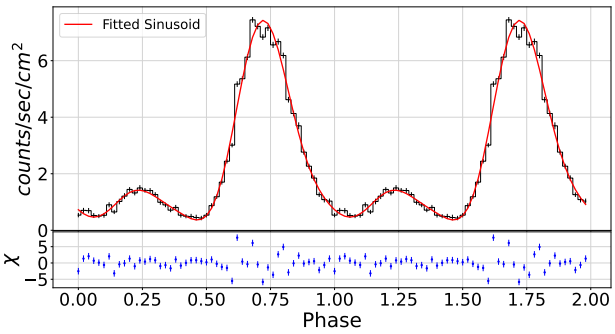

(b) Energy: 4-10 keV; χ^2_{red} = 6.72.

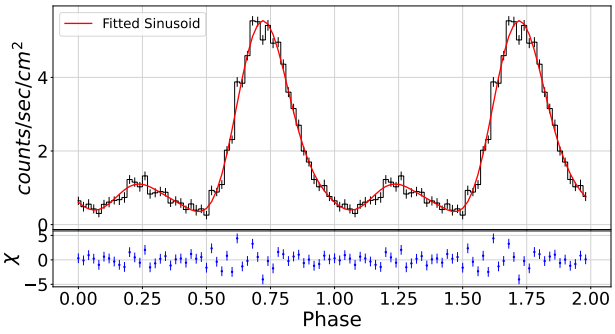

(c) Energy: 10-20 keV; χ^2_{red} = 2.46.

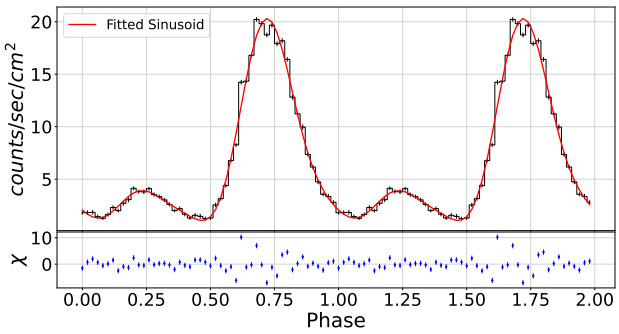

(d) Energy: 2-20 keV; χ^2_{red} = 9.00.

Figure 3.55: Phase folded lightcurve for Her X-1 at period ~34.74 days.

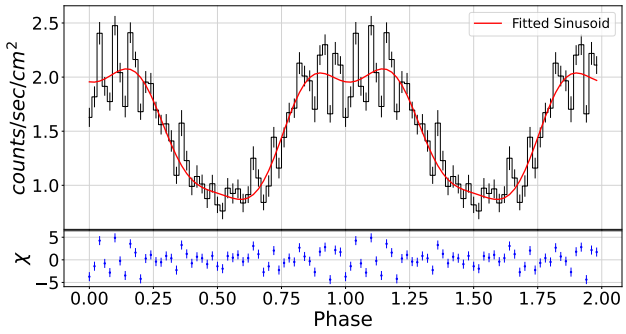

(a) Energy: 2-4 keV; χ^2_{red} = 5.25.

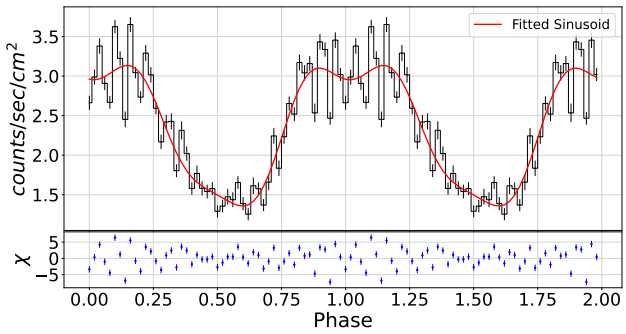

(b) Energy: 4-10 keV; χ^2_{red} = 10.41.

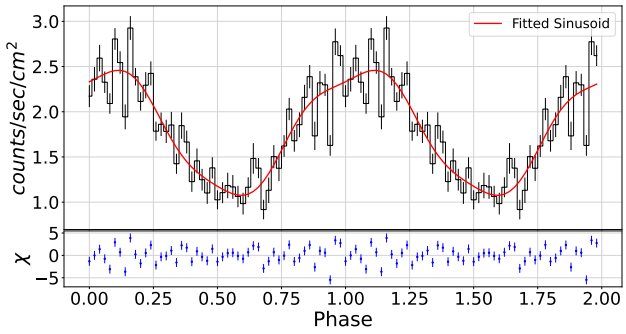

(c) Energy: 10-20 keV; χ^2_{red} = 4.13.

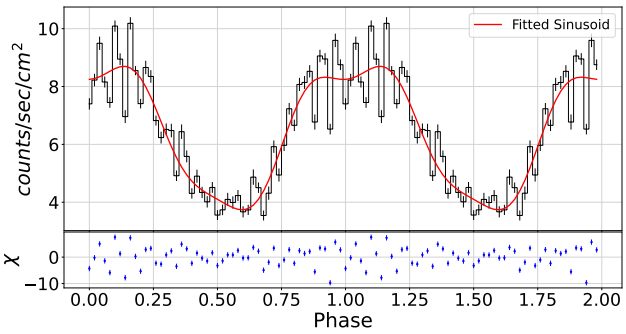

(d) Energy: 2-20 keV; χ^2_{red} = 15.80.

Figure 3.56: Phase folded lightcurve for Her X-1 at period ~66.54 days.

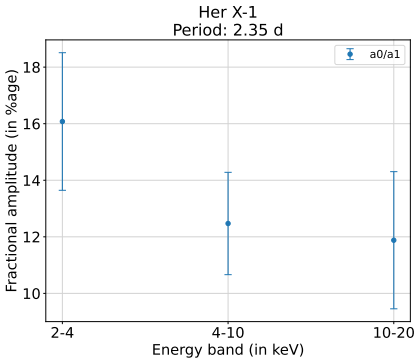

(a) Period: 2.35 days.

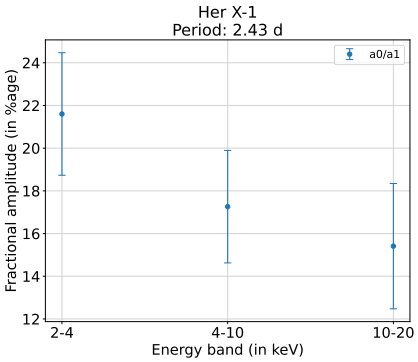

(b) Period: 2.43 days.

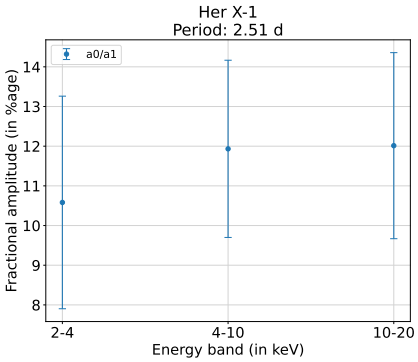

(c) Period:2.51 days.

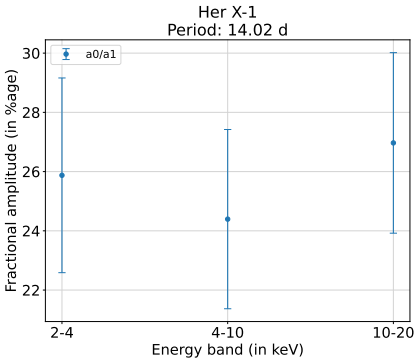

(d) Period: 14.02 days.

Figure 3.57: Fractional amplitude of the periods for the source Her X-1.

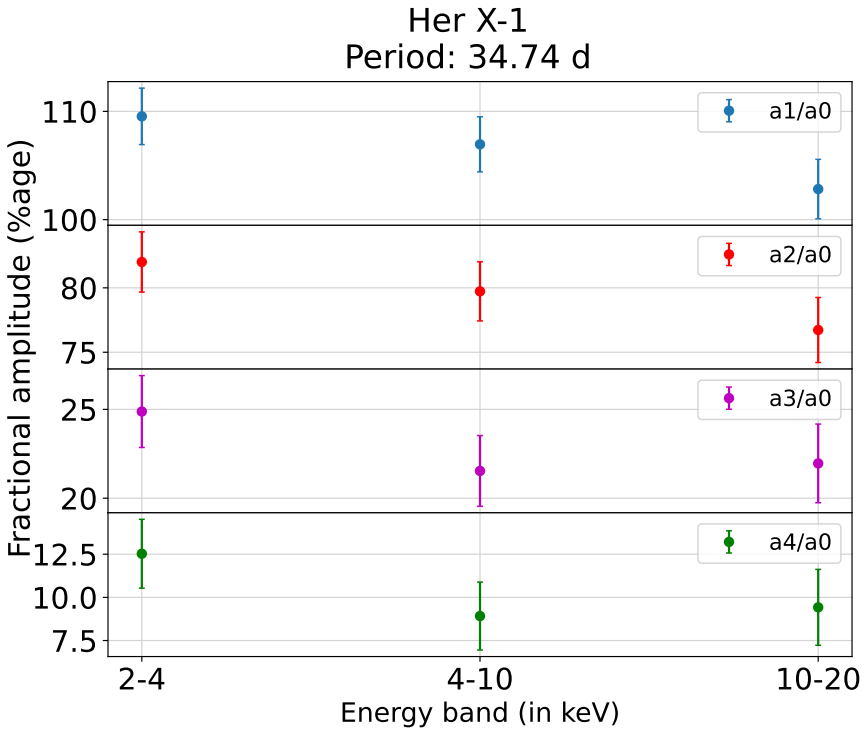

(a) Period:34.74 days.

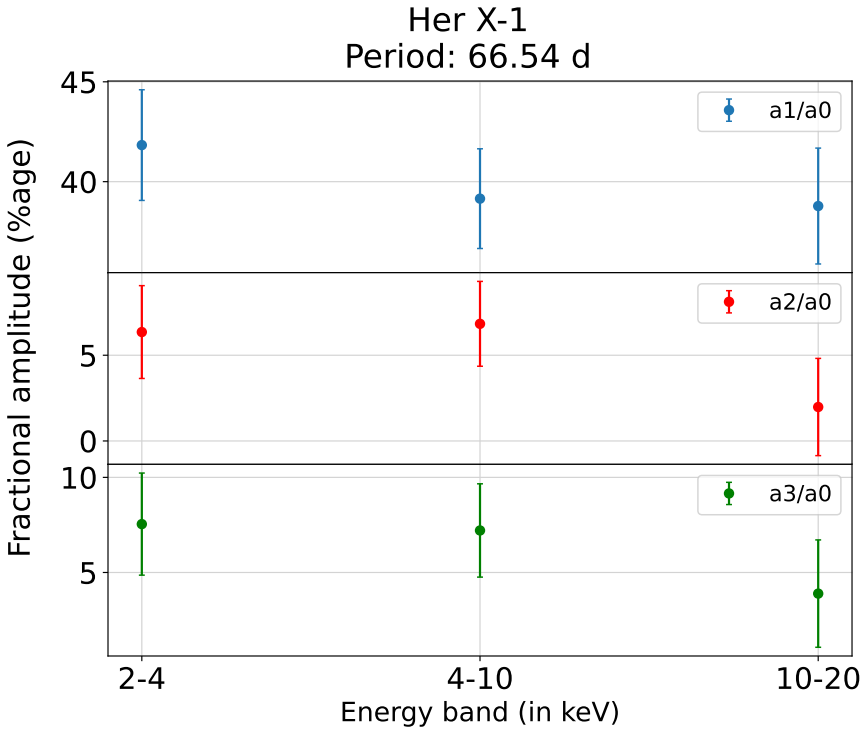

(b) Period: 66.54 days.

Figure 3.58: Fractional amplitude of the periods for the source Her X-1 for 34.75 and 66.54 days.

3.3.3 LMC X-4

The period of ~30.36 days and its harmonic 15.18 days show well periodic patterns when folded. Other than the two, ~51.64 days of period also gives a good repeating pattern. Fig. from 3.59 to 3.61 shows the folded lightcurves for the three periods. It can be seen from Fig. 3.61 that there is no variation in 2-4 keV energy band, showing low variability in this band, but the source is variable in other bands for 51.64 days of period.

Fig. 3.62 shows the variation in the fractional amplitude for the three periods. Period 15.18 days shows overlapping errors, hence one can infer that the physical region emitting photons in all three energy bands with some lower percent in the softer X-rays. The cause producing 30.36 days of period emits in the softer X-rays, whereas the mechanism producing 51.68 days of period emits in harder X-rays. Since 15.18 days is the harmonic of 30.36 days, both periods follow a similar trend in the fractional amplitude variation. The period 51.64 days has no relation to the two periods.

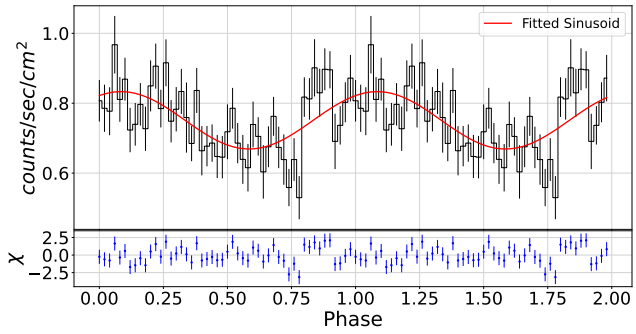

(a) Energy: 2-4 keV; χ^2_{red} = 1.57.

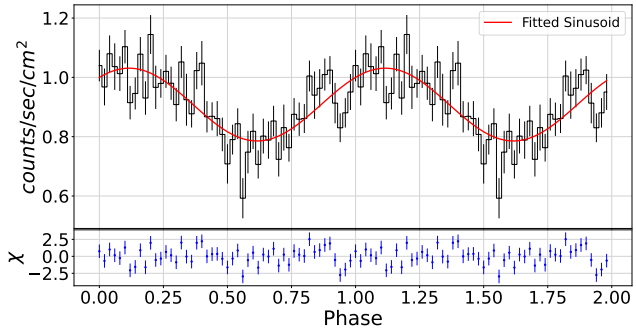

(b) Energy: 4-10 keV; χ^2_{red} = 1.71.

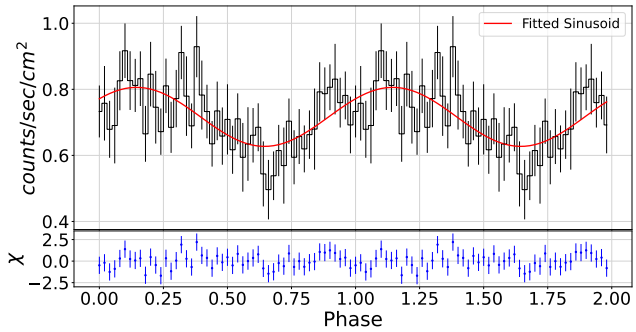

(c) Energy: 10-20 keV; χ^2_{red} = 0.78.

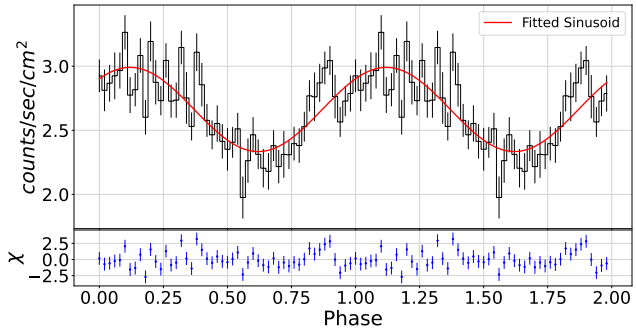

(d) Energy: 2-20 keV; χ^2_{red} = 1.84.

Figure 3.59: Phase folded lightcurve for LMC X-4 at period ~15.18 days.

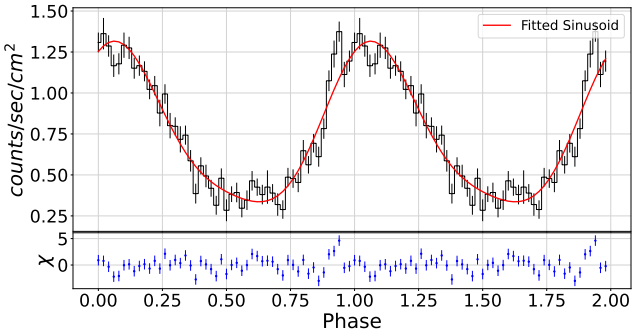

(a) Energy: 2-4 keV; χ^2_{red} = 1.81.

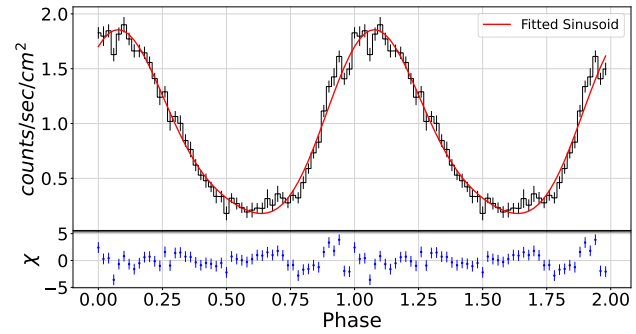

(b) Energy: 4-10 keV; χ^2_{red} = 1.82.

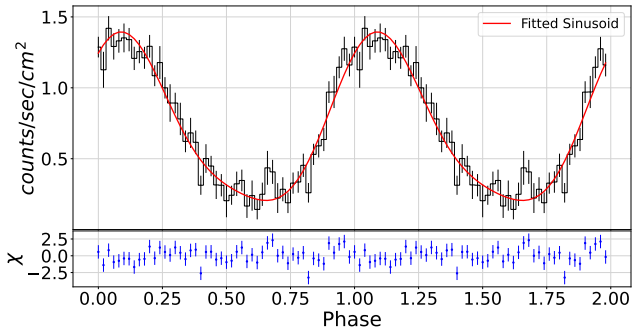

(c) Energy: 10-20 keV; χ^2_{red} = 1.14.

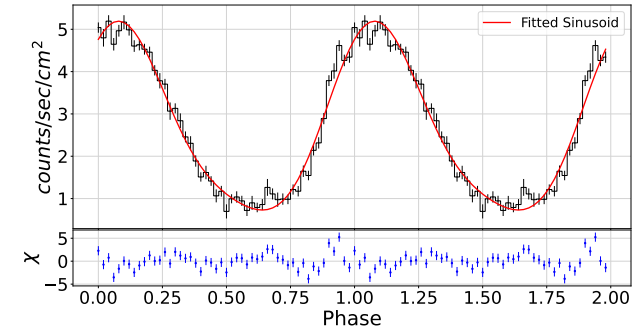

(d) Energy: 2-20 keV; χ^2_{red} = 2.11.

Figure 3.60: Phase folded lightcurve for LMC X-4 at period ~30.36 days.

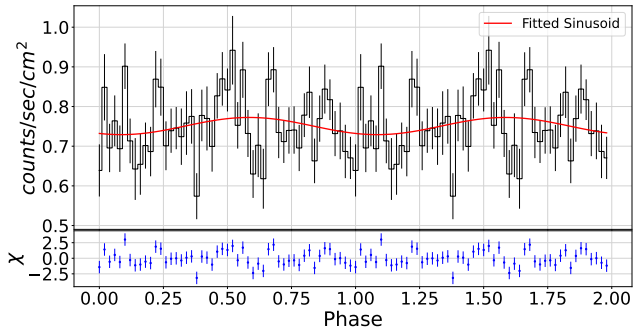

(a) Energy: 2-4 keV; χ^2_{red} = 1.06.

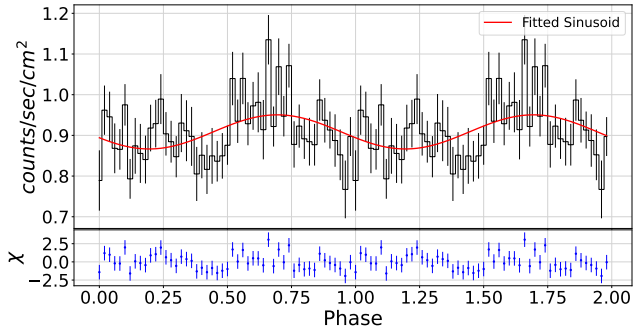

(b) Energy: 4-10 keV; χ^2_{red} = 1.34.

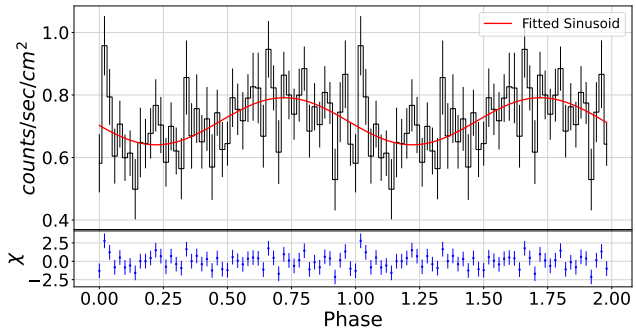

(c) Energy: 10-20 keV; χ^2_{red} = 1.66.

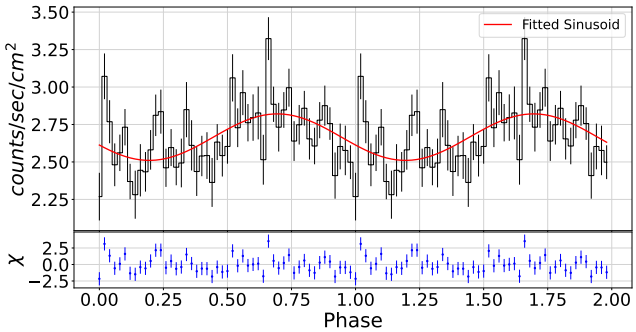

(d) Energy: 2-20 keV; χ^2_{red} = 1.69.

Figure 3.61: Phase folded lightcurve for LMC X-4 at period ~51.64 days.

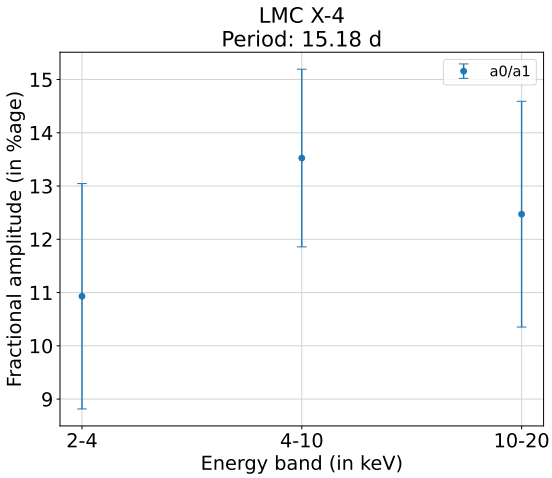

(a) Period: 15.18 days.

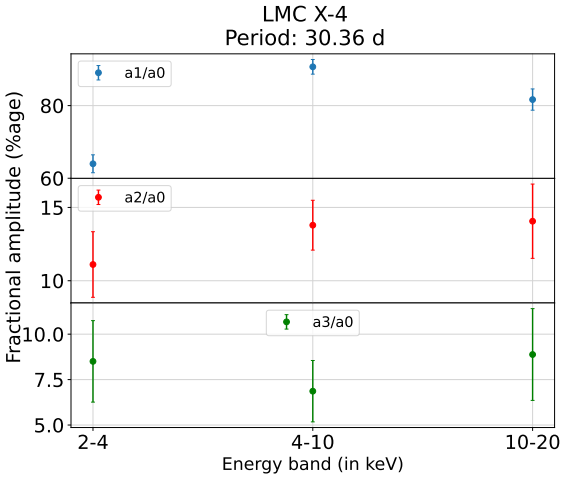

(b) Period: 30.36 days.

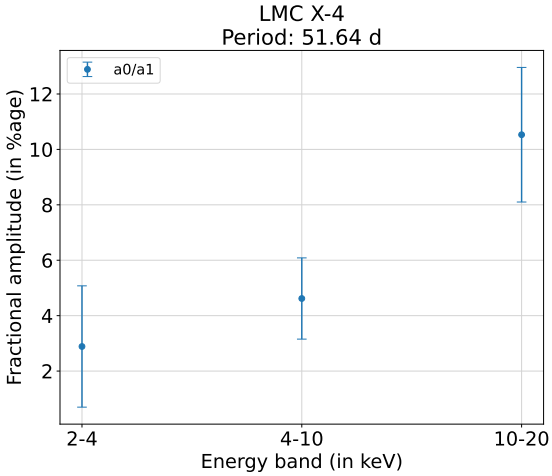

(c) Period: 51.64 days.

Figure 3.62: Fractional amplitude of the periods for the source LMC X-4.

3.3.4 SMC X-1

The phase folded lightcurve for all three detected periods are given from Fig. 3.63 to 3.65. The periods 2.06 and 3.89 days show the same pattern in all the energy bands in folded-lightcurve, which may be due to the fact that the former is a candidate instrument artifact and the latter is the orbital motion, hence may affect the photon in each energy equally. For 4.19 days of the period, the variation in 10-20 keV is lower than the other band, implying weakness of the signal in the band.

Fig 3.66 shows fractional amplitude for the three periods. Fractional amplitude does not show any modulation for 2.06 days, implying the complete spectrum is affected equally. The cause of the period can be the instrument artifact that was emerging in many sources, as discussed, which is affecting all the energies equally. Mechanism for period of 4.18 days is more dominantly emitting in the softer X-rays, corresponding to a low temperature region from the disk. The period of 3.89 days is the orbital period, and the amplitude $a3$ and $a4$ can have some correlation as they are following a similar trend.

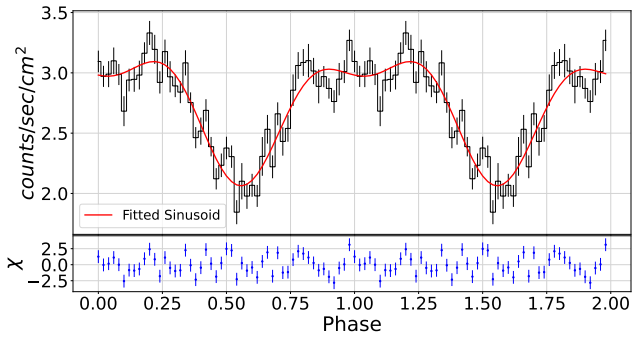

(a) Energy: 2-4 keV; χ^2_{red} = 2.48.

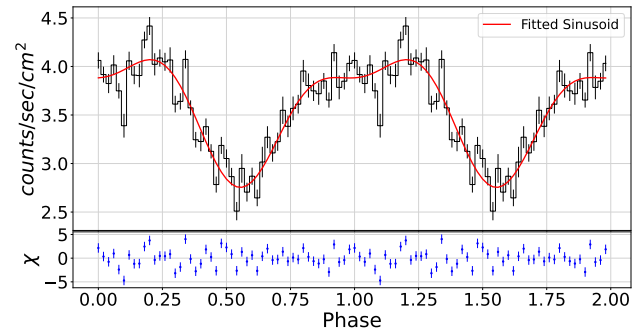

(b) Energy: 4-10 keV; χ^2_{red} = 3.88.

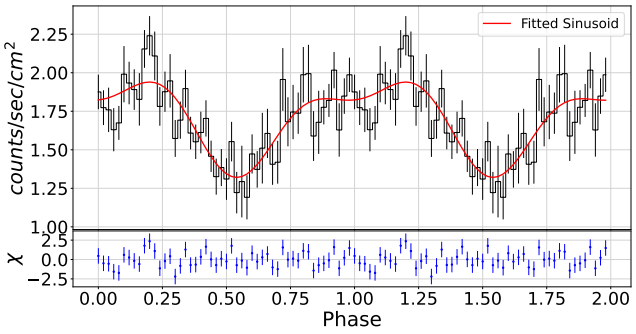

(c) Energy: 10-20 keV; χ^2_{red} = 1.16.

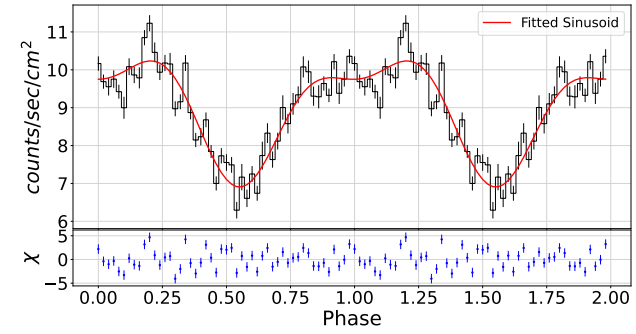

(d) Energy: 2-20 keV; χ^2_{red} = 4.63.

Figure 3.63: Phase folded lightcurve for SMC X-1 at period ~2.06 days.

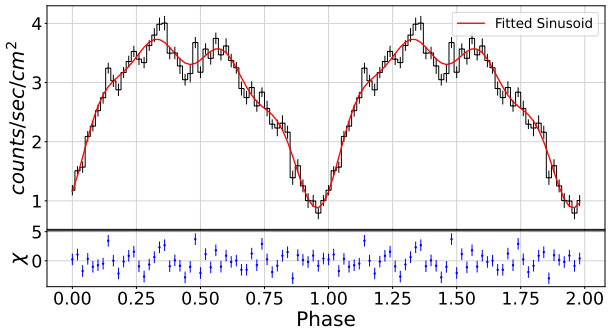

(a) Energy: 2-4 keV; χ^2_{red} = 2.89.

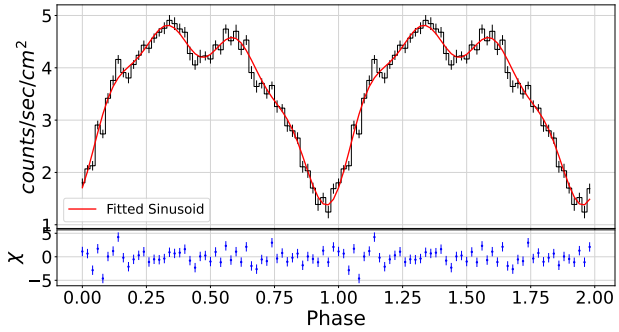

(b) Energy: 4-10 keV; χ^2_{red} = 3.02.

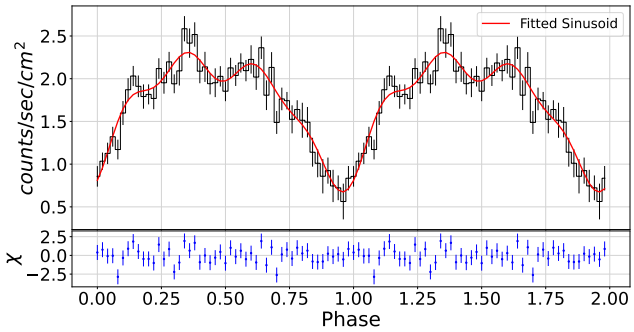

(c) Energy: 10-20 keV; χ^2_{red} = 1.35.

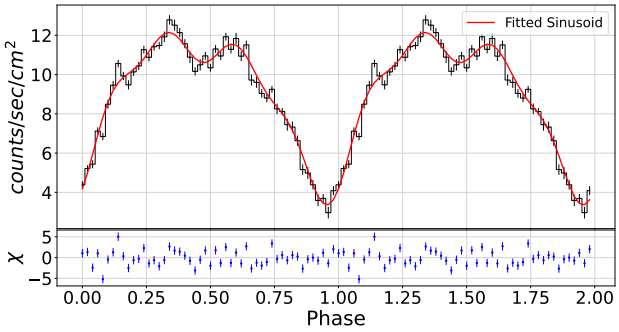

(d) Energy: 2-20 keV; χ^2_{red} = 4.32.

Figure 3.64: Phase folded lightcurve for SMC X-1 at period ~3.89 days.

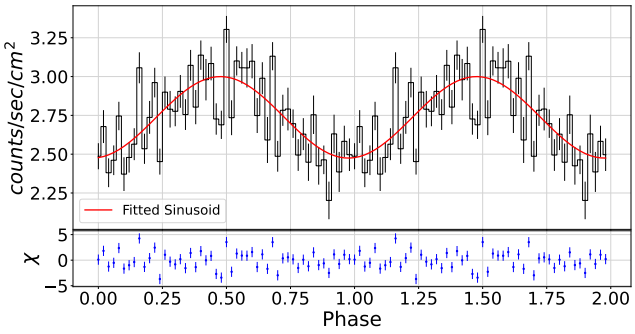

(a) Energy: 2-4 keV; χ^2_{red} = 3.24.

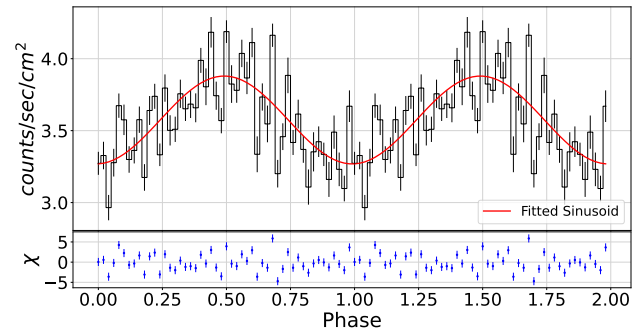

(b) Energy: 4-10 keV; χ^2_{red} = 5.32.

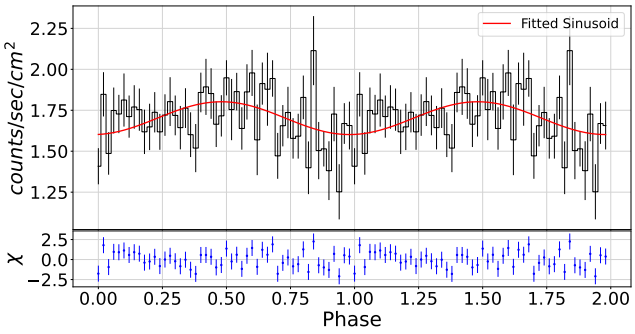

(c) Energy: 10-20 keV; χ^2_{red} = 1.17.

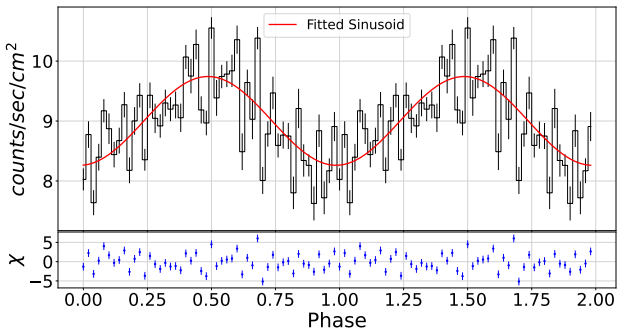

(d) Energy: 2-20 keV; χ^2_{red} = 5.73.

Figure 3.65: Phase folded lightcurve for SMC X-1 at period ~4.19 days.

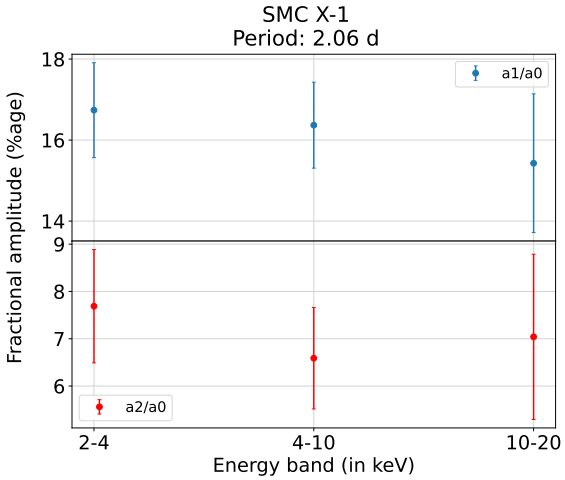

(a) Period: 2.06 days.

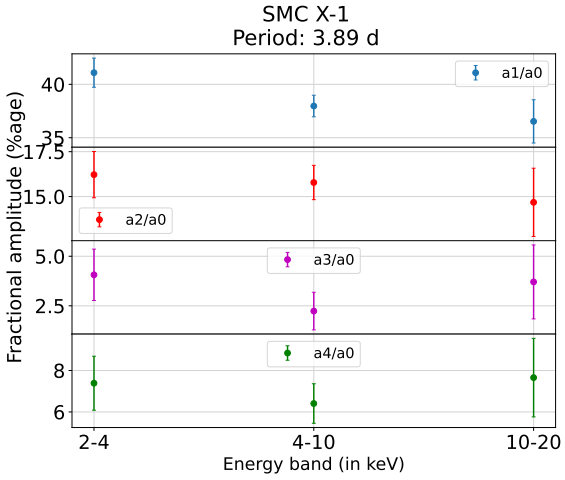

(b) Period: 3.89 days.

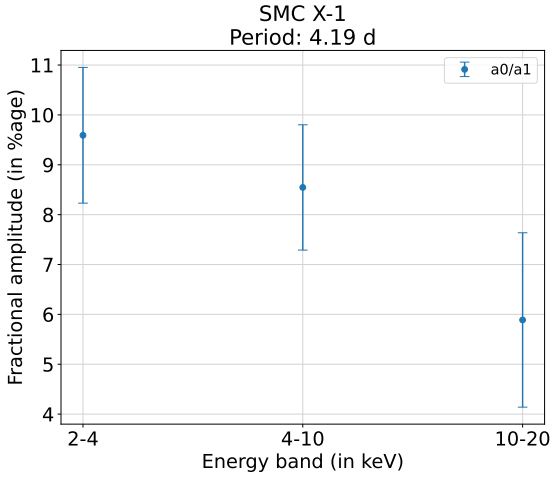

(c) Period: 4.19 days.

Figure 3.66: Fractional amplitude of the periods for the source SMC X-1.

3.3.5 SS433

Fig. 3.67 shows the variations in flux across different energy bands and Fig. 3.68 shows fractional amplitude for 162 days of period. The period is known to produced by the precession of relativistic jet from the source which are generally produced from the center of the system. The fractional amplitude for $a1$ also shows high variation in higher energy band, implying it is produced from higher temperature regions or from the inner parts of the disk.

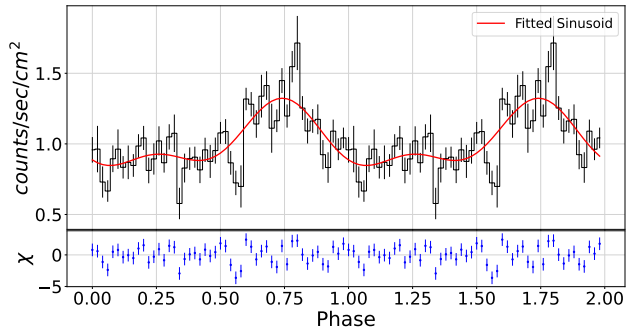

(a) Energy: 2-4 keV; χ^2_{red} = 2.19.

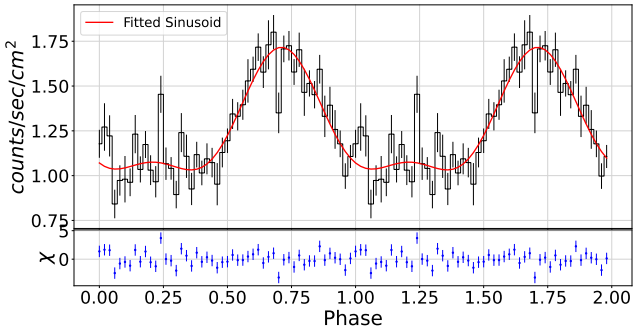

(b) Energy: 4-10 keV; χ^2_{red} = 1.74.

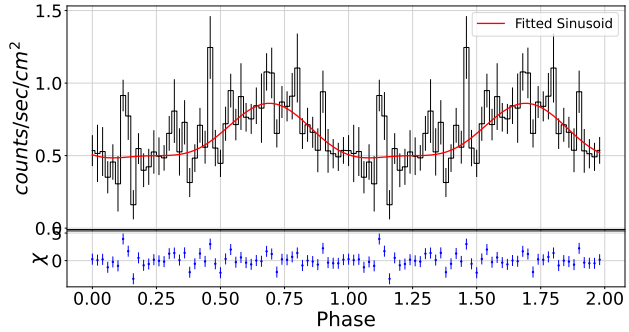

(c) Energy: 10-20 keV; χ^2_{red} = 1.82.

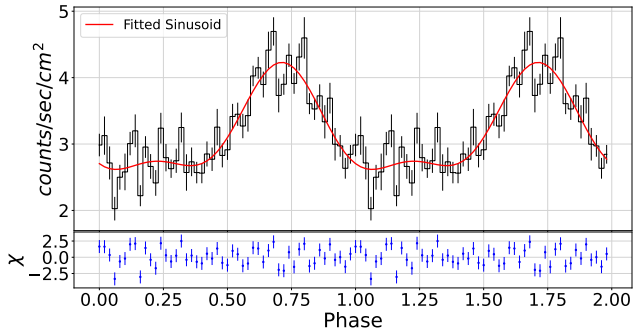

(d) Energy: 2-20 keV; χ^2_{red} = 2.20.

Figure 3.67: Phase folded lightcurve for SS433 at period ~162 days.

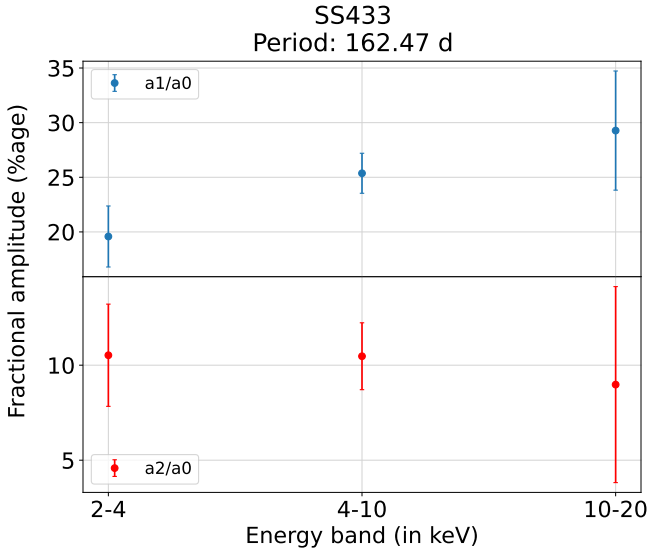

Figure 3.68: Fractional amplitude of SS433 for period 162 days in different energy bands.

3.3.6 X0114+650

Fig. 3.69 and 3.70 show the variation of flux in different energy bands in the phase-folded folded lightcurve. A significant variation in the flux pattern can be seen in different energy bands for both periods, 11.6 and 30.68 days. For 30.68 days of the period, the photons do not follow a periodic nature, showing low variability in the energy band 10-20 keV.

From Fig. 3.71 it can be seen that the variation in the flux decreases with energy due to the orbital motion as 11.6 days is the orbital period. The period of 30.68 days is produced due to precession of the disk and may be produced due to low temperature regions.

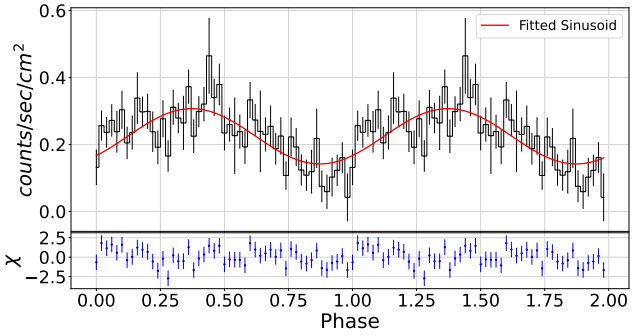

(a) Energy: 2-4 keV; χ^2_{red} = 1.20.

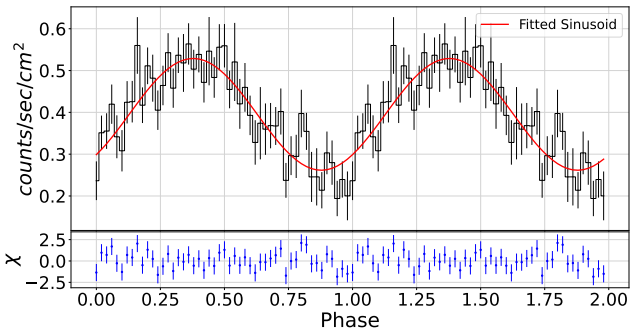

(b) Energy: 4-10 keV; χ^2_{red} = 1.07.

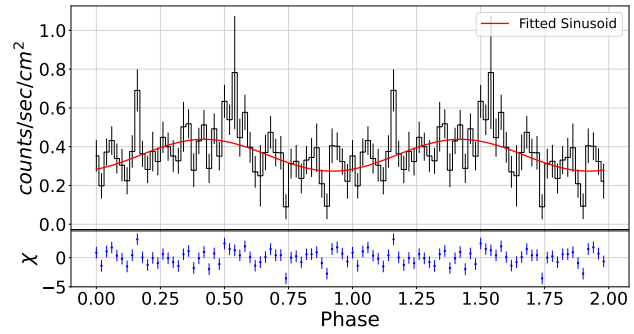

(c) Energy: 10-20 keV; χ^2_{red} = 1.79.

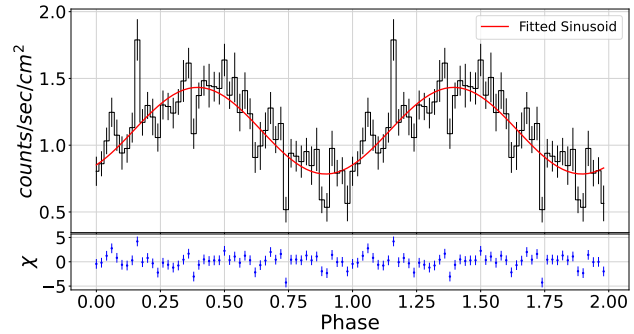

(d) Energy: 2-20 keV; χ^2_{red} = 2.26.

Figure 3.69: Phase folded lightcurve for X0114+650 at period ~11.6 days.

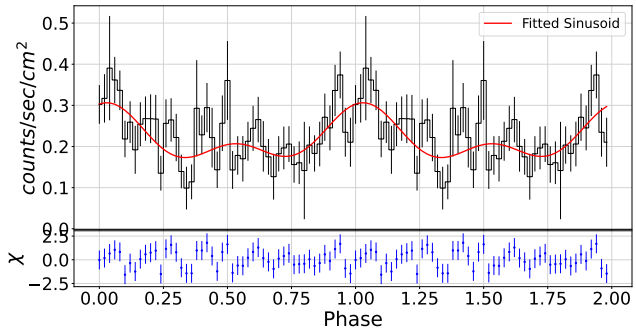

(a) Energy: 2-4 keV; χ^2_{red} = 1.00.

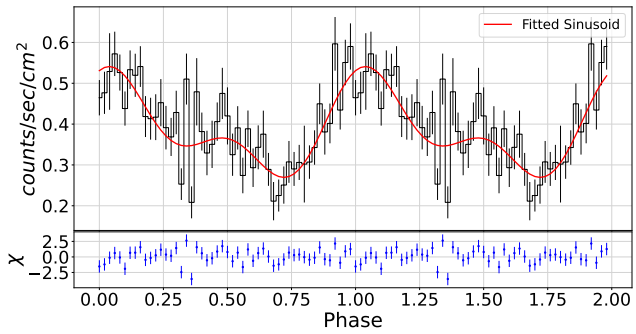

(b) Energy: 4-10 keV; χ^2_{red} = 1.57.

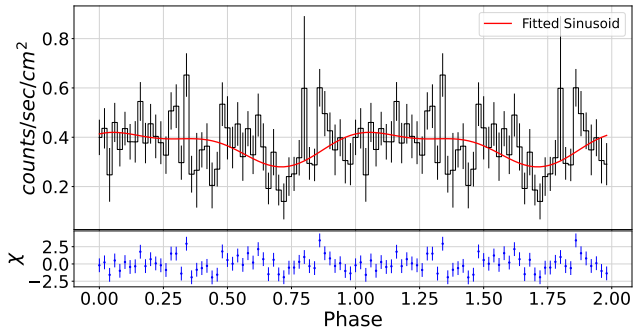

(c) Energy: 10-20 keV; χ^2_{red} = 1.68.

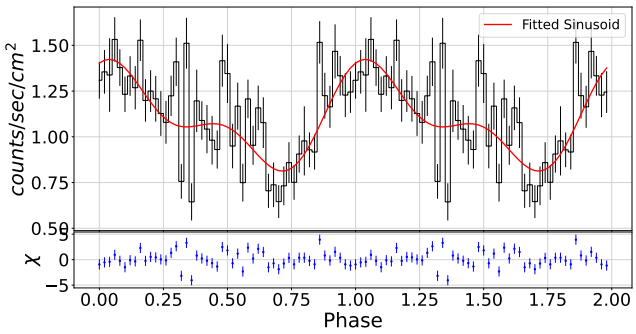

(d) Energy: 2-20 keV; χ^2_{red} =2.62.

Figure 3.70: Phase folded lightcurve for X0114+650 at period ~30.68 days.

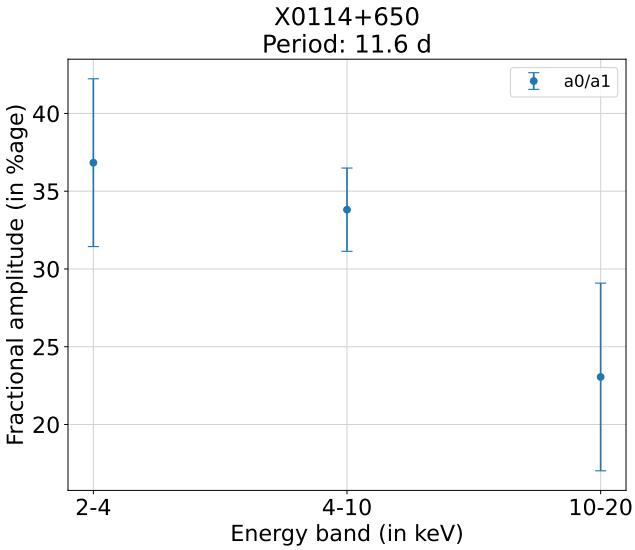

(a) Period: 11.6 days.

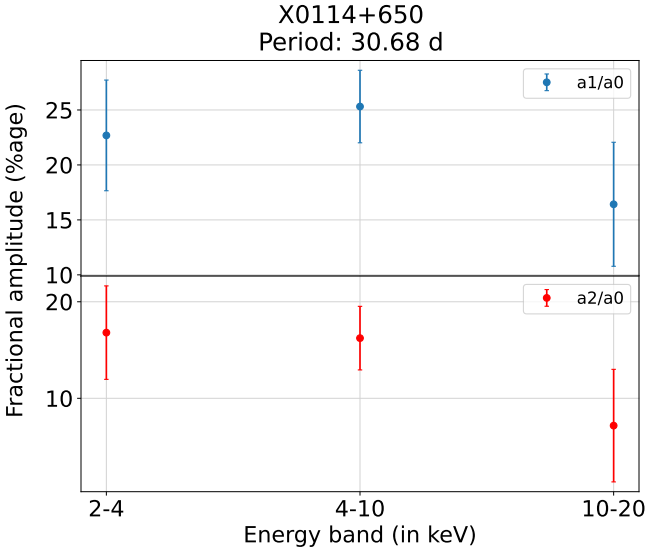

(b) Period: 30.68 days.

Figure 3.71: Fractional amplitude of the periods for the source X0114+650.

3.3.7 X1907+097

Fig. 3.72 shows the variations in the periods of 8.37 days. From the figure, it can be seen that in energy band 2-4 keV, the signal does not follow a pattern, whereas well well-periodic nature can be seen in other bands. Phase folded lightcurve for period 71.75 days is shown in Fig. 3.73.

Fig. 3.74 shows the effect of orbital motion (8.37 day) on the flux variation. High variability is seen in higher energy bands due to this. An interesting feature can be seen for the period 71.75 days that the fractional amplitude first decreases, then increases and again decreases for $a1$ and the reverse happens for $a2$, whereas $a3$ shows a monotonic decrease with increase in energy.

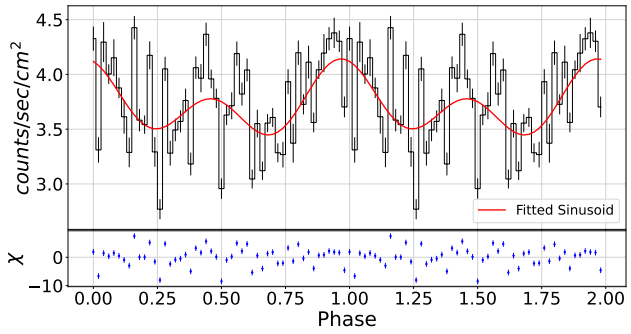

(a) Energy: 2-4 keV; χ^2_{red} = 12.99.

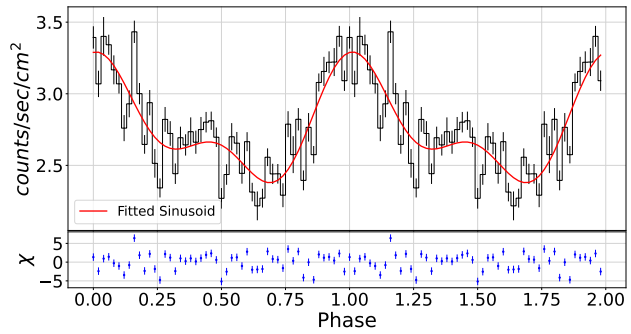

(b) Energy: 4-10 keV; χ^2_{red} = 6.14.

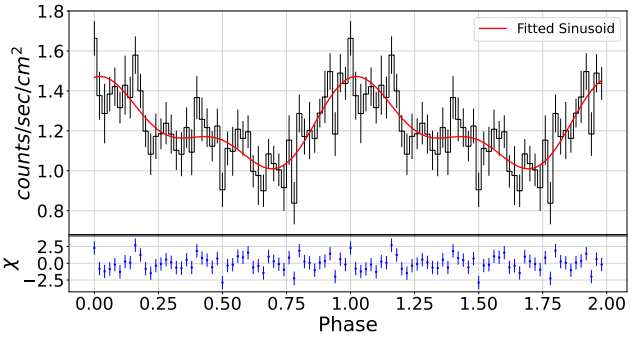

(c) Energy: 10-20 keV; χ^2_{red} = 1.40.

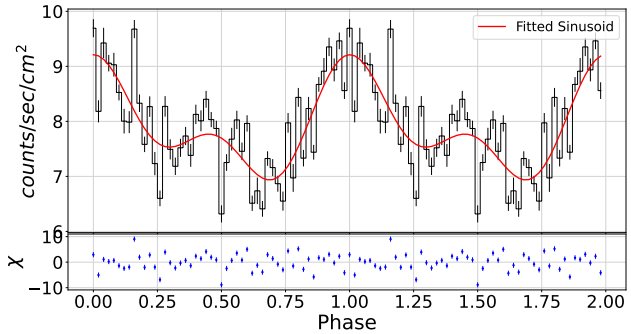

(d) Energy: 2-20 keV; χ^2_{red} = 12.32.

Figure 3.72: Phase folded lightcurve for X1907+079 at period ~8.37 days.

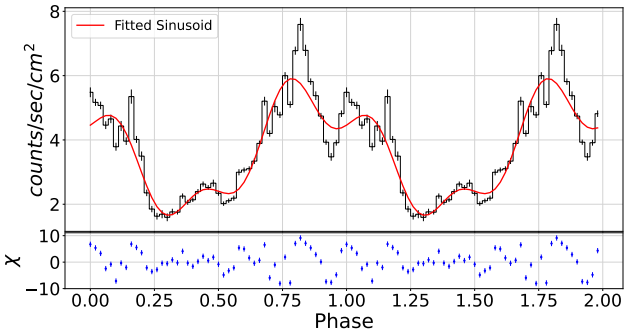

(a) Energy: 2-4 keV; χ^2_{red} = 22.61.

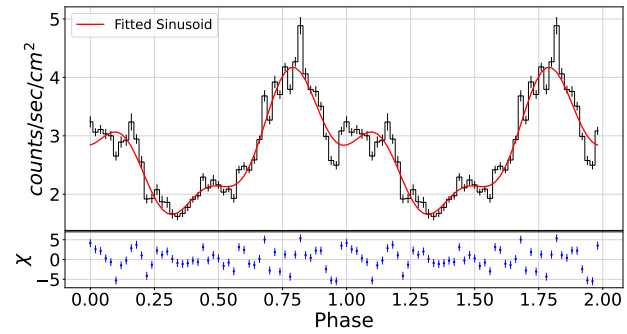

(b) Energy: 4-10 keV; χ^2_{red} = 7.93.

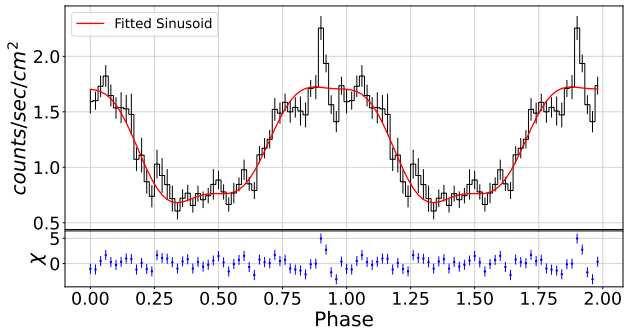

(c) Energy: 10-20 keV; χ^2_{red} = 2.15.

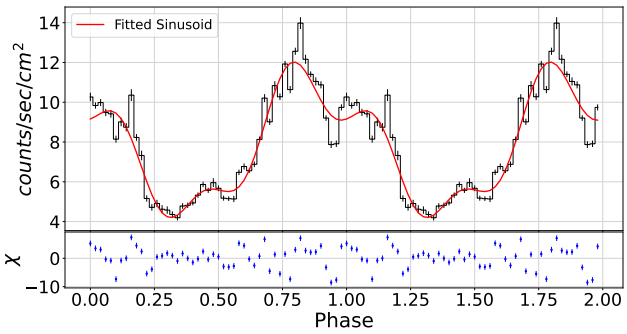

(d) Energy: 2-20 keV; χ^2_{red} = 17.15.

Figure 3.73: Phase folded lightcurve for X1907+097 at period ~71.75 days.

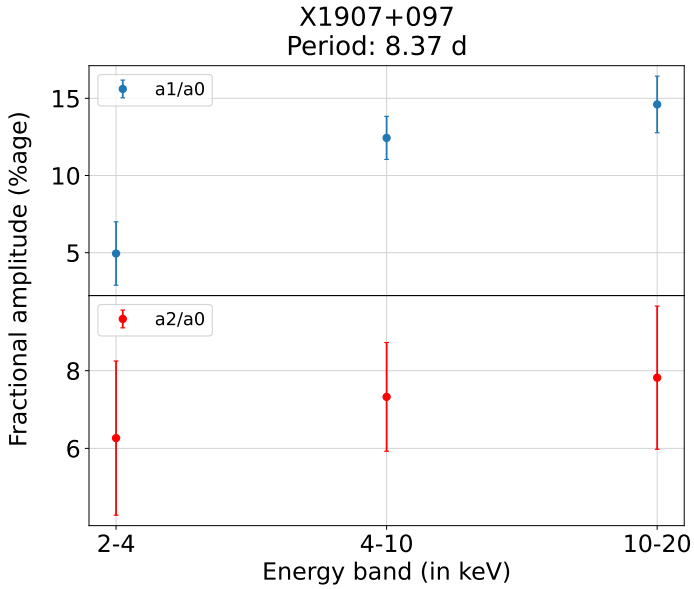

(a) Period: 8.37 days.

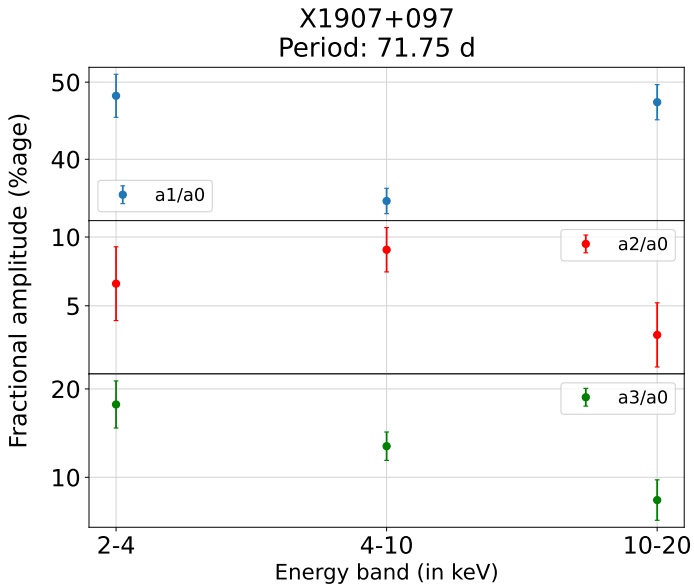

(b) Period: 71.75 days.

Figure 3.74: Fractional amplitude of the periods for the source X1907+097.

3.4 Results from Scanning-Sky Monitor/AstroSat

The very first choice of instrument that we had for our study was the Scanning-Sky Monitor (SSM) on board AstroSat. With the help of SSM data, we plotted the light curves for the X-ray source Sco X-1 and tried to find the periodicities present. Fig. 3.75 shows the lightcurve of Sco X-1 for 1 satellite orbit.

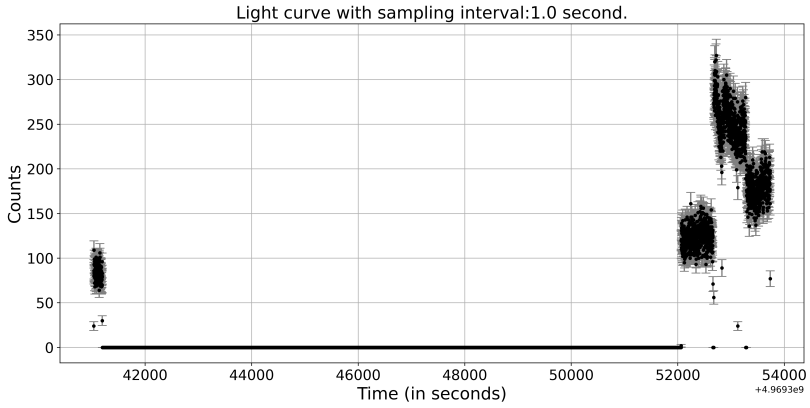

Figure 3.75: Sco X-1 light curve from SSM data for orbit ID 03294, binned at 1 second. The x-axis is in units of +4.9693e9 seconds.

Due to large data gaps in the light curve, we were unable to construct the periodogram. The large gaps acted as the windows whose periodogram comes out as a sinc function, which should not be the case. So, data with large gaps cannot be used to detect the superorbital periodicities, as the gaps contain the information about the intensity, which is missing in this case. But, the data can be used to study the variations in the pulsation period, as pulses have the periodicity of seconds and milliseconds, and hence can be detected in even small data sets. So, we will be using the SSM data to look for pulse evolution.

Hence, to find superorbital periodicities, we used the lighcurves from MAXI where we found different periodicities for different sources as discussed above.

We tried finding the pulsation in the lightcurves of three sources, namely, Cen X-3, GRO J2058+42 and Her X-1, using SSM. As we have seen earlier

that to find the small periodicities, the binning of the lightcurve is one of the most important things that has to be kept in mind. Hence, to find pulsations which are periodicities in the range of some milliseconds to some seconds, the binning should be of the same order or even smaller. We used different kinds of binning for different sources. We had some FITS files (FITS is a file format) from the satellite for the above three sources. Each of these files contains a different number of extensions, each with $\sim$ 10 $minutes$ of observation. As discussed earlier for the cases of long-term periodicities that the data contains lots of gaps when all the extensions are combined to form a single lightcurve. The large gaps, on transforming from time to frequency domain, give a sinc function which is not suitable for detecting the periodicities. To deal with this, instead of combining all the extensions, we studied single extensions at once. Since the 10 minute extensions do not have any data gap, the problem of the sinc nature in the periodogram will be solved. Also, as we are looking for pulsation, 10 minutes of data is good enough to detect the spin periods (if present). The study and analysis of the three sources are as follows:

3.4.1 Cen X-3

This is a neutron star binary star system with the spin period of ~4.8 seconds (Giacconi et al. 1971) and orbital period of ~2.09 days, which we detected from the MAXI observations. To find the period of 4.8 seconds (or spin frequency, $f_{spin} = 0.2083Hz$), the binning should be such that the sampling frequency (f_{samp}) of the lightcurve is double of the maximum frequency (f_{spin}) to be detected or more than that. Here, the $f_{spin} = 0.2803\ Hz$, hence $f_{samp} > 2f_{spin}$, i.e, $f_{samp} > 0.4166\,Hz$. In other words, the binning or the sampling time ($t_{samp} = f_{samp}^{-1}$) should be smaller than 2.4 seconds. The binning of 1-second is used to just look for the behavior of the lightcurves and to check for the anomalies, if present in the lightcurves. The following figure shows the 10 minute lightcurves for the source for the different extensions:

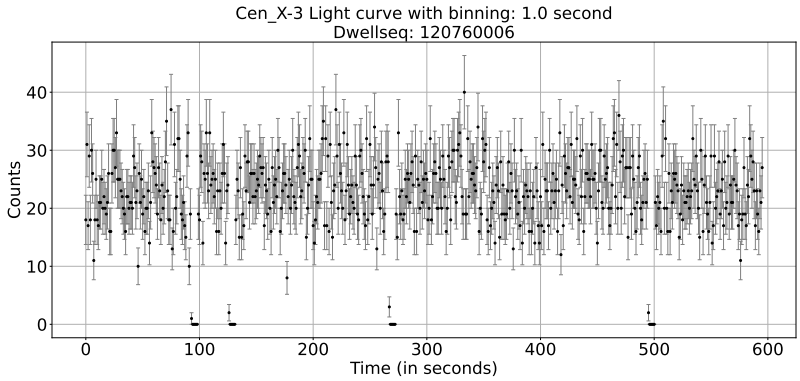

Figure 3.76: Cen X-3: 1-sec binned lightcurve for dwell sequence 120760006.

Fig. 3.76 is a lightcurve from one of the extensions from the FITS file which has a photon count rate of up to 40 counts/sec. Other than this, the instrument gives some peculiar lightcurves due to different reasons. For example, in Fig. 3.77 there is a sudden increase and decrease of the photon counts rate which can be due to the dwelling of SSM such that the source just comes into the sight of it and moves out quickly as it dwells.

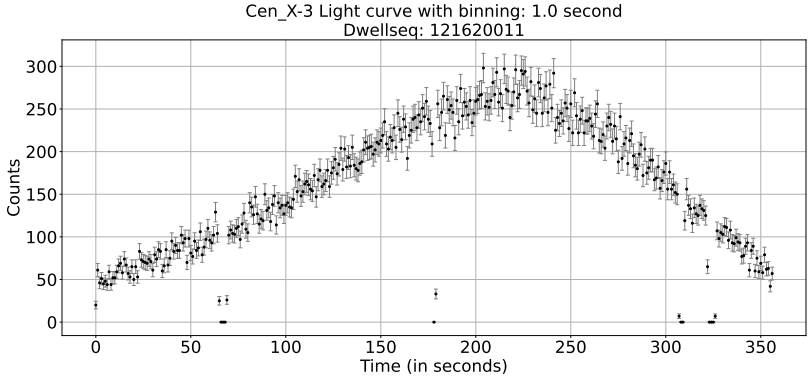

Figure 3.77: Cen X-3: 1-sec binned lightcurve for dwell sequence 121620011.

Another anomaly that can be seen in the lightcurves is the rise in the photon counts throughout the extension. Fig. 3.78 shows an example of such behavior. The reason for this can be the appearance of other sources with high flux in these extensions while observing Cen X-1.

In order to look for pulsation, it is not a good idea to search for it in all the extensions as some of them show anomalies and we can lose information

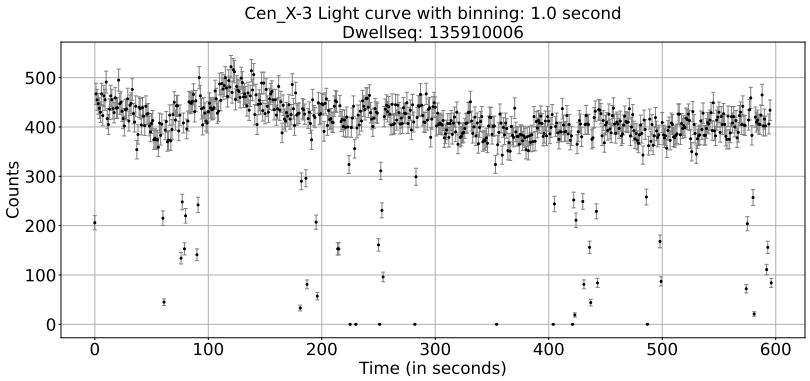

Figure 3.78: Cen X-3: 1-sec binned lightcurve for dwell sequence 135910006.

about the source. So, we can study the lightcurves which have a photon count rate around ~10 to 40 counts/sec, like in Fig. 3.76.

From the lightcurves of the type discussed above, periodograms are constructed using the *scipy.signal.periodogram* module in Python. Here, the Fourier transformation can be used instead of Lomb-Scargle as the data is evenly spaced. The application of the Lomb-Scargle periodogram primarily affects the scaling of the power spectrum but does not modify the underlying periodic structure. From the periodogram, the maximum power peak and the corresponding period are extracted. Then the phase-folded folded lightcurve is created at the detected periods to look for how the flux changes throughout the period.

The periodograms for different lightcurves from different extensions show different periods. Fig. 3.79 shows two different periodograms from two different lightcurves and Fig. 3.80 shows the corresponding phase-folded lightcurves at the periods where maximum power is detected.

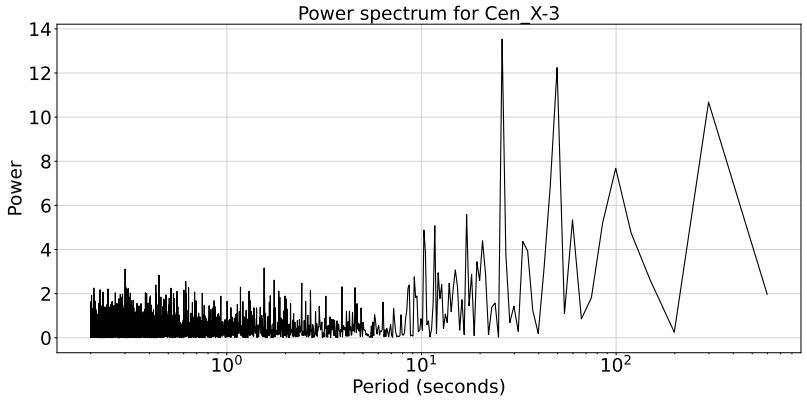

(a) Periodogram 1: maximum power at 25.952 sec.

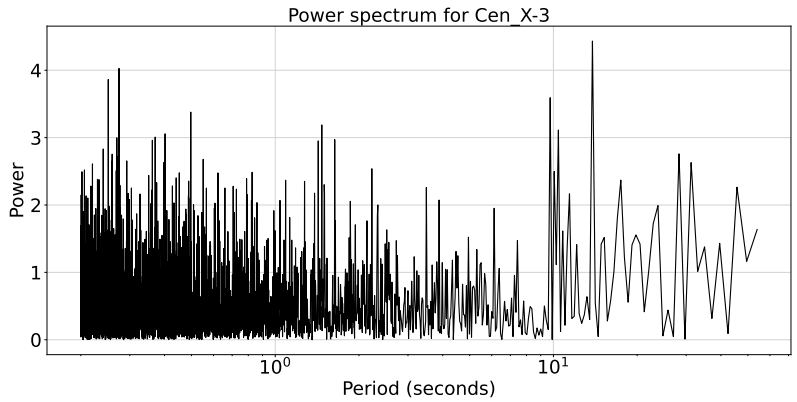

(b) Periodogram 2: maximum power at 13.812 sec.

Figure 3.79: Periodograms for two different light curves of Cen X-3.

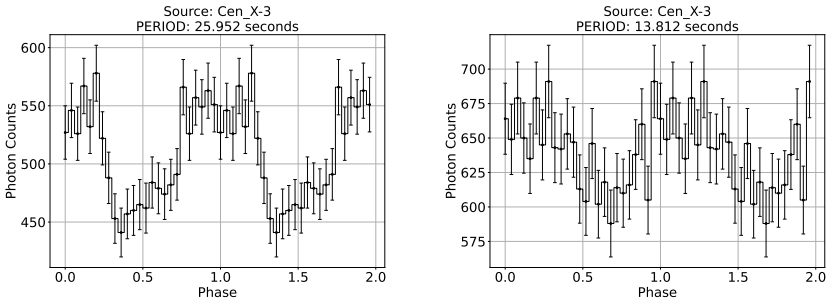

(a) For Fig. 3.85a at period 25.952s. (b) For Fig. 3.85b at period 13.812s.

Figure 3.80: Phase folded lightcurve at the periods corresponding to the highest peak for the periodograms plotted in Fig 3.79.

The periodograms does not show any strong periods, individually. Similarly, many well periodic phase-folded lightcurves were detected at many different periods. The periods may not be the intrinsic property of the

source. The averaged periodogram calculated from the lightcurves similar to Fig. 3.76, shows a peak at period ~4.799 seconds as shown in the Fig. 3.81. The higher periods in the periodogram are not shown as they contain lots of noise. The main reason to note this period is that it is close to the spin period of the source. Further proofs are needed to confirm that this period arise due to the spin of the neutron star.

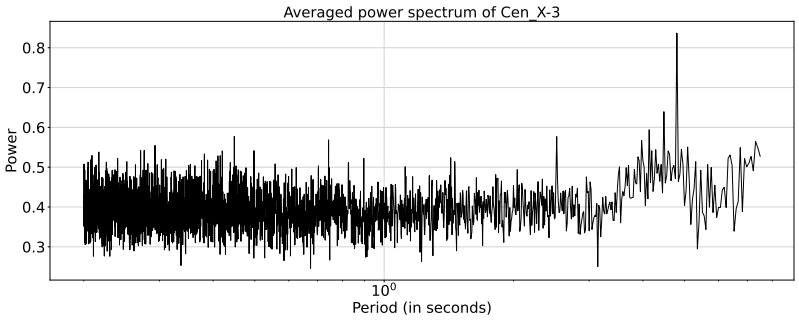

Figure 3.81: Averaged power spectrum of Cen X-3.

The higher periods in the periodogram are not shown as they contain lots of noise. The main reason to note this period is that it is close to the spin period of the source. Further proofs are needed to confirm that this period arise due to the spin of the neutron star.

3.4.2 GRO J2058+42

This is a Be binary system, where the companion is a Be star. These are the stars with spectral type B but have a strong hydrogen emission line in their spectrum due to a circumstellar disk present around them. This X-ray binary source has a pulsation period of $\sim$ 194 *seconds* (Mukerjee, Antia, and Katoch 2020).

The source also contains some anomalies and peculiarities in its lightcurves (not as high as seen in Cen X-3). The source shows a variable nature in lightcurves for some extensions, as shown in Fig. 3.82

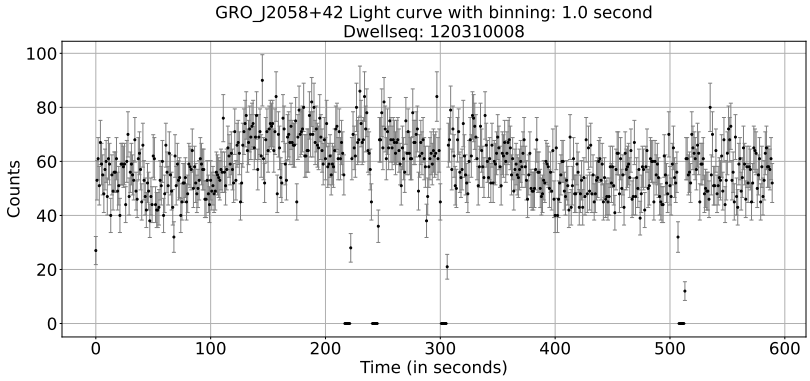

Figure 3.82: GRO J2058+42: 1-sec binned lightcurve for dwell sequence 120310008.

Apart from these variable lightcurves, we have some lightcurves which do not show this kind of nature. These lightcurves can be used to reach our science goal, like in Fig. 3.83.

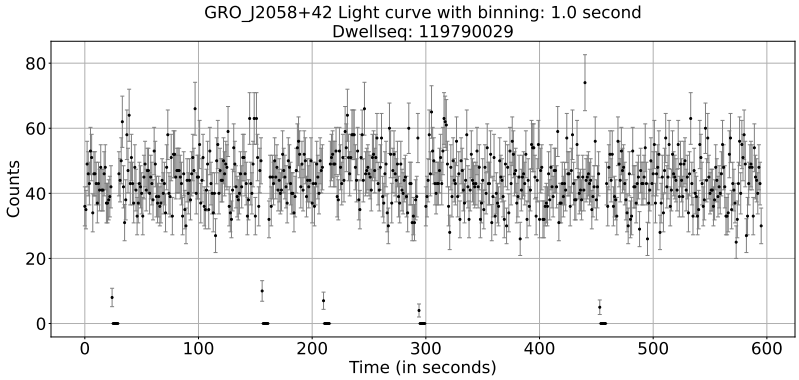

Figure 3.83: GRO J2058+42: 1-sec binned lightcurve for dwell sequence 119790029.

Similar to Cen X-3, unusual features have been seen in the periodograms, that lightcurves from different extensions show different periods for the same source. Also, instead of the source's spin period, we detected some periods that do not belong to the source. Fig 3.84a and 3.84b show two different periodograms for the source with different nature and Fig 3.85 shows the phase-folded lightcurves of the sources at the periods corresponding to the highest peak in the periodograms.

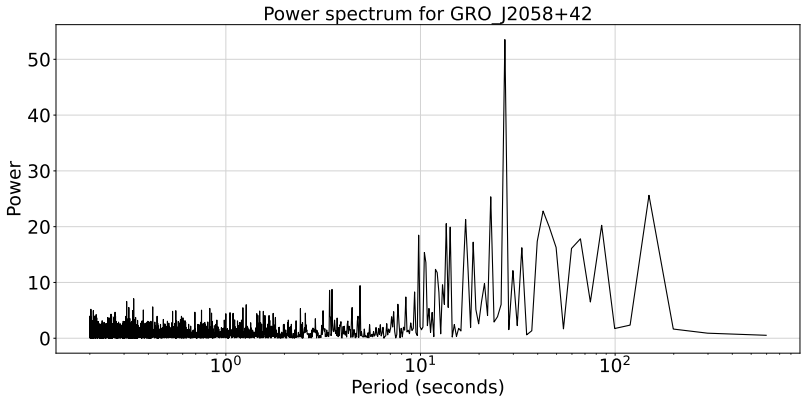

(a) Periodogram 1: maximum power at 27.132 sec.

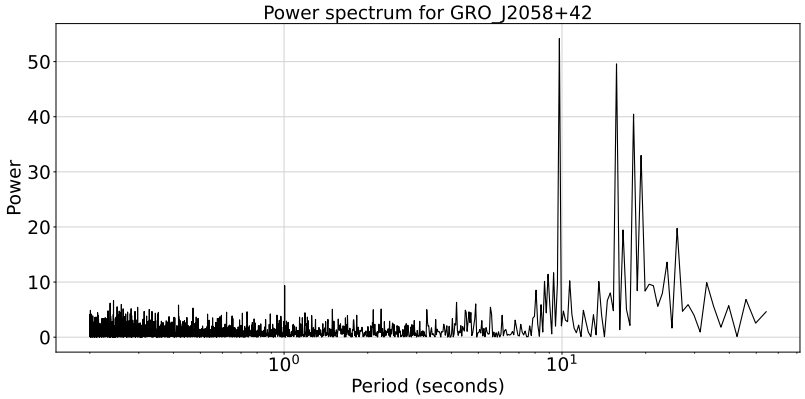

(b) Periodogram 2: maximum power at 9.785 sec.

Figure 3.84: Periodograms for two different light curves of GRO J2048+52.

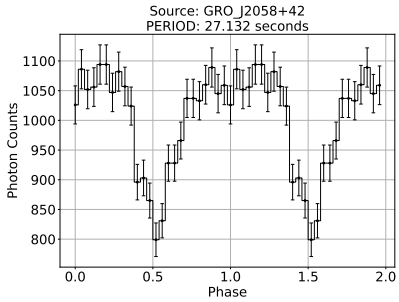

(a) For Fig. 3.85a at period 27.132s.

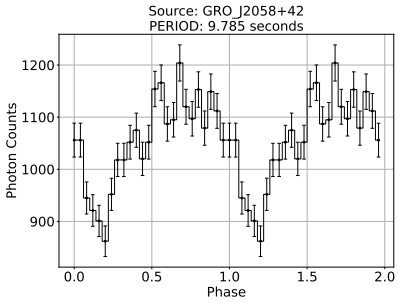

(b) For Fig. 3.85b at period 9.785s.

Figure 3.85: Phase folded lightcurve at the periods corresponding to the highest peak for the periodograms plotted in Fig 3.84.

Similarly, different periods arise in different extensions, some of which are repeated in more than one extension. These periods are found around ~9.7s, 20.5s, 27.1s and 39.7s. These periods can be produced due to other sources present in the field of view while observing GRO J2058+42, but the exact reason is not known. Strong supporting evidence is necessary to validate this.

3.4.3 Her X-1

The LMXB has a neutron star with a spin period of ∼1.24 seconds and an orbital period of 1.7 days (Shakura, N. I. et al. 2021). A different kind of peculiar behavior is seen in the lightcurves for this source. Fig. 3.86 is an example of such behavior. The lightcurves show a sudden jump in the photon counts.

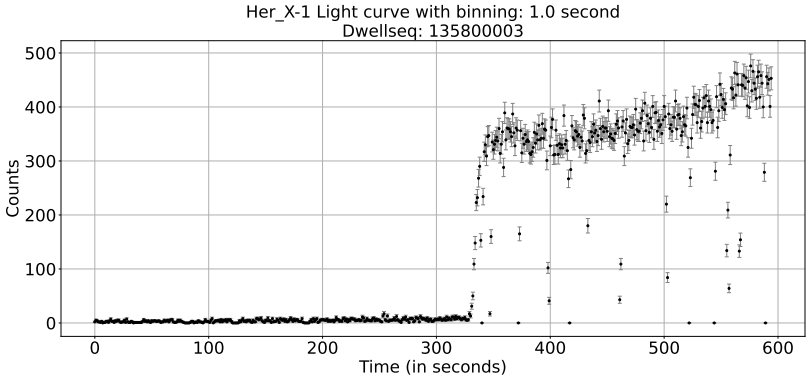

Figure 3.86: Her X-1: 1-sec binned lightcurve for dwell sequence 136460003.

Also, there is a high count rate observed in the lightcurves for some extensions. Fig. 3.87 shows this kind of behavior. This can be due to the appearance of any other source or group of sources with high flux while observing Her X-1. Studying these lightcurves will not give us the information about Her X-1, rather, it will show the combined behavior of the sources in the field of view of SSM.

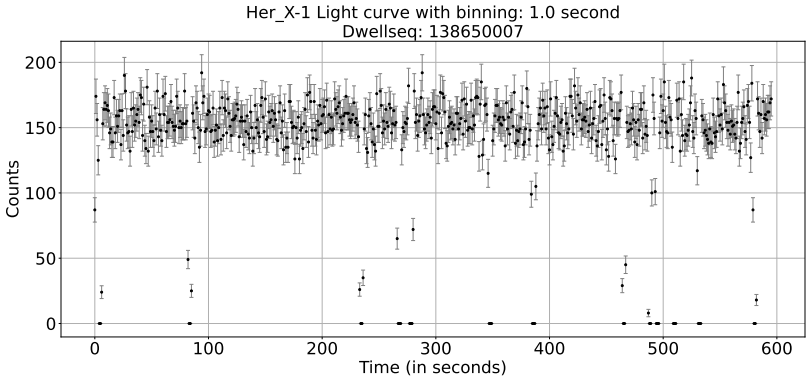

Figure 3.87: Her X-1: 1-sec binned lightcurve for dwell sequence 138650007.

To deal with this, lightcurves as in Fig. 3.88 are used for the study of this source.

Same as the above two sources, different lightcurves give different periods. Fig. 3.89 shows the periodogram and Fig. 3.90 shows the corresponding phase-folded lightcurves at the period of maximum power.

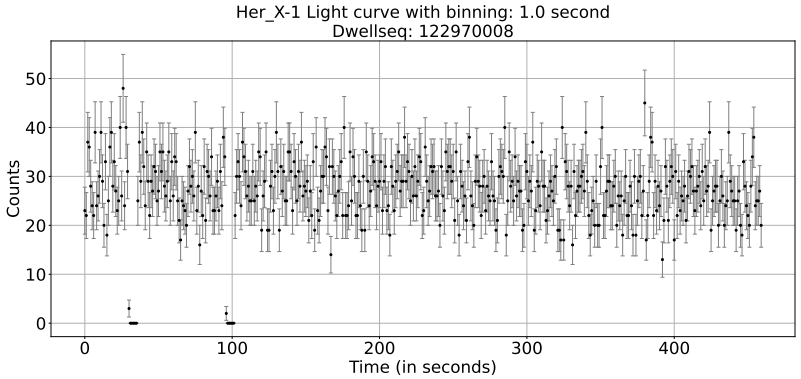

Figure 3.88: Her X-1: 1-sec binned lightcurve for dwell sequence 12297008.

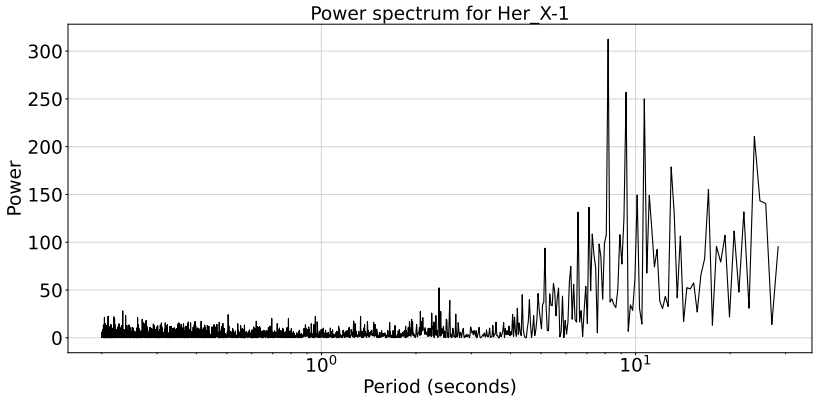

(a) Periodogram 1: maximum power at 8.177 sec.

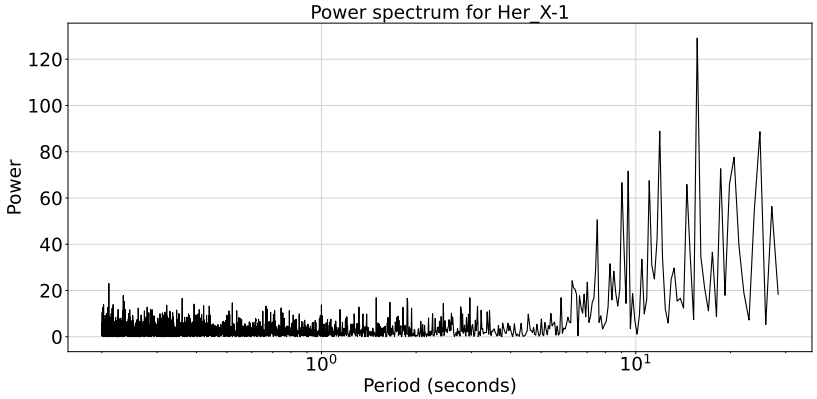

(b) Periodogram 2: maximum power at 15.682 sec.

Figure 3.89: Periodograms for two different light curves of Her X-1

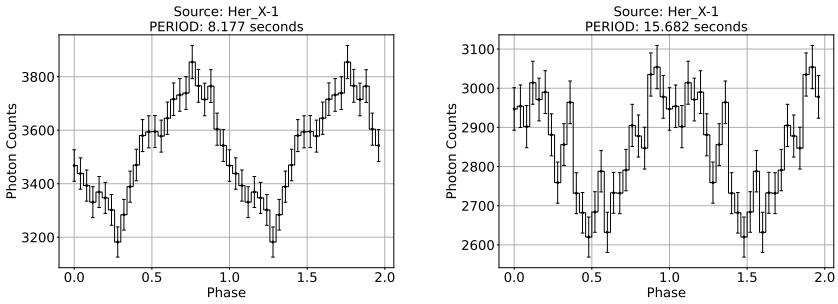

(a) For Fig. 3.89a at period 8.177s. (b) For Fig. 3.89b at period 15.682s.

Figure 3.90: Phase folded lightcurve at the periods corresponding to the highest peak for the periodograms plotted in Fig 3.89.

Also, the averaged periodogram does not show any significant period, implying high noise in the data.

3.5 Eclipse Modelling

To investigate long-term variability in X-ray binaries (XRBs), eclipses can serve as valuable probes. In binary systems, eclipses can last from a few minutes to several hours, depending on factors such as the size of the companion star, the dimensions of the compact object, orbital velocity, and the system's inclination angle.

We tried to make a model that can identify the eclipses, ingress time, egress time and can predict the next eclipse from the lightcurve. We applied it to find the eclipse in the source EXO 0748-676 from the LAXPC/AstroSat data. Fig. 3.91 shows the light curve of the source for 2.5 days with 5-second binning. Three bursts can be seen from the lightcurve, but the eclipses are not perfectly visible. Using the model, we have detected 6 eclipses in this lightcurve and 1 partial eclipse where the ingress and part of the eclipse is not observed, as shown in the Fig. 3.95.

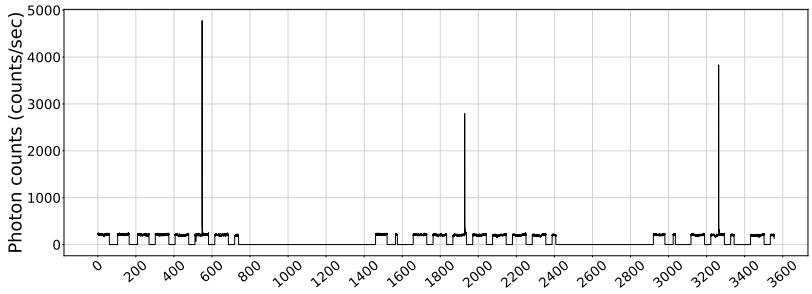

Figure 3.91: Lightcurve of the XRB source EXO 0748-676 with 5-second binning.

The methodology adopted for detecting eclipses in the lightcurve is outlined below:

It can be seen from Fig. 3.91 that the observation has many gaps where the photon count drops to zero. These gaps are the intervals of no observations for the source from LAXPC/AstroSat. Hence, the data is in chunks (here, 25 chunks where 6 chunks have very little observation time) rather than having a continuous observation. To deal with this, we tried to find the eclipse in different chunks separately. The modeling includes calculating means and variances of the photon counts for the eclipse detection of each

chunk. The photon counts from the flares, even for a few seconds, change the mean and variance of the chunk to a high level, hence the flares have to be removed before proceeding. So, the parts of flares and zero photon counts are eliminated for the modelling. In order to find the eclipses in a chunk, we start by finding the dips. Here, a dip will start from the first point where the photon count is smaller than 0.5 times the standard deviation of the chunk photons (σ_{chunk}) and will run until the photon count goes higher than σ_{chunk}. For this particular source, if the total time length of the dip is greater than 150 seconds, then only it will be a candidate dip for eclipse and then only we will calculate the ingress and egress time around this dip. The ingress starts from the point in the chunk around the dip where the photon count is 4 times the standard deviation of the dip flux (σ_{dip}) and ends at the first point where the photon count is above $0.5\sigma_{dip}$. The same convention is followed for the egress time, i.e., the egress starts where photon count > $0.5\sigma_{dip}$ and ends where photon count > $4\sigma_{dip}$.

Fig. 3.92 shows the interval of eclipse in the lightcurve, including ingress and egress.

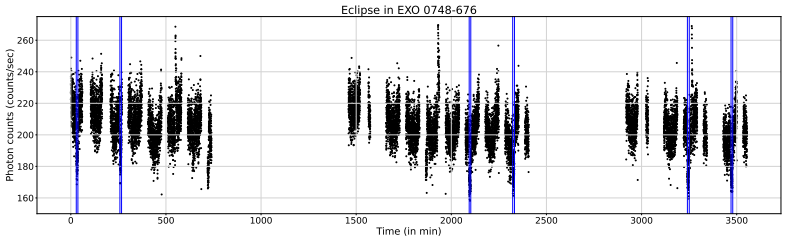

Figure 3.92: Lightcurve of EXO 0748-676. The intervals in blue are the eclipse found in the source.

The following figure shows the zoomed-in version of the eclipse and its ingress and egress times.

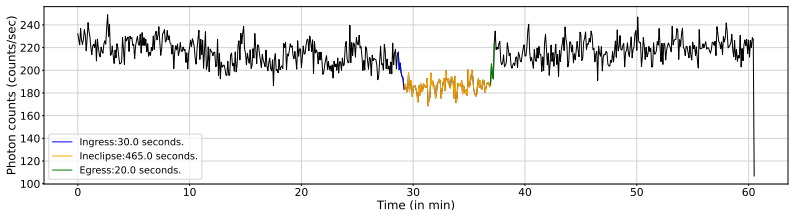

Figure 3.93: Eclipse in 1st chunk with ingress time: 30 seconds, eclipse time: 465 seconds and egress time: 20 seconds.

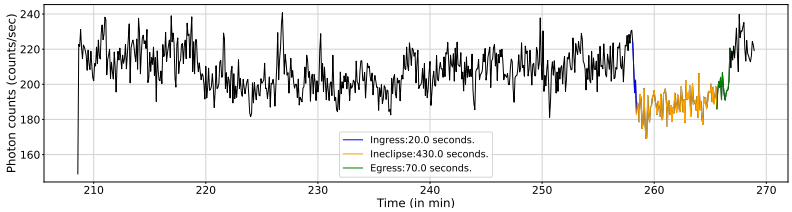

Figure 3.94: Eclipse in 3rd chunk with ingress time: 20 seconds, eclipse time: 430 seconds and egress time: 70 seconds.

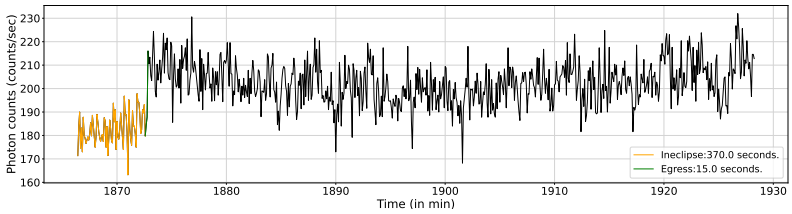

Figure 3.95: Partial eclipse in 15th chunk with egress time: 15 seconds and eclipse time more than 370 seconds.

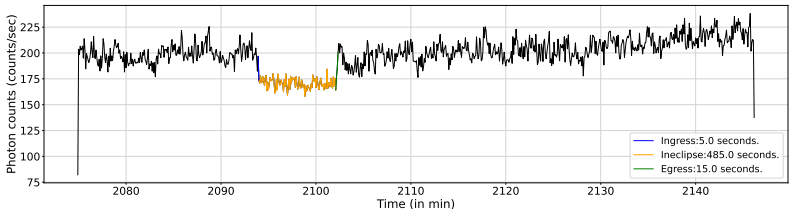

Figure 3.96: Eclipse in 18th chunk with ingress time: 5 seconds, eclipse time: 485 seconds and egress time: 15 seconds.

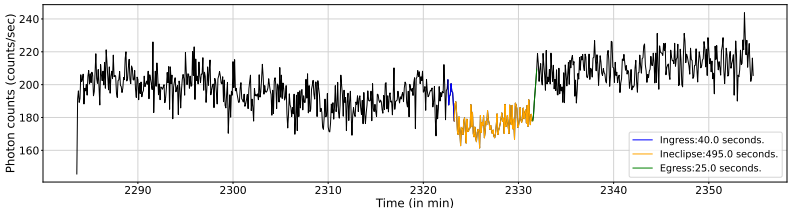

Figure 3.97: Eclipse in 20th chunk with ingress time: 40 seconds, eclipse time: 495 seconds and egress time: 25 seconds.

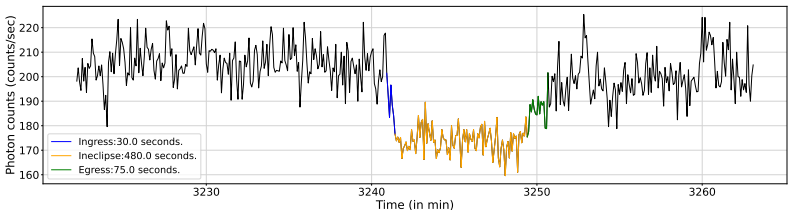

Figure 3.98: Eclipse in 25th chunk with ingress time: 30 seconds, eclipse time: 480 seconds and egress time: 75 seconds.

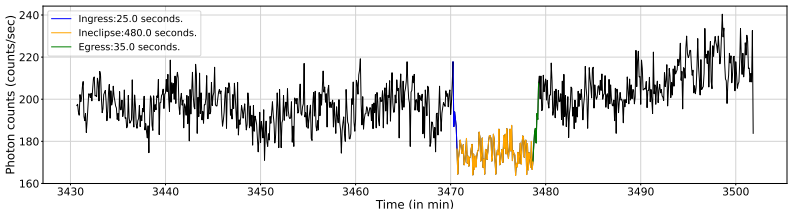

Figure 3.99: Eclipse in 28th chunk with ingress time: 25 seconds, eclipse time: 480 seconds and egress time: 35 seconds.

Table 3.2 summaries the eclipse times found in different chunks. The

Eclipse no.	**Ingress time (in sec)**	**In-eclipse time (in sec)**	**Egress time (in sec)**
1	30	465	20
2	20	430	70
3	-	370 (partial detection)	15
4	5	485	15
5	40	495	25
6	30	480	75
7	25	480	35

Table 3.2: Estimated time of the eclipse in different chunks.

binning of the lightcurve is 5 seconds, hence there is always a least count error of 5 seconds present. Since the least count is 5 seconds, the uncertainty in each measurement is typically taken as:

For six times measurements (excluding partial eclipse), the error can be propagated as:

$$\sigma_{total} = 5/\sqrt{6} = 2.04\ seconds$$

On averaging the ingress, eclipse and egress times, we get:

$$T_{ingress} = 25 \pm 2.04\ seconds$$

$$T_{eclipse} = 472.5 \pm 2.04\ seconds$$

$$T_{egress} = 27.5 \pm 2.04\ seconds$$

For the above calculation, the partial eclipse is not taken into account.

The ingress and egress times are different for different chunks. Also, the egress time is more extended than the ingress time when averaged. The results are somewhat close (but not very good) to the results found by Knight et al. 2021 where the eclipse time is ~500 seconds, the ingress time is 15.2 seconds and the egress time is 17.5 seconds. To model eclipse for other sources, the parameters like $\sigma_{chunk}\ and\ \sigma_{dip}$ will change. Hence, the criteria for the start and end of the dip/eclipse, ingress and egress will be changed depending on the source. Hence, the model is not a very strong enough to detect an eclipse in every lightcurve. Changes in the model are needed to a large extent for better parameter estimation. This can also be seen from the difference between the time parameters found by us and those found by Knight et al. 2021.

The modelling can further be extended to study the difference in the ingress and egress times, and also to study the extended egress times. On the other hand, spectral analysis can also provide a good insight into the behavior of the source at the time of eclipse. But since we are looking for the temporal evolution of the sources, this is beyond the scope of this project.

Chapter 4

Discussion

We analysed 22 sources out of 25 reported in KC11. We found some new previously unreported periodicities for a subset of sources, whereas for the others, we detected no significant periodicities. The reason for not seeing the previously known super-orbital periodicities is the evolution of the XRBs with time. As the systems evolve, the mechanisms giving rise to the super-periodicities change, resulting in the change of these periods. Since the orbital period of the source does not evolve, we found these periods in our analysis, at least for some HMXBs. The orbital periods of the LMXBs (except Cyg X-2, which has P_{orb} = 9.844days (Liu, Paradijs, and E. P. J. v. d. Heuvel 2007) and two HMXBs, LMC X-3 and LMC X-4, are less than 2 days, which cannot be detected in our study due to the light curve binning constraints. A light curve binned in seconds or hours can help us detect these periods.

A subset of X-ray binaries exhibits stable superorbital periods, such as ~35 days in Her X-1, ~162 days in SS433, and ~30 days in LMC X-4. The persistence of these periodicities suggests that the underlying mechanisms, such as stable precession of a warped accretion disk, remain relatively unchanged over the observational timescales. Conversely, other systems display significant variability in their superorbital periods, implying dynamic changes in their accretion disk structure.

We also found some new periodicities in some of the sources, like:
Cen X-1, Her X-1 , LMC X-4, SMC X-1, X1636-536 and X1907+097.

Some of these periodicities are due to the intrinsic physical properties of the sources, and some may be artifacts. There is a detection of a period around ~2 days in some sources, e.g., Cen X-1, Her X-1 and SMC X-1, so it can be an artifact whose reason is yet to be figured out. Other than this, ~72 days period in LMC X-2, X1636-536 and X1907+097, and ~36 days of period in LMC X-2 and X1907+097, are also artifacts arising due to the precession period of ISS. The period of 72 is also observed in DPS of many sources, like GX 339-4, Sco X-1, X0114+650 and X1916-053. These three periods are potential candidates for instrumental artifacts, as it is uncommon to detect identical periods across multiple independent sources.

Other than the periods of some hundreds of days, we detected a period of ~1840 days in X1636-536 which looks unreal. XRBs can have a superorbital period >1000 days, but it is very rare. Some of the sources like SXP 138, GX-304 and γ-Cas show superorbital periods > 1000 days as discussed Chashkina et al. 2015. The detected period is likely to be a false detection for two reasons: first, there are only about 3 cycles of this period in ~15 years of data; second, because of the edge effects due to rescaling of the periodogram, the noise itself mimics the signal. Robust evidence is required to confirm this period as an intrinsic property of the source.

Along with the rescaled periodogram, the dynamic power spectrum provides deeper insights into the temporal evolution of periodicities in the sources. Through the DPS analysis, we identified periodicities that were not apparent in the periodogram generated from the entire ~15 years of data. For instance, in the case of sources GRS 1747-312, SMC X-1, X1730-333 and X1907+097, new periodicities at ~24, 65, 100 and 24 days were detected, respectively, in the DPS but were absent in the full-period periodogram. This discrepancy may be attributed to the suppression of weaker periodic signals by the dominant power of stronger periods in the overall dataset. Therefore, the DPS was employed to capture the local, time-dependent evolution of the systems more effectively.

To further investigate the X-ray binaries and the detected periodicities, we examined the fractional amplitude, which revealed varying trends across the observed periods. We observed a variety of trends in the fractional

amplitude values with increasing energy, including monotonic increases (e. g., LMC X-4 at 51.64 days) and decreases (e. g., SMC X-1 at 4.19 and 3.89 days), instances of no significant variation (e. g., Her X-1 at 2.51 and 14.02 days), and turnover behaviors (e. g., X1097+097 at 71.75 days). The period which do not show any significant changes with energy can be the instrument artifacts, as these affect the photon count rate equally in energy bands.

Additionally, we attempted to identify superorbital periods using the SSM data but did not detect any. This is likely due to the presence of significant data gaps, which obstruct the detection of long-term periodicities. As a result, the SSM data is not well-suited for studying superorbital variations. Moreover, the data is not sufficiently filtered to reliably identify pulsations either. From pulse analysis of sources Cen X-3, GRO J2058+42 and Her X-1, we found different periods for the same source. These periods may not be associated with the sources as they are detected in one extension but not in the very next extension. The source generally does not show high variations in very small amount of time. The reason for this can be the noise or the appearance of other sources in the field of view at the time of scanning any of the above sources. As SSM has a large field of view of $22.1^o \times 100^o$, it can scan many sources simultaneously. Other than from the X-ray sources, the X-ray from the Sun and reflected from Earth also contribute to the flux in the lightcurves. The contribution from all the factors affects the lightcurves and in-turn the periodogram. These may be the reasons for the many periods seen other than the original spin periods of the source in the periodograms. These all contributions from the different sources may suppress the signals from the source under study, making it too hard to detect the desired signal.

The search for a meaningful signal from SSM was made to test the data of this instrument. The sources with known spin periods were used for the same. If we had detected the spin periods in the three sources, we could have used the other sources to find pulsations from the instrument. Hence, the pipelines used to clean the SSM data need better filtering algorithms and the data needs to be continuous to have a better analysis. If the data is well filtered, it can be used for all the three aspects, superorbital periods, pulsation and the eclipse, of the project.

Other than finding periodicities across different time scales, an effort is made to detect the eclipse from the lightcurve of the sources is also made. We found 6 eclipses and 1 partial eclipse for EXO 0748-676 from LAXPC data. There are large uncertainties in calculating the ingress, egress and in-eclipse time. The algorithm needs modifications for a better study of the eclipses.

Chapter 5

Future plans

After successfully developing the periodogram and identifying significant power levels and periods, the next step is to investigate the causes of these periodicities. We need to determine whether they are artifacts or a result of underlying mechanisms in the binary systems. Fractional amplitude is calculated in different energy bands to investigate the emitting region. This is not sufficient to find the cause of the period. Hence, we have to come up with some analysis to find the cause. One can do spectral analysis for the same.

While calculating the fractional amplitude, the reduced chi square has high values when the model is fitted. A proper and deep analysis will be helpful to fit a better model and a better understanding of the sources. If this problem is resolved, better parameter estimation can be achieved, leading to a closer physical relation to the system.

The objective of studying pulsations and their long-term variability using SSM data could not be achieved due to the poor quality of the data, which contains numerous peculiarities and anomalies. Therefore, there is a strong need to thoroughly clean and preprocess SSM data for each source. If the data quality remains insufficient even after cleaning, it may be necessary to consider using alternative instruments for the analysis.

The eclipse modelling that we have done needs a lot of optimization and modification. It worked very well in the case of EXO 0748-676 as

the lightcurve does not have much variations. If any source shows high variability, the model needs different threshold criteria for mean and standard deviation to find the eclipse. Also, the algorithm cannot distinguish between the dip and the eclipse. An optimized modelling is also needed to find the ingress and egress times of the eclipse. A machine learning model can be used to get better results for this. The model can be extended to the prediction of the next eclipses. The analysis can aid in investigating the shrinking and expansion of the binary orbit. Also, spectral analysis can be carried out to gain deeper insights into the physical properties of the X-ray source and its companion. This includes investigating the emission mechanisms, estimating the temperature and composition of the accretion material, and identifying any spectral features that may help constrain the nature of the compact object and its interaction with the companion star.

Bibliography

[1] URL: https://iss.jaxa.jp/en/kiboexp/ef/maxi/.

[2] M. Ackermann et al. "Multiwavelength Evidence for Quasi-periodic Modulation in the Gamma-Ray Blazar PG 1553+113". In: *Astrophysical Journal Letters* 813.2, L41 (Nov. 2015), p. L41. DOI: 10.1088/2041-8205/813/2/L41. arXiv: 1509.02063 [astro-ph.HE].

[3] *AstroSat, INDIA'S FIRST MULTIWAVELENGTH ASTRONOMY SATELLITE*. 2014. URL: https://web.iucaa.in/~astrosat/AstroSat_handbook.pdf.

[4] D J K Buisson et al. "Dips and eclipses in the X-ray binary Swift J1858.6–0814 observed with NICER". In: *Monthly Notices of the Royal Astronomical Society* 503.4 (Mar. 2021), pp. 5600–5610. ISSN: 1365-2966. DOI: 10.1093/mnras/stab863. URL: http://dx.doi.org/10.1093/mnras/stab863.

[5] Phil Charles et al. "Observational properties of accretion discs: Precessing and warped?" In: *New Astronomy Reviews* 51.10 (2008). Jean-Pierre Lasota, X-ray Binaries, Accretion Disks and Compact Stars, pp. 768–774. ISSN: 1387-6473. DOI: https://doi.org/10.1016/j.newar.2008.03.025. URL: https://www.sciencedirect.com/science/article/pii/S1387647308000274.

[6] Anna Chashkina et al. "Superorbital variability of the X-ray flux in the Be-donor binaries SXP 138, GX-304, and γCas". In: *Astronomy Reports* 59 (June 2015), pp. 563–572. DOI: 10.1134/S1063772915060074.

[7] W.I. Clarkson et al. “Long-term properties of accretion discs in X-ray binaries — I. The variable third period in SMC X-1”. In: *Monthly Notices of the Royal Astronomical Society* 339.2 (Feb. 2003), pp. 447–454. ISSN: 0035-8711. DOI: 10.1046/j.1365-8711.2003.06176.x. eprint: https://academic.oup.com/mnras/article-pdf/339/2/447/3242942/339-2-447.pdf. URL: https://doi.org/10.1046/j.1365-8711.2003.06176.x.

[8] Robin H. D. Corbet et al. *Sharp Periodic Flares and Long-Term Variability in the High-Mass X-ray Binary XTE J1829-098 from RXTE PCA, Swift BAT and MAXI Observations*. 2024. arXiv: 2410.03500 [astro-ph.HE]. URL: https://arxiv.org/abs/2410.03500.

[9] A. P. Cowley et al. “Discovery of a Long-Term Periodic Variation in LMC X-3”. In: *The Astrophysical Journal* 381 (Nov. 1991), p. 526. DOI: 10.1086/170676.

[10] D. Crampton, A. P. Cowley, and J. B. Hutchings. “The probable binary nature of SS 433.” In: *Astrophysical Journal Letters* 235 (Feb. 1980), pp. L131–L135. DOI: 10.1086/183176.

[11] Falanga, M. et al. “INTEGRAL and RXTE observations of accreting millisecond pulsar IGR J00291+5934 in outburst”. In: *Astronomy & Astrophysics* 444.1 (2005), pp. 15–24. DOI: 10.1051/0004-6361:20053472. URL: https://doi.org/10.1051/0004-6361:20053472.

[12] R. Giacconi et al. “Discovery of Periodic X-Ray Pulsations in Centaurus X-3 from UHURU”. In: *Astrophysical Journal Letters* 167 (July 1971), p. L67. DOI: 10.1086/180762.

[13] D. E. Gruber and R. E. Rothschild. “SMC X-1 variability observed from HEAO 1.” In: *The Astrophysical Journal* 283 (Aug. 1984), pp. 546–551. DOI: 10.1086/162338.

[14] G. L. Israel and L. Stella. “A New Technique for the Detection of Periodic Signals in “Colored” Power Spectra”. In: *The Astrophysical Journal* 468 (Sept. 1996), p. 369. DOI: 10.1086/177697. arXiv: astro-ph/9603038 [astro-ph].

[15] Wang Jun-yi et al. “Periodicity Analysis of X-ray Light Curves of SS 433”. In: *Chinese Astronomy and Astrophysics* 41.1 (2017), pp. 42–61. ISSN: 0275-1062. DOI: https://doi.org/10.1016/j.chinastron.2017.01.005. URL: https://www.sciencedirect.com/science/article/pii/S0275106217300127.

[16] Amy H Knight et al. “Eclipse mapping of EXO 0748–676: evidence for a massive neutron star”. In: *Monthly Notices of the Royal Astronomical Society* 510.4 (Dec. 2021), pp. 4736–4756. ISSN: 1365-2966. DOI: 10.1093/mnras/stab3722. URL: http://dx.doi.org/10.1093/mnras/stab3722.

[17] M. M. Kotze and P. A. Charles. “Characterizing X-ray binary long-term variability: Long-term variability in X-ray binaries”. In: *Monthly Notices of the Royal Astronomical Society* 420.2 (Dec. 2011), pp. 1575–1589. ISSN: 0035-8711. DOI: 10.1111/j.1365-2966.2011.20146.x. URL: http://dx.doi.org/10.1111/j.1365-2966.2011.20146.x.

[18] M. I. Kudryavtsev et al. “An Indication of 62-HOUR Periodicity in SCORPIUS-X-1 Based on the PROGNOZ-9 X-Ray Experiment”. In: *Soviet Astronomy Letters* 15 (Nov. 1989), p. 466.

[19] Paweł Lachowicz et al. “Periodic long-term X-ray and radio variability of Cygnus X-1”. In: *Monthly Notices of the Royal Astronomical Society* 368.3 (Apr. 2006), pp. 1025–1039. ISSN: 0035-8711. DOI: 10.1111/j.1365-2966.2006.10219.x. eprint: https://academic.oup.com/mnras/article-pdf/368/3/1025/18663985/mnras0368-1025.pdf. URL: https://doi.org/10.1111/j.1365-2966.2006.10219.x.

[20] Q. Z. Liu, J. van Paradijs, and E. P. J. van den Heuvel. “A catalogue of low-mass X-ray binaries in the Galaxy, LMC, and SMC(Fourth edition)”. In: *Astronomy & Astrophysics* 469.2 (Apr. 2007), pp. 807–810. ISSN: 1432-0746. DOI: 10.1051/0004-6361:20077303. URL: http://dx.doi.org/10.1051/0004-6361:20077303.

[21] N. R. Lomb. “Least-Squares Frequency Analysis of Unequally Spaced Data”. In: *Astrophysics and Space Science* 39.2 (Feb. 1976), pp. 447–462. DOI: 10.1007/BF00648343.

[22] Bruce Margon. “Observations of SS 433”. In: *Annual Review of Astronomy and Astrophysics* 22 (Jan. 1984), pp. 507–536. DOI: 10.1146/annurev.aa.22.090184.002451.

[23] Masaru Matsuoka et al. “The MAXI Mission on the ISS: Science and Instruments for Monitoring All-Sky X-Ray Images”. In: *Publications of the Astronomical Society of Japan* 61.5 (Oct. 2009), pp. 999–1010. ISSN: 0004-6264. DOI: 10.1093/pasj/61.5.999. URL: http://dx.doi.org/10.1093/pasj/61.5.999.

[24] Kallol Mukerjee, H. M. Antia, and Tilak Katoch. “AstroSat Observations of GRO J2058+42 during the 2019 Outburst”. In: *The Astrophysical Journal* 897.1 (July 2020), p. 73. ISSN: 1538-4357. DOI: 10.3847/1538-4357/ab97b6. URL: http://dx.doi.org/10.3847/1538-4357/ab97b6.

[25] G. I. Ogilvie and G. Dubus. “Precessing warped accretion discs in X-ray binaries”. In: *Monthly Notices of the Royal Astronomical Society* 320.4 (Feb. 2001), pp. 485–503. ISSN: 1365-2966. DOI: 10.1046/j.1365-8711.2001.04011.x. URL: http://dx.doi.org/10.1046/j.1365-8711.2001.04011.x.

[26] A. Papitto, E. Bozzo, et al. “The discovery of the 401 Hz accreting millisecond pulsar IGR J17498-2921 in a 3.8 h orbit”. In: *Astronomy & Astrophysics* 535, L4 (Nov. 2011), p. L4. DOI: 10.1051/0004-6361/201117995. arXiv: 1111.1976 [astro-ph.HE].

[27] A. Papitto, T. Di Salvo, et al. “Timing of the accreting millisecond pulsar XTE J1814338”. In: *Monthly Notices of the Royal Astronomical Society* 375.3 (Jan. 2007), pp. 971–976. ISSN: 0035-8711. DOI: 10.1111/j.1365-2966.2006.11359.x. eprint: https://academic.oup.com/mnras/article-pdf/375/3/971/3936529/mnras0375-0971.pdf. URL: https://doi.org/10.1111/j.1365-2966.2006.11359.x.

[28] B. Paul, S. Kitamoto, and F. Makino. “Changes in the Long-Term Intensity Variations in Cygnus X-2 and LMC X-3”. In: *The Astrophysical Journal* 528.1 (Jan. 2000), p. 410. DOI: 10.1086/308149. URL: https://dx.doi.org/10.1086/308149.

[29] W. C. Priedhorsky and J. Terrell. “Long-term observations of X-ray sources : the Aquila-Serpens-Scutum.” In: *The Astrophysical Journal* 280 (May 1984), pp. 661–670. DOI: 10.1086/162039.

[30] W. C. Priedhorsky and J. Terrell. “Long-term X-ray observations of CEN X-3, GX 301-2 (4U 1223-62), GX 304-1 (4U 1258-61) and 4U 1145-61.” In: *The Astrophysical Journal* 273 (Oct. 1983), pp. 709–715. DOI: 10.1086/161406.

[31] Andreas Reisenegger. *Magnetic Fields of Neutron Stars: an Overview*. 2001. arXiv: astro-ph/0103010 [astro-ph]. URL: https://arxiv.org/abs/astro-ph/0103010.

[32] Javier Rico. “The Variable Superorbital Modulation of Cygnus X-1”. In: *The Astrophysical Journal* 683.1 (July 2008), pp. L55–L58. ISSN: 1538-4357. DOI: 10.1086/591472. URL: http://dx.doi.org/10.1086/591472.

[33] Tiziana Di Salvo and Andrea nana. *Accretion powered X-ray millisecond pulsars*. 2020. arXiv: 2010.09005 [astro-ph.HE]. URL: https://arxiv.org/abs/2010.09005.

[34] A Sanna et al. “Timing of the accreting millisecond pulsar IGR J17591-2342: evidence of spin-down during accretion”. In: *Monthly Notices of the Royal Astronomical Society* 495.2 (May 2020), pp. 1641–1649. ISSN: 1365-2966. DOI: 10.1093/mnras/staa1253. URL: http://dx.doi.org/10.1093/mnras/staa1253.

[35] A. Sanna et al. “Study of the accretion torque during the 2014 outburst of the X-ray pulsar GRO J174428”. In: *Monthly Notices of the Royal Astronomical Society* 469.1 (Mar. 2017), pp. 2–12. ISSN: 1365-2966. DOI: 10.1093/mnras/stx635. URL: http://dx.doi.org/10.1093/mnras/stx635.

[36] Sanna, A. et al. “Astronomy & Astrophysics”. In: *Astronomy & Astrophysics* 616 (2018), p. L17. DOI: 10.1051/0004-6361/201833205. URL: https://doi.org/10.1051/0004-6361/201833205.

[37] J. D. Scargle. “Studies in astronomical time series analysis. II. Statistical aspects of spectral analysis of unevenly spaced data.” In: *The Astrophysical Journal* 263 (Dec. 1982), pp. 835–853. DOI: 10.1086/160554.

[38] E. Schreier et al. “Discovery of the Binary Nature of SMC X-1 from UHURU”. In: *Astrophysical Journal Letters* 178 (Dec. 1972), p. L71. DOI: 10.1086/181086.

[39] S. Seetha et al. “The Scanning Sky Monitor (SSM) on ASTROSAT”. In: *Advances in Space Research* 38.12 (2006). Spectra and Timing of Compact X-ray Binaries, pp. 2995–2998. ISSN: 0273-1177. DOI: https://doi.org/10.1016/j.asr.2005.09.046. URL: https://www.sciencedirect.com/science/article/pii/S0273117706000238.

[40] Shakura, N. I. et al. “Observations of Her X-1 in low states during SRG/eROSITA all-sky survey”. In: *Astronomy & Astrophysics* 648 (2021), A39. DOI: 10.1051/0004-6361/202040145. URL: https://doi.org/10.1051/0004-6361/202040145.

[41] Alan P. Smale and James C. Lochner. “Long-Term Variability in Low-Mass X-Ray Binaries: A Study Using Data from VELA 5B”. In: *The Astrophysical Journal* 395 (Aug. 1992), p. 582. DOI: 10.1086/171678.

[42] Thomas M. Tauris and Ed van den Heuvel. *Formation and Evolution of Compact Stellar X-ray Sources*. 2003. arXiv: astro-ph/0303456 [astro-ph]. URL: https://arxiv.org/abs/astro-ph/0303456.

[43] Jacob T. VanderPlas. “Understanding the Lomb–Scargle Periodogram”. In: *The Astrophysical Journal Supplement Series* 236.1 (May 2018), p. 16. DOI: 10.3847/1538-4365/aab766. URL: https://dx.doi.org/10.3847/1538-4365/aab766.

[44] Roland Walter and Carlo Ferrigno. “X-Ray Pulsars”. In: *Handbook of Supernovae*. Springer International Publishing, 2017, pp. 1385–1399. ISBN: 9783319218465. DOI: 10.1007/978-3-319-21846-5_74. URL: http://dx.doi.org/10.1007/978-3-319-21846-5_74.

[45] Linqing Wen et al. “A Systematic Search for Periodicities in RXTE ASM Data”. In: *The Astrophysical Journal Supplement Series* 163.2 (Apr. 2006), p. 372. DOI: 10.1086/500648. URL: https://dx.doi.org/10.1086/500648.

[46] Patrick Wojdowski et al. “Quasi-periodic Occultation by a Precessing Accretion Disk and Other Variabilities of SMC X-1”. In: *The Astrophysical Journal* 502.1 (July 1998), p. 253. DOI: 10.1086/305893. URL: https://dx.doi.org/10.1086/305893.

[47] J. S. Yadav et al. “Large Area X-ray Proportional Counter (LAXPC) instrument onboard ASTROSAT”. In: *Space Telescopes and Instrumentation 2016: Ultraviolet to Gamma Ray*. Ed. by Jan-Willem A. den Herder, Tadayuki Takahashi, and Marshall Bautz. Vol. 9905. Society of Photo-Optical Instrumentation Engineers (SPIE) Conference Series. July 2016, 99051D, p. 99051D. DOI: 10.1117/12.2231857.